EASI SMR

D7.3 Analysis of the code benchmarking for the PRATIC core at BOC conditions

Géraud PRULHIÈRE, Grégoire LEHOUX (CEA)
Jin LI (PSI)
Gianfranco HUACCHO-ZAVALA, Luigi MERCATALI (KIT)
Iurii OVDIIENKO (SSTC-NRS)
Marco TIBERGA (EDF)
Romain VUIART, Franck BERNARD (ASNR)
Ondrej PETRASEK, František NEUMAN (UJV)
Marc-Antoine DOR, Ruben PERSICOT (FRAMATOME)
David DE MEYER (TRACTEBEL)

1. Document information

Grant Agreement Number	n°101164810
Project Title	Ensuring Assessment of Safety Innovations for SMR
Project Acronym	EASI-SMR
Project Coordinator	Nicolas Sobecki, EDF
Project Duration	1 September 2024 – 31 August 2028 (48 months)
Related Work Package	WP 7
Lead Organisation	CEA
Contributing Partner(s)	ASNR, CEA, EDF, Framatome, HZDR, KIT, PSI, SSTC NRS, Tractebel, UJV
Submission Date	24.04.2026
Dissemination Level	Public

2. History

Date	Submitted by	Reviewed by	Version (Notes)
07/04/2026	G. Prulhière (CEA)	V.-H. Sanchez-Espinoza (KIT)	V1
07/04/2026		V.-H. Sanchez-Espinoza (KIT)	V2 (1st review of the document)
15/04/2026		V.-H. Sanchez-Espinoza (KIT)	V3 (minor modifications, grammatical mainly)
22/04/2026	G. Prulhière (CEA)	V.-H. Sanchez-Espinoza (KIT)	V4 (Modify list of co-autors on the 1st page + complementary conclusions on sections 9.1.3 and 10)
24/04/2026	N. Sobecki (EDF)	O. Fauchet, A. Paul	Final

Co-funded by the European Union
UK Research and Innovation
The Research Council of Norway
Project funded by

Table of Contents

List of Figures

List of Tables

3. Summary

This document describes the work carried out as part of Work Package 7, which is dedicated to advanced fundamental physics studies on boron-free SMR designs. This deliverable reflects the Task 7.2.1, focused on the analysis of the PRATIC SMR, a virtual reactor designed for benchmark studies, applying different computational routes. Specifically, it is a PWR-type reactor that operates without soluble boron. The objective of this task is to calibrate neutron physics calculations, and to compare standard calculation methods used in industry with reference calculations based on Monte Carlo method and advanced deterministic transport calculation methods.

A total of 9 organisations took part in this benchmark, using 12 different calculation chains.
The calculations performed by KIT using the SERPENT2 code were used as the reference. Other calculations based on the Monte Carlo method were also carried out. CEA and EDF performed calculations using TRIPOLI4, while ASNR performed calculations using TRIPOLI5, and PSI also used SERPENT2.
Advanced methods were carried out using neutron transport methods: CEA with APOLLO3-Sn, FRAMATOME with APOLLO3-SPn and PSI with nTracer MoC.
Industry-grade methods were performed using the neutron diffusion theory: ASNR, KIT and PSI with CMS5 code system, involving the codes CASMO5 and SIMULATE5; ANSR also performed CASMO5/PARCS calculations; CEA with APOLLO3-Diffusion and APOLLO2/CRONOS2 codes; SSTC NRS and UJV used HELIOS and DYN3D codes for their simulations; TRACTEBEL used the WIMS/PANTHER calculation chain.
Most of these simulations were based on both ENDF/B7.1 or JEFF-3.1.1 nuclear data libraries. Due to code constraints, SSTC NRS used ENDF/B6 for HELIOS/DYN3D and PSI used ENDF/B7.0 for nTracer.

The work for Task 7.2.1 was divided into two phases:

- The first phase aimed to model the core in a hot zero-power (HZP) state. In this state, the core is isothermal, with only neutron effects governing its behaviour. This is therefore an important step calibrating the neutron physics alone.
- The second phase aimed to model the core in a hot, full-power (HFP) state. In this state, the core's behaviour is governed by both neutronics and thermohydraulics. Therefore, it is necessary to use computational codes that couple these two disciplines.

In the first phase, the following type of values were calculated in HZP state by the codes and compared together: infinite or effective neutron multiplication factors, 1D-axial or 2D-radial power distributions and neutron kinetic parameters. The results obtained using Monte Carlo methods showed a very high level of agreement. Industrial-standard neutron simulations, employing neutron diffusion theory, supplied two categories of results, as is usually the case in this type of benchmark exercise:

- Those that behave similarly to the reference, with limited reactivity calculation biases (less than a 250 pcm deviation for k_{∞} and k_{eff}, with deviations limited to 300 pcm for CRBW, power differences per assembly of less than 0.04 in 2D and 0.01 in 1D, and 3% for neutron kinetic parameters).
- Those showing greater deviations from the reference (up to 1500 pcm on the k_{∞}, 1,200 pcm in core reactivity calculations, 2,000 pcm in CRBW, power differences of up to 0.23 in 2D and 0.015 in 1D, and around 7% in kinetic parameters).

The results obtained with advanced methods based on the transport theory were globally disappointing: they were not really any better than the worst-performing category of industrial

results, despite the computational cost (in terms of CPU time and memory) being significantly higher.

In the second phase, which was performed in the HFP state, simulations were carried out by either setting the xenon to zero or by activating the estimation of the xenon equilibrium level. Compared to the HZP condition, deviations in reactivity values are more pronounced (around 100 to 300 pcm) when the thermal feedback are activated and the xenon deactivated. Activating the xenon equilibrium tends to reduce these core reactivity deviations, allowing reactivity deviations to be brought back under 125 pcm. Critical control rods insertion of several configurations was estimated with a deviation range of ±5 cm from the reference. The distribution of power, fuel and coolant temperature within the core was compared. The power distributions were found to be very similar, with most of the results ranging from ±0.05 around the reference. Most of the codes tend to underestimate the fuel temperature by almost -6 °C and the coolant temperature by almost -0.5 °C.

In conclusion, given the efforts made to ensure a very high level of reliability in the reference calculations and the satisfactory agreement between the results obtained by the various codes and the reference results, Task 7.2.1, which involved characterising the PRATIC core loaded with fresh fuel, is considered complete. The PRATIC core has been fully characterised under conditions ranging from zero power to full power.

4. Keywords

comparison; transport, diffusion, Monte Carlo; deterministic; advanced; neutron physics; HZP; HFP

5. Abbreviations and acronyms

Acronym	Description
ARI	All Rods In. Configuration where all the control rods are fully inserted into the core.
ARO	All Rods Out. Configuration where all the control rods are extracted from the core.
BOC	Beginning of Cycle: in this document, it is considered equivalent to BOL
BOL	Beginning of Life: a state where all the fuel composing the core is fresh.
CRB	Control Rod Bank
CRBW	Control Rod Bank Worth
CTC	Coolant Temperature Coefficient
EASI-SMR	Ensuring Assessment of Safety Innovations for Small Modular Reactors
FA	Fuel assembly
FTC	Fuel Temperature Coefficient
HFP	Hot Full Power: at this operating condition, the core produces 350 MWth; the moderator core inlet temperature is 285 °C; the difference in water temperature between the inlet and outlet of the core is 30°C; the pressure in the primary loop is 155 bars.
HZP	Hot Zero Power: operating condition where no power is produced by the core, and an isothermal state at 300 °C for all the materials and geometries; the pressure in the primary loop is 155 bars.
MoC	Method of Characteristics
NDL	Nuclear Data Library
SMR	Small Modular Reactor
SVT	Sampling Velocity in the Target nucleus
TSL	Thermal Scattering Law
WP	Work Package
XS	Cross section

6. Introduction

Small modular reactors (SMRs) have gained attraction as a low-carbon energy solution, offering advantages such as modularity, passive safety and versatility for applications such as heating and hydrogen production (IAEA, 2024). The EASI-SMR (Ensuring Assessment of Safety Innovations for Small Modular Reactors) project, which was launched in 2024 as part of the Horizon Europe Euratom Programme, is tackling the specific safety and licensing challenges of European light-water SMR designs (Tulkki, Sanchez-Espinoza, & Sobecki, 2025). Coordinated by EDF, the project involves 38 partners from 16 countries and focuses on developing a robust safety framework (EASI-SMR Project, 2025). The project is organised into nine work packages (WPs), including WP7 which is dedicated to advanced fundamental physics studies on boron-free SMR designs.

Boron-free PWR cores are based on less extensive experience and technical knowledge than traditional PWR cores, which use boron for reactivity control. This justified the WP7 dedicated to study the neutron-physical behaviour of boron free cores and their specific characteristics, modelling, and simulation challenges (European SMR pre-Partnership Workstream 5 –Research, Development, and Innovation Roadmap, 2023). This work package is led by KIT and involves two main benchmark exercises:

- The first focuses on the PRATIC core (Vuiart, Eustache, Eveillard, & Prulhière, 2024), an electricity-generating virtual concept developed by CEA and the subject of this document.
- The second exercise deals with the LDR-50-Lite design (LDR lite benchmark, 2025): a public version of the LDR-50 reactor, which was originally developed at VTT Technical Research Centre of Finland Ltd and is now being commercialized by Steady Energy Oy for district heating.

The WP7 is organised into several tasks, the first of which was to specify the input data required for modelling the cores. The document describing PRATIC core modelling for WP7 is (Prulhière, et al., 12/02/2025). The second task aims at benchmarking the neutronics results obtained with different codes used by different participants. The main purpose is to compare the results obtained by industry-grade simulations (nodal diffusion methods) with advanced simulations based on deterministic transport solution, and with High-Fidelity simulations based on Monte Carlo transport resolution. This deliverable reports the results obtained in this second task.

This task consists of two phases. The first phase aims to compare the results of the neutron codes only. To achieve this, the core was modelled in a hot zero power (HZP) configuration, where effects of thermohydraulics phenomena do not play a role. The second phase involves comparing the results obtained by neutronic codes coupled with thermohydraulic models. The core was simulated under hot full power (HFP) conditions. The deliverable is organised as follows: Section 7 specifies the calculations, while Section 8 describes the calculation methods used by the benchmark participants. Section 9 presents the obtained results, while Section 10 describes the final conclusions. Section 11 provides some outlooks, offering ideas for further scientific research topics.

7. Calculation specifications

The task 7.2.1, dedicated to the studies of the PRATIC core, was composed of two phases at the fuel Beginning of Life (BOL)[1]: this means that all the fuel composing the core was considered fresh (zero burn-up). The first phase focused on the Hot Zero-Power (HZP) state, while the second phase dealt with Hot Full-Power (HFP) conditions. The main objective of this task is to calibrate the discrepancies between the codes, and to assess the precision of the industrial-grade diffusion methods and advanced transport calculations, compared with a reference Monte Carlo simulation.

7.1. Phase 1: Beginning of Life, Hot Zero Power

The objective of this phase is to perform a code-to-code comparison in neutronics and reactor physics fields only. These exercises were therefore performed under HZP conditions, since thermo-hydraulic phenomena are negligible under these conditions.

Phase 1 is divided into several sub-parts, described in the following subsections.

7.1.1. Fuel Assembly lattice scale

The aim is to compare the neutron multiplication factor in an infinite lattice, k_{∞}, for each lattice pattern that will be used later in the PRATIC core, with a SERPENT reference. The operating conditions and calculation options considered are described in Table 1.

Table 1. Operating conditions and calculation options of Phase1, lattice scale sub-part.

Burnup	0 MWd/tHM
Cross section temperatures for all materials	600 K
Density related temperature for all materials	300°C
Geometric model	2D, One FA at a time
Boundary condition	Reflective
Neutron leakage model	No leakage

7.1.2. Core scale: Control rods worth

The objective is to benchmark the effective neutron multiplication factor, k_{eff}, of several core configurations against a SERPENT reference. All core configurations are simulated under the operating conditions described in Table 2 and differ only in the number of control rod banks inserted. The core power level is assumed to be zero; if this is not possible, a nominal power of 1% is assumed instead.
The configurations for control rod banks insertions are as follows:

- All rods out (ARO),
- Only bank G1 inserted,
- Only bank G2 inserted,
- Only bank G3 inserted,
- Only bank G4 inserted,
- Banks G1, G2, G3 and G4 inserted,

[1] In this document, the terms 'Beginning of Cycle' (BOC) and 'Beginning of Life' (BOL) will be used interchangeably.

- Bank S inserted,
- All Rods In (ARI).

These configurations make it possible to assess the efficiency of the control rod banks.

Table 2. Operating conditions of Phase 1, core calculations

Burnup	0 MWd/tHM
Cross section temperatures for all materials	600 K
Density related temperature for all materials	300°C
Geometric model	3D, Core
Core Power Level	3.5 MWth (1% NP)

7.1.3. Core scale: Radial and axial power maps

The role of this sub-part is to compare the 2D radial assembly-wise power maps and 1D axial core-wise power profile regarding to the reference. The operating conditions of these simulations are identical to those of the previous sub-part and are detailed in Table 2. These power distributions are calculated for several control rod bank insertion configurations:

- All rods out (ARO),
- Only bank G1 inserted,
- Only bank G2 inserted,
- Only bank G3 inserted,
- Only bank G4 inserted,
- Bank S inserted,
- All Rods In (ARI) (only for the 2D power maps).

The normalization of the 2D radial power maps is done considering the sum of each 2D map is the number of fuel assemblies (FAs): 57. The normalization of the 1D axial power profile is done considering the sum of each 1D profile is the number of axial mesh: 20. The recommended axial mesh to be completed by the benchmark participants is given in Table 3.

Table 3. Axial mesh recommended in the core active zone for the 1D axial profiles

Axial mesh #	bottom level [cm]	top level [cm]	average level [cm]
20	190.5333	200.5613	195.5473
19	180.5052	190.5333	185.5192
18	170.4771	180.5052	175.4912
17	160.4491	170.4771	165.4631
16	150.4210	160.4491	155.4350
15	140.3929	150.4210	145.4070
14	130.3649	140.3929	135.3789
13	120.3368	130.3649	125.3508
12	110.3087	120.3368	115.3228
11	100.2807	110.3087	105.2947
10	90.2526	100.2807	95.2666
9	80.2245	90.2526	85.2386
8	70.1965	80.2245	75.2105
7	60.1684	70.1965	65.1824
6	50.1403	60.1684	55.1544
5	40.1123	50.1403	45.1263
4	30.0842	40.1123	35.0982
3	20.0561	30.0842	25.0702
2	10.0281	20.0561	15.0421
1	0.0000	10.0281	5.0140

7.1.4. Core scale: Thermal feedback coefficients

This sub-part benchmarks the thermal feedback coefficients -inherent safety parameter of the core- predicted by different neutronic codes against the SERPENT reference solution. The operating conditions for the nominal cases are the same as those outlined in Table 2. To calculate these coefficients, a couple of three core configurations are simulated:

- In Hot Zero Power (HZP), All Rods Out (ARO) configuration:
  - Nominal case: cross section temperatures for all materials at 600 K; density related temperature for all materials at 300 °C.
  - Uniform fuel temperature increase: same than nominal case but the cross-section temperatures for all fuel materials are at 900 K rather than 600 K.
  - Coolant density reduction: same than nominal case but the density related temperature for water is 315 °C rather than 300 °C. At 155 bars pressure, the water density changes from 0.726 829 g/cm^3 (at 300 °C) to 0.693 249 g/cm^3 (at 315 °C).
- In HZP, All Rods In (ARI) configuration:
  - Nominal case: cross section temperatures for all materials at 600 K; density related temperature for all materials at 300 °C.
  - Uniform fuel temperature increase: same than nominal case but the cross-section temperatures for all fuel materials are at 900 K rather than 600 K.
  - Coolant density reduction: same than nominal case but the density related temperature for water is 315 °C rather than 300 °C. At 155 bars pressure, the water density changes from 0.726 829 g/cm^3 (at 300 °C) to 0.693 249 g/cm^3 (at 315 °C).

7.1.5. Core scale: Kinetic parameters

This sub-part permits to compare the kinetic parameter values predicted by different codes (diffusion, deterministic transport, MC) with a SERPENT reference. The operating conditions are the same as those outlined in Table 2. The kinetic parameters to be calculated as well as their definition are presented in Table 4, an illustration of a radioactive decay law is given in Figure 1.

Table 4. Definition of the kinetic parameters

Term	Definition	Unit	Equation
β_{eff}	Effective fraction of delayed neutrons	pcm	$\sum_i \beta_i = \beta_{eff}$
Λ_{eff}	Average neutron generation time	s	
β_i	Delayed neutron fraction of the group i		
λ_i	Radioactive decay constant of the group i	1/s	
T_i	radioactive period of the group i (T is the time after which half of the initial precursors have emitted a delayed neutron)	s	$T_i = \frac{\ln(2)}{\lambda_i}$
i	Group of precursors (it is generally 6 but it could be 8 for JEFF-3.1.1)		
ρ	Reactivity of the configuration	pcm	

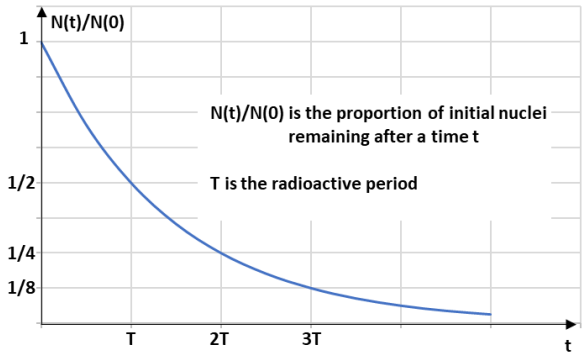

Figure 1. Illustration of a radioactive decay law

7.2. Phase 2: Beginning of Life, Hot Full Power

In this phase, the start-up core is modelled at hot full power (100% Nominal Power = 350 MWth) and zero burnup. Completing the task requires solving a coupled steady state problem between neutronics and thermohydraulics. Input data are given in the Tables 5 and 6. Fuel behaviour is modelled by a simplified manner, with fixed values given in Table 7.
This phase has two main parts, composed of two sub-parts.

I. In the first part, the system is modelled without xenon.
   I.1. In the first sub-part, the cumulate insertion of the control rod banks is given: 338 cm, which corresponds to the rod bank insertions described in Table 8 and Figure 2.
   I.2. In the second sub-part, the objective is to determine the critical insertion of the control rod banks.
II. In the second part, the system is modelled with xenon chain at equilibrium (saturated).
   II.1. In the first sub-part, the cumulate insertion of the control rod banks is given: 257 cm, which corresponds to the bank insertions described in Table 8 and Figure 3.

II.2. In the second sub-part, the objective is to determine the critical insertion of the control rod banks.

In addition to the critical insertion assessments described above (only for subsections I.2 and II.2), the following results are required for each subsection:

- Effective multiplication factor k_{eff},
- Axial power profile (normalized so that the mean of this distribution is equal to 1),
- Axial fuel temperature profile,
- Axial moderator temperature profile,
- Moderator output temperature (last value located at the top of the active area of the previous distribution),
- Assembly-wise 2D radial power map (normalized so that the mean of this distribution is equal to 1),
- Assembly-wise 2D radial fuel temperature map,
- Assembly-wise 2D radial moderator temperature map.

Optionally, the same calculations can be performed at a lower power level of 50% Nominal Power (175 MWth). In that case, the flow rates described in Table 5 don't change, the pressure of the primary loop stays at 155 bars, but **the moderator inlet temperature becomes 292.5°C**. The simplified thermal conditions described in Table 7 doesn't change. For the calculation 'I.1' (without xenon, fixed control rod insertion), the value of the cumulate insertion is 348 cm; for the calculation 'II.1' (xenon at saturation, fixed control rod insertion), the value of the cumulate insertion is 293 cm. The bank insertions corresponding to these cumulative values are given in Table 8, Figures 4 and 5, respectively.

Table 5. Flow rates

	Value	Unit	Remark
Nominal thermal power [NP]	3.50E+08	W	/
Moderator flow rate in the core (1)	1,550.00	kg/m^2/s	Effective core flow (not including bypass), assumed to be constant for each power level
Moderator cross section in the core at 300°C	1.41	m^2	Assuming that the moderator circulates around the fuel rods only (not in the guide tubes)
Moderator mass flow rate in the core (2)	2,185.39	kg/s	Calculated at 155 bars and 300°C, assumed to be constant for each power level
Density of water at 155 bars and 300°C	726.83	kg/m^3	Value considered in CRONOS2 / FLICA4 codes from CEA
Moderator volume flow rate in the core (3)	10,824.28	m^3/h	Calculated at 155 bars and 300°C, assumed to be constant for each power level

The reference value is the moderator flow rate (1). This value is assumed to be constant for each power level. The mass (2) and volume (3) flow rates are calculated based on the moderator flow rate (1): they are only given as indicators.

Table 6. Operating conditions at 100% Nominal Power

	Value	Unit	Remark
Moderator pressure	155.00	bars	/
Moderator inlet temperature [T_{in}]	285.00	°C	/
Moderator outlet temperature [T_{out}]	314.32	°C	average of meshes in the upper active plane, at the beginning of equilibrium cycle
Moderator 3D averaged temperature	302.30	°C	averaged 3D moderator density, converted into temperature, at beginning of equilibrium cycle
Moderator mid temperature (T_{in}+T_{out})/2	299.66	°C	/
Fuel 3D averaged temperature	470.55	°C	CRONOS2 calculations, at the beginning of equilibrium cycle

In Table 6, yellow highlighted values are obtained by a CRONOS2 calculation realized at CEA on the equilibrium cycle core (i.e., not the start-up core), with 'THERMIC/THERMOC' simplified models accounting for thermohydraulics effects. This is not a reference but can be considered as a good indicator.

Table 7. Thermal model and energy deposition

	Value	Unit	Remark
heat transfer coefficient of the fuel-clad gap	1,00	W/(cm^2×°C)	This value is assumed to be a constant (in space, in burnup and in power level)
Ratio of energy deposition in the fluid	2,50	%	/
energy produced by neutron capture in non-fissile areas	0,00	eV	It is assumed that neutron capture energy deposition is not considered in the reflector's areas and in the instrument and guide tubes (with or without control rod)

Table 8. Control rod insertions for several core configurations

Core Power (%NP)	Xenon	Insertion [cm]				
		Cumulative insertion	Bank G1	Bank G2	Bank G3	Bank G4
100	null	338	200	200	138	38
100	saturated	257	200	157	57	0
50	null	348	200	200	148	48
50	saturated	293	200	193	93	0

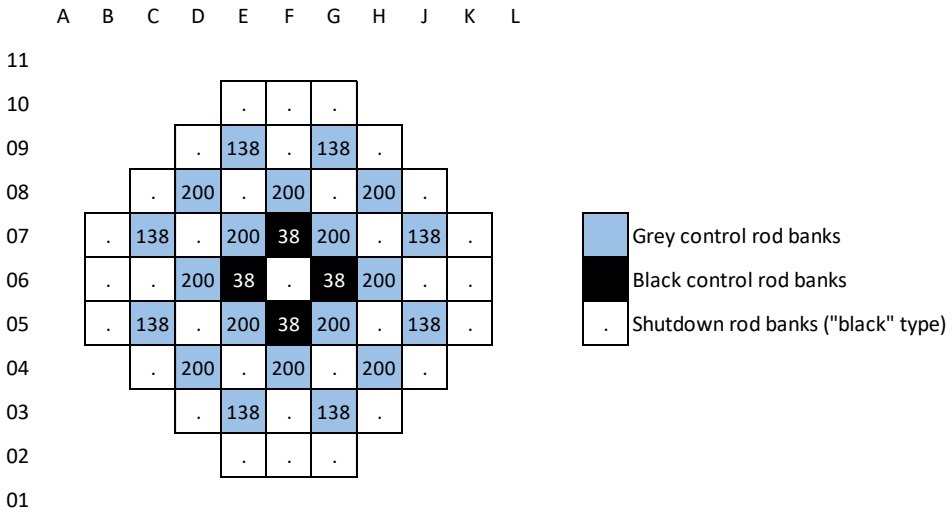

Figure 2. Control rod insertions at 100% NP, xenon null

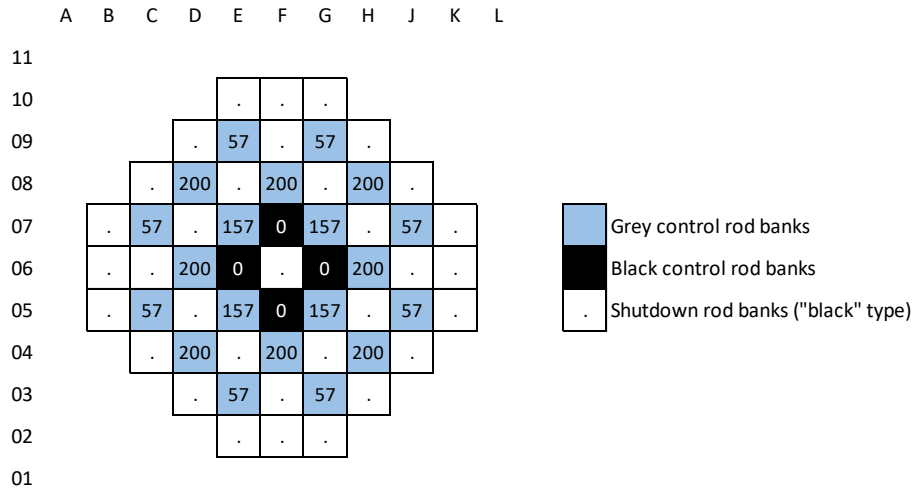

Figure 3. Control rod insertions at 100% NP, xenon saturated

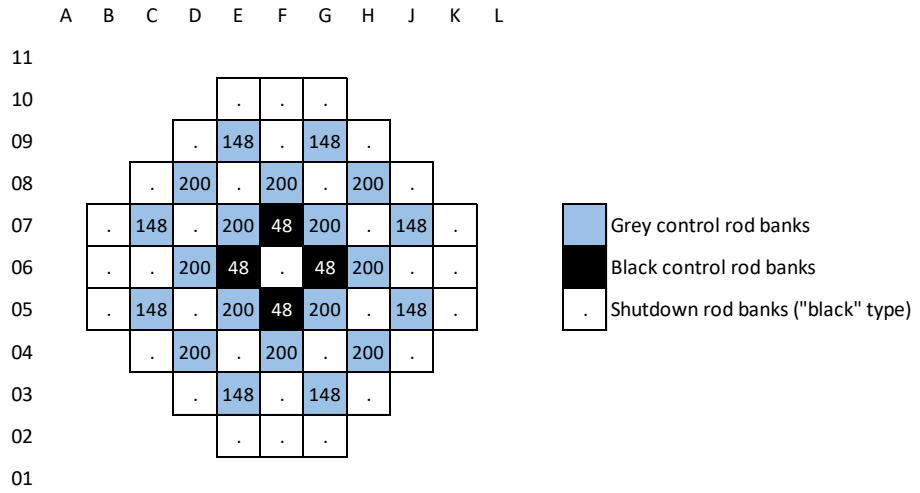

Figure 4. Control rod insertions at 50% NP, xenon null

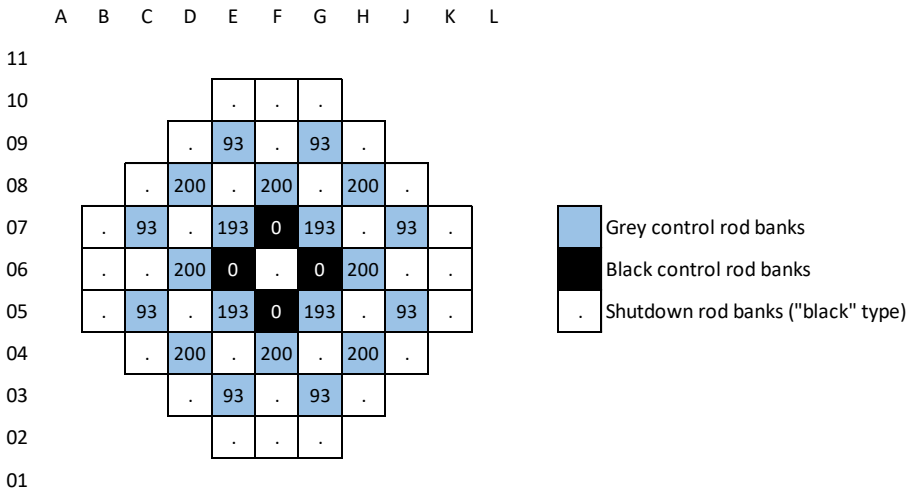

Figure 5. Control rod insertions at 50% NP, xenon saturated

Co-funded by the European Union
UK Research and Innovation
The Research Council of Norway
Project funded by

8.Description of the Calculation Routes

This chapter describes the calculation routes used by the different partners to produce the results presented in chapter 9. There are three main computational approaches: the Monte Carlo method (see Section 8.1), which provides reference results; advanced methods (see Section 8.2) based on solving the transport equation; and industry-standard methods (see Section 8.3) based on the diffusion equation.

8.1. Simulations Based on Monte Carlo Method

Three codes based on the Monte Carlo method were used in this benchmark: SERPENT2, which is considered the reference for this benchmark; TRIPOLI-4® and TRIPOLI-5, which provide additional Monte Carlo results for complementary analyses, giving confidence in the reference results.

8.1.1. Reference Results: SERPENT2 code

The Serpent code (Leppänen, Valtavirta, Rintala, & Tuominen, 2025), developed by VTT, Finland, was used to perform both 2D reflective lattice and 3D full-core calculations.

8.1.1.1. Model developed by KIT

For both phases of Task 7.2, the Serpent code v2.1.32 was used. Geometry and material specifications were taken from the PRATIC reference documentation (Prulhière, et al., 12/02/2025), and additional specifications given in Section 7.2.

Results were obtained using ENDF/B-VII.1 (Chadwick, et al., 2011) and JEFF-3.1.1 (Santamarina, Bernard, & Rugama, JEFF report 22, 2009) nuclear data libraries (NDLs) from the Serpent data repository. For the Phase 1 of the Task 7.2, under HZP conditions, the reference models entirely rely on Serpent stand-alone simulations. In contrast, for Phase 2 (HFP conditions), Serpent is coupled on a pin-by-pin basis to the subchannel thermohydraulic code Subchanflow (Imke & Sanchez, 2012), developed at KIT, Germany, providing a high-detail reference solution.

For the first phase, under HZP conditions, stand-alone Serpent models were developed, including 2D reflective and 3D full-core models. Figure 6 shows radial and axial cuts of the 3D Serpent model. Nearly default settings were used for both assembly-lattice and core models. For the 2D lattice, one eight-symmetry was considered using the *usym* card, while the core was modelled without symmetry considerations. In both cases, all cross sections were set to a fixed temperature of 600 K (.06c) as specified for the HZP condition, and no Doppler broadening was needed. For the thermal scattering law of H in H_2O, ENDF/B-VII.1-based solutions were evaluated exactly at 600 K, whereas for JEFF-3.1.1-based solutions, an interpolation (*therm* card) was applied using libraries at 574 K (.11t) and 624 K (.13t). Additionally, unresolved resonance probability table sampling was enabled (*set ures 1*). For the criticality source mode simulations, the 2D assembly cases were run using 10^6 neutron histories with 1,000 active and 100 inactive cycles. The full 3D core simulations used $2x10^6$ particles with 2,000 active and 500 inactive cycles. With these statistics, the 1 sigma uncertainty in the infinite and effective multiplication factors remained below 3 pcm.

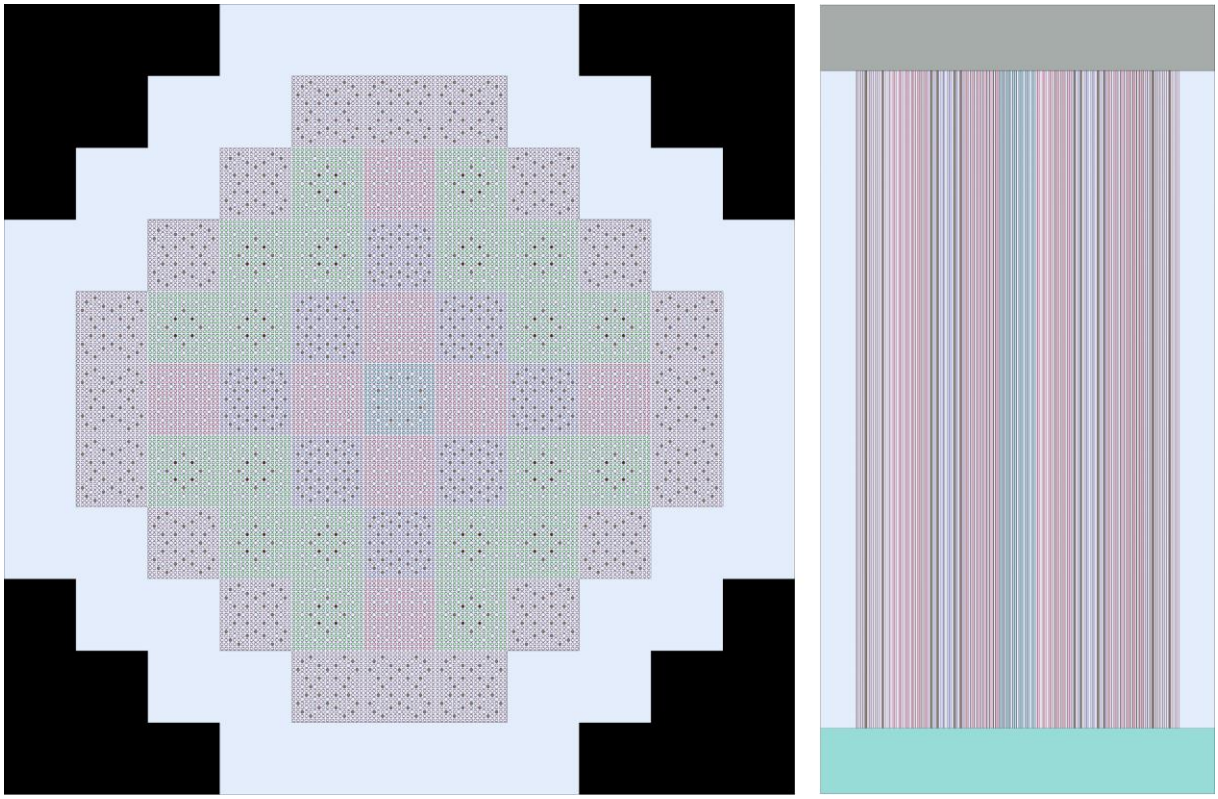

Figure 6. Radial and axial cuts of the PRATIC core model obtained from Serpent.

For the second phase, under HFP conditions, a thermohydraulic model was developed using the Subchanflow code v3.7.1. A high-detail pin-by-pin and subchannel-by-subchannel model was developed, as shown in Figure 7. The main assumptions and modelling considerations for the thermohydraulic calculations are summarized in Table 9.

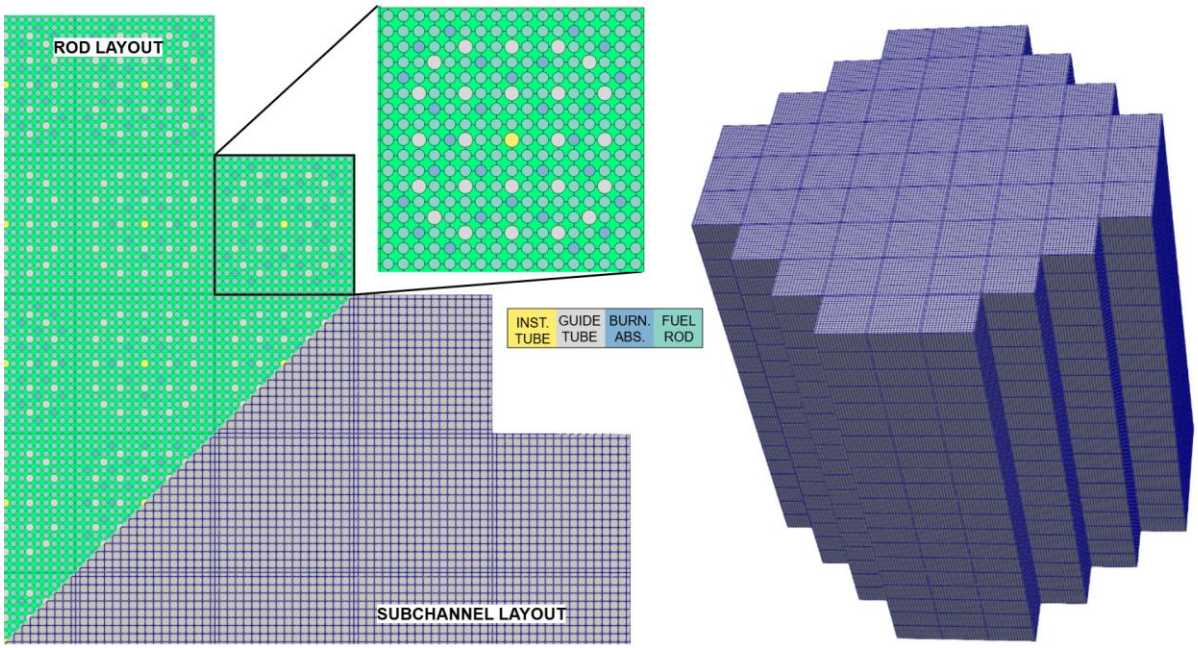

Figure 7. Subchanflow model of the PRATIC core. (Left) Rod and subchannel layout configuration. (Right) 3D subchannel layout representation.

Co-funded by the European Union
UK Research and Innovation
The Research Council of Norway
Project funded by

Table 9. Main assumptions and consideration for the Subchanflow model. (*) refers to specifications given in Section 7.2

Parameter	Value	Comment
Number of rods	16,473	17x17x57
Number of channels	18,468	18x18x57
Axial slices	20	-
Radial slices in the pellet	10	For solving the temperature radial profile
Radial slices in the cladding	2	For solving the temperature radial profile
Heat transfer correlation	Dittus-Boelter	-
Friction factor correlation	Blasius	Cladding wall friction
Water properties	IAPWS-IF97	-
Fuel conductivity	T-dependent	From specifications (*). BAs are considered to have the same conductivity properties.
Cladding conductivity	T-dependent	From specifications (*)
Gap heat transfer coefficient	10,000 W/K/m^2	From specifications (*)
Mass flow rate	2,185.39 kg/s	From specifications (*)
Outlet core pressure	15.5 MPa	From specifications (*)
Core inlet temperature	285.0 °C	From specifications (*)
Heat fraction to the moderator	2.5%	From specifications (*)
Power	350 MW	Distribution provided by Serpent
Thermal expansion	0	Not considered

For the coupled solution, pin power distribution is transferred to Subchanflow, which in return provides fuel temperature, coolant temperature, and coolant density for each fuel rod, and for each grid-element in the subchannel layout. This exchange is performed iteratively until a convergence criterion is met or until a predefined number of iterations is reached. In this analysis, the number of iterations was fixed to five, and Serpent's criticality source simulation were performed using 10^6 neutron histories with 1,000 active and 500 inactive cycles. With five fixed iterations, a reactivity difference of less than 3 pcm was obtained between the last two iterations. For the thermohydraulic quantities, differences below 4.0 K in fuel temperature, 0.2 K in coolant temperature, and 0.0005 g/cm^3 in coolant density were obtained, based on the L2-norm evaluated over the entire domain (Ferraro, et al., 2019).

Since a radial temperature profile is calculated within the fuel pellet, while a single fuel temperature value per rod slice is used in the neutronic model, an equivalent Doppler temperature was considered. This equivalent temperature is defined as a weighted average of the pellet centreline temperature (T_c) and the pellet outer surface temperature (T_s), according to:

$$T_{Doppler} = 0.3 \times T_c + 0.7 \times T_s$$

Two superimposed type 22 meshes (Serpent IFC files) were employed in Serpent to update the coolant and fuel parameters. Regarding cross sections, base cross sections at 600 K (.06c) with bounding temperatures between 600 K and 1,400 K (using the *tft* parameter of the *mat* card) were used for on-the-fly temperature adjustment based on Subchanflow results. For water, base cross section at 300 K (.03c) with bounding temperatures between 550 K and 620 K were applied. These bounding temperatures fully cover the temperature variations expected in the PRATIC core.

For the thermal scattering cross sections of hydrogen in H_2O, for ENDF/B-VII.1, interpolation between libraries at 550 K, 600 K, and 650 K (.55t, .60t, .65t) was considered. For JEFF-3.1.1, interpolation between libraries at 524 K, 574 K, and 624 K (.09t, .11t, 13t) was applied. Finally, for selected HFP cases, equilibrium xenon concentration was considered using the *set xenon 1* card, together with fuel material subdivision at the fuel assembly level and for each axial slice.

All Serpent and Serpent/SCF simulations were performed on the Horeka supercomputer. The authors gratefully acknowledge the computing time provided on the high-performance computer HoreKa by the National High-Performance Computing Center at KIT (NHR@KIT). This centre is jointly supported by the Federal Ministry of Education and Research and the Ministry of Science, Research and the Arts of Baden-Württemberg, as part of the National High-Performance Computing (NHR) joint funding program (https://www.nhr-verein.de/en/our-partners). HoreKa is partly funded by the German Research Foundation (DFG).

8.1.1.2. Model developed by ASNR

For the HZP phase, ASNR developed Monte-Carlo models using the Serpent code (Leppänen, Valtavirta, Rintala, & Tuominen, 2025), version 2.2.1. Calculations were performed with the JEFF-3.1.1 nuclear data library (Santamarina, Bernard, & Rugama, JEFF report 22, 2009). Two types of models were constructed: 2D reflective models for individual fuel assemblies and 3D models for the reactor core.

The geometrical models were built using the hot dimensions (300 °C) provided in the reference documentation (cf. (Prulhière, et al., 12/02/2025) and Section 7.2). For both the assembly and core models, a one-eighth symmetry was applied using the *usym* card. Material densities corresponding to 300 °C were also used.

All cross sections were set to a fixed temperature of 600 K (.06c), corresponding to the Hot Zero Power (HZP) conditions. Therefore, no Doppler broadening was required. For the thermal scattering law of hydrogen in water (H in H_2O), the data were interpolated to 600 K between the libraries available at 574 K (.11t) and 624 K (.13t) using the *therm lwtr* card. In addition, unresolved resonance probability table sampling was enabled using the option *set ures 1*.

The core models were used during the HZP phase to perform k_{eff} consistency checks against the predictions of models developed by KIT and HZDR and to investigate the impact of the thermal scattering law temperature on the calculated k_{eff}. The models were also provided to CEA to support further analyses aimed at understanding potential discrepancies between Monte Carlo codes.

For the criticality source mode simulations performed with the 2D assembly models, 1×10^6 particles per cycle were used, with 100 inactive cycles followed by 500 active cycles. For the calculations performed with the 3D core model, the same simulation parameters were applied, and convergence was not further optimized, as these calculations were intended only for rapid consistency checks and sensitivity analyses on k_{eff} rather than for detailed power distribution analyses. The resulting statistical uncertainties on all computed k_{eff} values were below 3 pcm for the implicit k_{eff} and below 6 pcm for the analog k_{eff}.

Consistency checks showed that the k_{eff} values calculated with the ASNR models for both assembly and core configurations are consistent with those obtained by KIT and HZDR. The observed discrepancies remain below three times the cumulative uncertainty of the Monte-Carlo calculations, defined as $\sqrt{\sigma_{model}^2 + \sigma_{ASNR}^2}$.

Views of the developed 3D core model are presented in Figure 8.

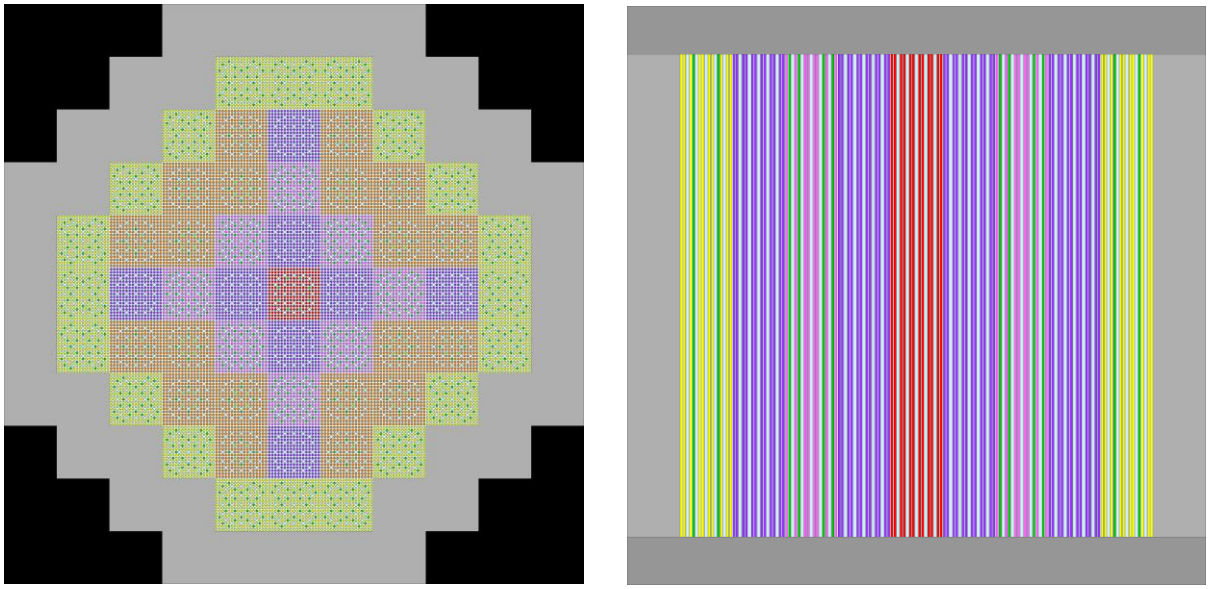

Figure 8 : Radial (left) and axial (right) cuts of ASNR's Serpent2 model of the PRATIC core

8.1.1.3. Model developed by PSI

In PSI's SERPENT v2.2.0 model, ENDF/B-VII.1, ENDF/B-VII.0 (Chadwick, et al., 2006) and JEFF-3.1.1 libraries are used to obtain the simulation results. The cross-section temperatures were set to 600 K. The material densities were set to the values at 300 °C in the specification document. Thermal scattering data at 600 K were applied for H in H_2O by interpolating between 574 K and 624 K. For the 2D assembly cases criticality calculations, 1,000,000 neutrons were used for 500 active and 150 inactive cycles; for the 3D full core calculations, 1,000,000 neutrons were used for 5,000 active and 500 inactive cycles. With above specification, the 1σ uncertainty in the k_∞ and k_{eff} remains below 5 pcm.

8.1.2. TRIPOLI-4®

TRIPOLI-4® is a Monte Carlo radiation transport code developed by the French Alternative Energies and Atomic Energy Commission (CEA) (Brun, et al., 2015). The role of the TRIPOLI-4® calculations in WP7 of the EASI-SMR project is to demonstrate how sensitive the results are to different types of Monte Carlo codes, which are free of modelling bias.

8.1.2.1. Model developed by CEA

CEA used the code TRIPOLI-4® in version 12.1 (Hugot, et al., 2024), based on the Monte Carlo method, for simulating the first phase of the task 7.2, in HZP conditions. The input decks of the code were generated using the INCA interface, based on the use of ROOT geometric model (Brun & Rademakers, 1997). Two NDLs were used: CEA-V5.1.2 based on JEFF-3.1.1 (Santamarina, Bernard, & Rugama, JEFF report 22, 2009) and ENDF/B-VII.1 (Chadwick, et al., 2011). According to the specifications, cross sections at 600 K were used for most of the configurations. This temperature was not tabulated in JEFF-3.1.1 so a linear interpolation of the cross sections was realized between the nearest tabulated temperatures: 574 K and 624 K. For the calculations with ENDF/B-VII.1, this interpolation was not necessary because 600 K is a tabulated temperature.

The epithermal broadening was treated using the following methods. For all isotopes except hydrogen in the water molecule, neutron elastic scattering was simulated using elastic cross sections between 10^{-5} eV and the colliding nucleus's thermal equilibrium energy, typically around 5 eV. Above this incident neutron energy, elastic scattering was described using the SVT (Sampling of the Velocity of the Target nucleus) model (Becker, 2010) until an upper energy threshold of $E_{SVT}^{maxi} = 400 \times k_B \times T \cong 20\ eV$ at 600 K.
For hydrogen linked to oxygen in the water molecule, isotope H1_H2O was used with its own thermal scattering law (TSL), also known as the $S(\alpha, \beta)$ matrix. This TSL was used in TRIPOLI-4® from 10^{-5} eV to an energy threshold of $E_{TSL}^{maxi} = 20\ eV$. Above these thresholds, the asymptotic scattering kernel is used instead for all the isotopes.

The unresolved energy range of the cross sections was treated using the probability tables (*TABPROB* keyword).

The simulations were set up in accordance with EDF model (see below). For the 2D assembly cases criticality calculations, 100,000 neutrons were used for 50,000 active and 400 inactive batches; for the 3D full core calculations, 100,000 neutrons were used for 100,000 active and 550 inactive batches. Batches were grouped in packets of size 200 to minimize the inter-batch correlations. The above simulation options allowed the 1σ uncertainty on k_{eff} to remain below 1.5 pcm for both assembly and full-core calculations. Kinetic parameters were calculated with the same model than EDF, presented in the following section.

8.1.2.2. Model developed by EDF

EDF performed Monte Carlo calculations only for the first benchmark phase, that is at HZP conditions, with version 4.12.1 of TRIPOLI-4® (Hugot, et al., 2024). The CEA-V5.1.2 nuclear data library, based on JEFF-3.1.1, was used. According to the common specifications, cross sections were evaluated at 600 K, but since data are not directly available at this temperature in the CEA-V5.1.2 library, a linear interpolation was necessary between data pre-tabulated at 574 K and 624 K. All geometries were generated using the ROOT package (Brun & Rademakers, 1997) (see Figure 9 for an example of core modelling at ARO conditions).

For the 2D assembly cases criticality calculations, 100,000 neutrons were used for 50,000 active and 400 inactive batches; for the 3D full core calculations, 100,000 neutrons were used for 100,000 active and 550 inactive batches. Batches were grouped in packets of size 200 to minimize the inter-batch correlations. The above simulation options allowed the 1σ uncertainty on k_{eff} to remain below 1.5 pcm for both assembly and full-core calculations.

Kinetic parameters for the ARO and ARI core configurations were evaluated via the Iterated Fission Probability (IFP) method (Hugot, et al., 2024), selecting 40 latent generations. In fact, after performing preliminary runs with a very large number of IFP latent generations (100), 40 was selected as a good compromise guaranteeing both close convergence of each parameter of interest to its asymptotic value (i.e., the one evaluated with 100 latent generations) and sufficiently low statistical uncertainty (which increases with the number of latent generations).

EDF simulations, since they were carried out with the same Monte Carlo code, the same NDL and with very similar calculation options than CEA simulations, allowed to verify the correctness of CEA TRIPOLI-4® model. Discrepancies between the two sets of results are very limited and fall within the interval of statistical acceptance (evaluated as $3\sqrt{\sigma_{EDF}^2 + \sigma_{CEA}^2}$).

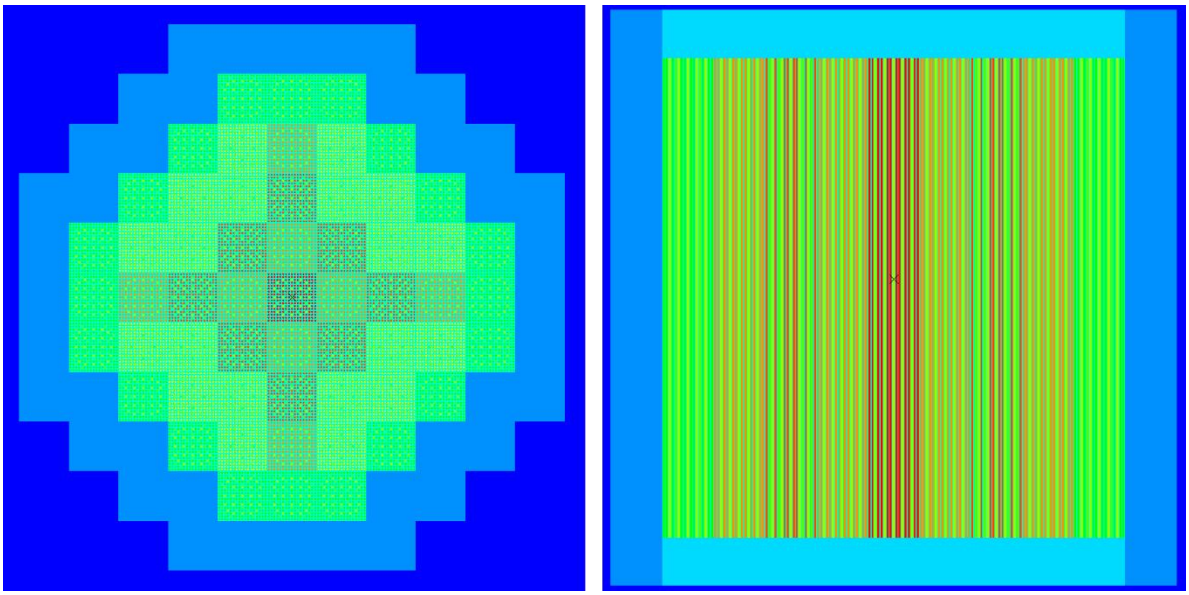

Figure 9. EDF TRIPOLI-4® ROOT model : radial (left) and axial (right) cuts of the PRATIC core at ARO conditions. The external dark blue region represents the void.

8.1.3. TRIPOLI-5

For the HZP phase, ASNR developed a second set of Monte-Carlo models using a development version (based on v0.1.0) of the TRIPOLI-5® code (Mancusi, et al., 2024), which is currently under development by CEA, ASNR and EDF. Calculations were performed with the ENDF-B/VII.1 nuclear data library (Chadwick, et al., 2011). Two types of models were constructed: 2D reflective models for individual fuel assemblies and 3D models for the reactor core.

The geometrical models were built using the hot dimensions (300 °C) provided in the reference documentation (Prulhière, et al., 12/02/2025). Both the assembly and core configurations were modelled in full geometry, without symmetry reduction. Material densities corresponding to 300 °C were also used.

All cross sections and the scattering law of hydrogen in water (H in H_2O) were set to a fixed temperature of 600 K, corresponding to the Hot Zero Power (HZP) conditions.

For the criticality source mode simulations performed with both the 2D assembly and the 3D core models, 3×10^6 particles per cycle were used, with 100 inactive cycles followed by 600 active cycles. These calculation parameters resulted in a statistical uncertainty of about 3 pcm on the computed k_{eff}.

Power distributions were evaluated using the *KappaFissionMEDMesh* score. Radial assembly power distributions were subsequently averaged by core quarter during post-processing.

Views of the developed 3D core model are presented in Figure 10.

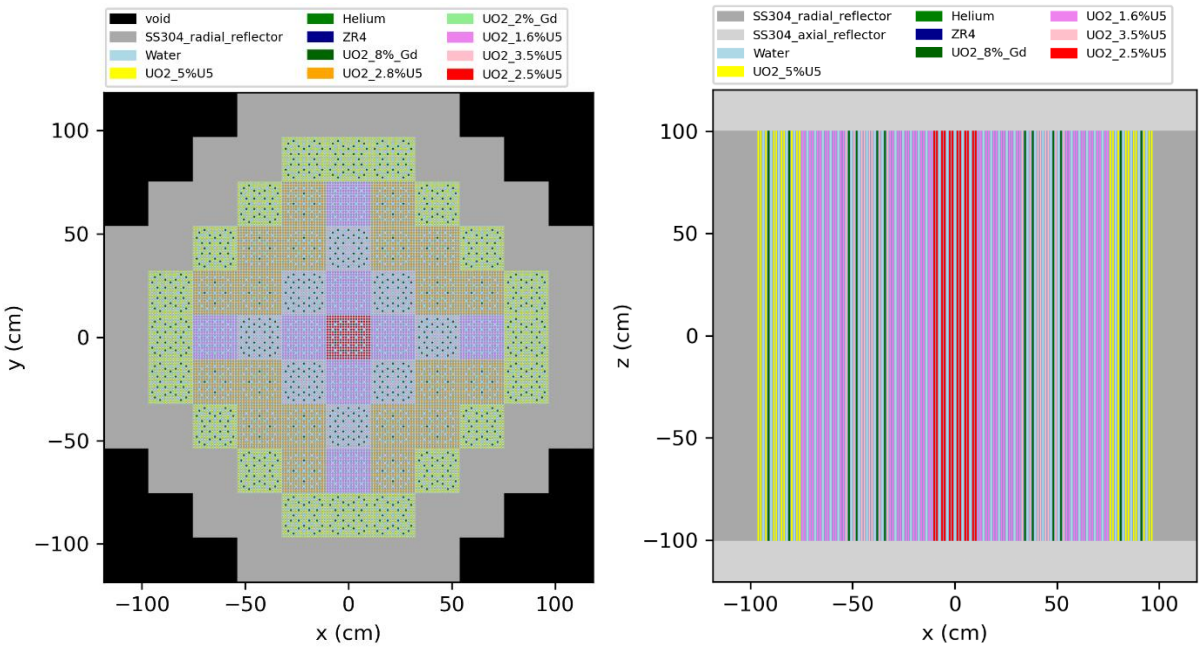

Figure 10 : Radial (left) and axial (right) cuts of ASNR's TRIPOLI-5® model of the PRATIC core

8.2. Simulations Based on Deterministic Transport

Deterministic transport methods are an advanced computational approach for simulating nuclear reactor cores. This method was employed by two computational codes in this benchmark.

8.2.1. APOLLO3®

APOLLO3 (Mosca, et al., 2023) is a multi-reactor code that combines the functionalities of lattice and core codes. It is developed by CEA, with the financial support of EDF and Framatome. This code incorporates a range of solvers and models, enabling various methods of neutronics and reactor physics calculations to be performed. The version APOLLO3-3.1 was used.

8.2.1.1. Model developed by CEA

Cross sections libraries were prepared using the SHEM-MOC (Santamarina, et al., 2009) calculation scheme, coupling a 281-groups energy mesh (Hfaiedh & Santamarina, 2005) for the self-shielding (P_{ij} method), and the method of characteristics (MoC) for the accurate neutron flux evaluation. The cross sections were pin-by-pin homogenized and condensed to a 8-groups energy mesh. After homogenization, an SPH equivalence step was performed to adjust the cross-sections. The cross sections of the reflectors were evaluated using a one-dimensional geometrical model representing the homogenized fuel and the reflector part. The cross sections were evaluated with a neutron transport solver in 281-group energy mesh, then condensed to a final energy mesh of 8 groups without any treatment. Finally, the neutron transport equation was solved using the Minaret solver (Moller & Lautard, 2011), based on the S8 discrete ordinates method. For simulations performed at HFP conditions, this solver was coupled to the internal thermohydraulic feedback model of APOLLO3® called Thedi (Patricot, Lenain, & Caron, 2019), in version 3.3.1. The thermo-physical properties used for fuel and cladding were those provided in the benchmark specification (Prulhière, et al., 12/02/2025), in particular the gap heat transfer

coefficient was simplified to a constant value of 1 W/(cm²×°C). The steam-water properties are taken from the FLICA4 thermo-hydraulic code developed by the CEA.

The simulations were realized using both JEFF-3.1.1 (Santamarina, Bernard, & Rugama, JEFF report 22, 2009) and ENDF/B-VII.1 (Chadwick, et al., 2011) NDLs.

8.2.1.2. Model developed by Framatome and EDF

The model developed by Framatome is based on simplified transport theory (SPN) with APOLLO3® code. It is based on the model described in Section 8.2.1.1 with a few changes. First, for lattice calculations, the previously mentioned SHEM-MOC scheme (Section 8.2.1.1) was used with JEFF-3.1.1 NDL but considering a refined spatial mesh and a higher order method within MOC solver (Linear Surface (Santandrea, Sanchez, & Mosca, 2008)). At the end of lattice calculation, cross sections were pin-by-pin homogenized and condensed to an 8-group energy mesh (2 groups were considered in Sections 8.3.1 and 8.3.2). Then, a SPH equivalence step was performed to adjust the cross sections during this homogenization/condensation phase. The reflectors' cross sections were obtained with the same procedure as the one described in Section 8.3.2 but with the 8-group SPN operator. Considering these cross sections at pin-scale, SPN equations on a 3D pin-by-pin mesh were solved with Minos solver embedded in APOLLO3® (Mosca, et al., 2023) on the full core model for each core configuration at HZP conditions.

8.2.2. nTRACER

nTRACER is a 3D neutron transport solver based on the method of characteristics (MoC) with the capability to couple with CTF subchannel code for thermohydraulics analysis and the capability of transient analysis (Jung, 2013). Nevertheless, the second phase of the Task 7.2 at HFP conditions was not treated with this code. In the first phase, which involved only neutron physics, the 2D assemblies and the 3D quarter core were modelled in nTRACER. At PSI, only ENDF/B-VII.0 nuclear data library is available for nTRACER. Serpent2 model was run with ENDF/B-VII.0 library to provide reference results for nTRACER.

In the nTRACER calculations, the ray tracing spacing is 0.05 cm. 16 azimuthal angles and 4 polar angles are used in 90°. The scattering order is 2. CMFD is applied to accelerate the convergence.

8.3. Simulations Based on Deterministic Diffusion

Industrial-grade simulations are generally based on the deterministic diffusion equation. Results obtained with six codes using this method have been compared during this benchmark.

8.3.1. APOLLO2 / CRONOS2

APOLLO2 (Sanchez, et al., 2010) is a two-dimensional lattice neutron transport code, developed by CEA, with the financial support of EDF and Framatome. The latest version APOLLO2.8-5 was used for this study. Several solvers are implemented in APOLLO2, permitting to define several calculation schemes. In our study, cross sections libraries were prepared using the same SHEM-MOC (Santamarina, et al., 2009) calculation scheme than for transport simulations with APOLLO3 (see Section 8.2.1). Results were produced with both JEFF-3.1.1 and ENDF/B-VII.1 NDLs. At the end of the lattice step, cross sections were pin-by-pin homogenized and

condensed to a 2-group energy mesh. A SPH equivalence step has permitted to adjust the cross sections during this homogenization/condensation phase.
The reflectors' effective cross sections were specially processed for two-group diffusion calculations. This involved using a one-dimensional geometrical model to solve the neutron transport equation with a 281-group energy mesh, followed by energy mesh condensation coupled with an albedo equivalence procedure. The cross sections of the two-group reflectors were adjusted until they satisfied the albedo reflective condition at the core-reflector interface.

All these cross sections were then transferred to the core calculation, realized with the CRONOS2.15 code (Lautard, Loubière, & Feudon-Magnaud, IAEA-TECDOC-678, 1992), consisting in the Minos solver (Lautard, Schneider, & Baudron, Mixed Dual Methods for Neutronic Reactor Core Calculations in the CRONOS System, 1999), solving the diffusion equation in a pin-by-pin spatial 3-D mesh (28 axial nodes: 20 in the active zone, and 4 nodes in both the upper and lower axial reflectors) and 2-group energy mesh. For HFP calculations, the Minos solver was coupled with THERMIC and THERMOC simplified thermohydraulics internal models. The thermo-physical properties used for fuel and cladding were those provided in the benchmark specification (Prulhière, et al., 12/02/2025), in particular, the gap heat transfer coefficient was simplified to a constant value of 1 W/(cm²×°C). The steam-water properties are taken from the FLICA4 thermo-hydraulic code developed by the CEA.
APOLLO2 and CRONOS2 are the codes that were used to design the PRATIC core.

8.3.2. APOLLO3®

APOLLO3® code has already been presented in Section 8.2.1.

The model developed by CEA for the simulations based on the diffusion theory with APOLLO3® code is the same than the APOLLO2 / CRONOS2 model. This model is described in Section 8.3.1. The only difference is that the APOLLO3 code uses the internal thermohydraulic Thedi-3.3.1 model (Patricot, Lenain, & Caron, 2019), whereas the CRONOS2 code uses the THERMIC and THERMOC simplified models to calculate the thermic properties of the fuel pin (THERMIC) and to calculate the core thermo-hydraulics properties (THERMOC). Thedi realizes both operations in one only code, and its thermohydraulics part is supposed to be more accurate than THERMOC.
The thermo-physical properties used for fuel and cladding were those provided in the benchmark specification (Prulhière, et al., 12/02/2025), in particular, the gap heat transfer coefficient was simplified to a constant value of 1 W/(cm²×°C). The steam-water properties are taken from the FLICA4 thermo-hydraulic code developed by the CEA.

8.3.3. CMS5 (CASMO5 / SIMULATE5)

The CMS5 code package (Core Management System version 5) is a suite of software tools developed by Studsvik Scandpower for simulation of light water reactors (LWRs). CASMO5 (Rhodes, Smith, & Lee, Sept. 10-14, 2006) and SIMULATE5 (Bahadir, Lindahl, & Studsvik Scandpower Ab, April 12-15 (2009)) are the two main components of the CMS5 package.

CASMO5 is a lattice physics code that performs detailed 2D transport calculations using the Method of Characteristics (MoC) in a fine energy-group structure, then condenses the cross sections into a coarser energy mesh. SIMULATE5 is a 3D core simulator that uses macroscopic cross-section data from CASMO5 to perform core-wide neutronics and thermohydraulics calculations.

Co-funded by the European Union
UK Research and Innovation
The Research Council of Norway
Project funded by

8.3.3.1. Model developed by ASNR

At the fuel assembly level, 2D reflective models were developed with CASMO5 (version 3.08.00L) for each of the five assemblies loaded in the core. CASMO5 calculations were performed using a Pij/MOC scheme. In the present study, 586/19 energy groups were used in the P_{ij} /MOC steps. Anisotropic scattering (P_N order) was treated using the P3 approximation, based on sensitivity analyses. Two nuclear data libraries were considered in the CASMO5 calculations: JEFF-3.1.1 and ENDF/B-VII.1.

Reflector modelling in CASMO5 was performed using a standard 1D approach, in which the neutron transport equation is solved with 95 energy groups along a radial traverse extending from the fuel to the reflector, with a vacuum boundary condition applied at the outer reflector boundary. Discontinuity factors are computed as the ratio of heterogeneous to homogeneous fluxes at the fuel/reflector interface.

The homogenized cross-section files were then generated using the S5C card with the TDN option, which enables branches where moderator temperature and density are decoupled. Sensitivity analyses were performed on the number of energy groups, leading to the choice of performing the 3D diffusion core calculations with 4 energy groups.

At the core level, SIMULATE5 (version 2.06.00L) calculations employed 20 axial nodes of 10 cm each and 4 radial nodes per fuel assembly. The axial reflectors were modelled with two axial nodes of 10 cm in each reflector. Infinite reflector boundary conditions were applied outside the radial and axial reflector blocks.

For the HZP conditions, the benchmark specifications were modelled in SIMULATE5 by disabling thermohydraulic feedback and enforcing the prescribed temperature and density conditions using the USE.BAS card:

'USE.BAS' 'DEN' 0.0 7.2683E-01 'TFU' 0.0 600.0 'TMO' 0.0 600.0 /

This methodology was selected to remain consistent with the standard application of the code for reactor cycle modelling. However, this approach introduces interpolation effects in the cross-section data.

For HFP conditions, the thermohydraulic (T/H) modeling of the core was handled by SIMULATE-5 through its integrated T/H feedback module. Each fuel assembly is divided into four quadrants, with no crossflow between assemblies. The 3D fuel temperatures are computed within the T/H module by solving the radial Fourier heat conduction equation, while thermodynamic quantities are evaluated using the NIST/ASME steam/water function library. The fuel-cladding gap thermal conductance was determined automatically by SIMULATE-5 through its built-in model.

The T/H conditions provided to the code are the coolant inlet temperature, the primary pressure, the core mass flow rate, the nominal core thermal power, and the core power level. The coolant inlet temperature is adjusted as a function of the core power level in accordance with the specifications (Prulhière, et al., 12/02/2025), and a uniform core inlet flow is assumed.

8.3.3.2. Model developed by KIT

For the PRATIC benchmark, preliminary sensitivity analyses were performed at KIT to identify the most suitable modelling options, balancing result accuracy with acceptable computational costs. These analyses focused on assessing the impact of different modelling choices, including

energy collapsing schemes at the lattice level and the multigroup representation adopted in nodal calculations. At the fuel-assembly (FA) level, two-dimensional reflective CASMO5 models were developed for each of the five assemblies loaded in the core, accounting for all possible combinations of rodded and un-rodded configurations. For the hot zero power (HZP) case, thermal expansion effects were neglected, and lattice transport calculations were carried out using the P3 approximation with a 19-group energy structure. The cross sections (XSs) generated by CASMO5 were subsequently homogenized and used in core diffusion calculations performed with the SIMULATE5 code, adopting a 4-group energy structure. This multigroup representation was selected for its improved capability to capture key features of the small cores considered in the PRATIC benchmark, such as high neutron leakage, strong sensitivity to spectral effects, and tight neutronic coupling. At the core level, SIMULATE5 calculations employed 20 axial nodes and 4 radial nodes per FA. Void boundary conditions were applied outside the radial reflector blocks as well as at the upper and lower boundaries of the axial reflectors. The 4-group diffusion model was also found to yield a more accurate representation of the axial power distribution near the top and bottom of the core, as the additional energy groups enable a better treatment of spectral hardening effects caused by neutron leakage at the core periphery. All CMS5 simulations performed at KIT were based on ENDF/B-VII.1 nuclear data.
The thermo-physical properties used in the simulations for fuel and cladding as well as the steam water properties were those calculated by the internal TH module of SIMULATE5 and this constitute a deviation with respect to the benchmark specifications.

8.3.3.3. Model developed by PSI

At PSI, CASMO5 was employed to perform 2D lattice calculations to generate macroscopic cross section data, which were used in SIMULATE5 to perform assembly level and full core level simulations. Multi-assembly calculations (“MxN” card) method in CASMO5 was used to generate macroscopic cross section data for the radial reflectors. Fixed moderator number density and material temperature are specified in the material card to decouple the moderator temperature and density. Calculations were performed using P3 approximation, 95 energy groups, with ENDF/B VII.1 nuclear data.

This model was only used in the first phase of Task 7.2, at HZP conditions.

8.3.4. CASMO5 / PARCS

In addition to the CMS5 analyses, ASNR performed simulations with the CASMO5/PARCS code sequence during the HZP phase.

CASMO5 provided homogenized two-group cross sections to the PARCS 3D diffusion code (Downar, Xu, & Seker, 2009) for full-core steady-state calculations. The same modelling parameters as in the CMS5 setup described in Section 8.3.3.1 were used (P_N order 3, 586/19 energy groups for the P_{ij}/MOC calculations, 1D radial reflector). The only difference was the activation of the fundamental mode option. Cross sections were generated using the same case matrix as for CMS5 (S5C card with the TDN option enabled).

In PARCS, the neutron mesh was defined with 4 radial nodes per fuel assembly (2x2 structure) and 20 axial nodes in the fuel region, complemented by two nodes in each axial reflector.

For the HZP conditions, the benchmark specifications were modelled in PARCS by disabling thermohydraulics feedback and enforcing the prescribed temperature and density conditions using the UNIF_TH card:

UNIF_TH 0.72683 326.85 326.85

Calculations were performed using a two-energy-group structure with both the ENDF/B-VII.1 and JEFF-3.1.1 nuclear data libraries.

8.3.5. HELIOS / DYN3D

8.3.5.1. Model developed by SSTC NRS

At SSTC NRS, a deterministic neutron and gamma transport code HELIOS-1.10 has been used for 2D lattice calculations to generate few-group macroscopic cross section libraries. HELIOS-1.10 relying on ENDF/B-VI nuclear data library (Dunford, 1991), that deviates from benchmark specifications regarding the defined nuclear data libraries ENDF/B-VII.1 or JEFF-3.1.1. The neutron transport calculation was carried out using the current coupling and collision probabilities (CCCP) method with a 190-group library. For the cross-section library preparation, preliminary sensitivity analyses were performed to identify the most suitable coupling orders, balancing result accuracy with acceptable computational costs.
At the core level, the DYN3D model employed that, based on a two-group diffusion approximation and a nodal expansion method. The DYN3D calculation code offers advanced and flexible capabilities for modelling reactor cores. The PRATIC core is represented as a set of square prisms with dimensions corresponding to the FA lattice pitch in the PRATIC core. The height of each prism corresponds to the active fuel length of the FA. In the reactor core layout, one calculation node is assigned per FA in the radial direction. The number of axial calculation nodes for modelling the fuel zone of the PRATIC core was set to 20. This yields an axial node height, which ensures that when CRs are in intermediate positions, geometric weighting is sufficient, thereby enabling accurate generation of homogenized nodal constants. To accurately account for neutron leakage beyond the reactor core boundaries, the model includes an additional peripheral row of 40 reflector cells in radial direction and two axial reflector layers. Void boundary conditions were applied outside the radial reflector.

The thermal hydraulic core model is represented by one-dimensional parallel coolant channels consisting of a fuel rod and proportional coolant flow. Each coolant channel is connected to one fuel element describing the average conditions. The channels are isolated, i.e., no cross flow between the channels is taken into account.

The thermo-hydraulics boundary conditions, provided by:

- pressure at core outlet,
- coolant temperature at the core inlet for each channel,
- total coolant mass flow rate through the core

correspond to Tables 5, 6 values. HTC of the fuel-clad gap is assumed to be a constant 1,00 W/(cm²×°C) regards to Table 7. The thermal conductivities for fuel and cladding are used according to ch.8.5.1 of “D7.1 Specifications of PRATIC fresh core at BOC conditions”.

The water and steam properties are presented by a software package based on the IFC67 formulation.

8.3.5.2. Model developed by UJV

Regarding the fuel and reflector lattice calculations, the HELIOS 2.04.01 code was used at UJV. Neutron and gamma transport were solved using 49-group microscopic cross-section library

based on ENDF/B-VII.1 (Chadwick, et al., 2011) employing the current coupling and collision probabilities (CCCP) method within discretized quarter-symmetry geometry (see for an example of discretized lattice), providing trade-off between solution accuracy and computational cost.

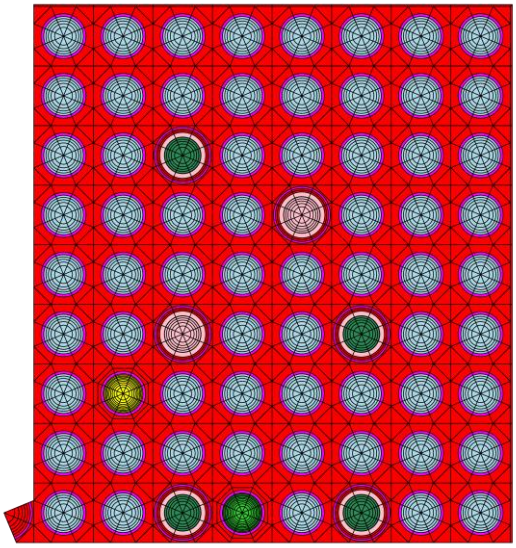

Figure 11. UJV HELIOS model of an example fuel lattice with grey control rods in.

At the core level, the DYN3D 3.3 code was used. The code computational models are based on a nodal expansion method and two-group neutron diffusion approximation for rectangular geometry. One radial square node is assigned to each fuel assembly, so the dimensions of the nodes correspond to the fuel assembly lattice pitch. There are also 40 radial reflector nodes around fuel assembly nodes with the same dimensions. The fuel region is divided into 20 axial nodes. Both top and bottom axial reflector parts are divided into 4 nodes each. Void boundary conditions were applied outside the radial and the axial reflector parts. For HFP calculations, the thermohydraulics module FLOCAL of the code DYN3D is used. The thermohydraulics boundary conditions as well as the thermo-physical properties used for fuel and cladding are those provided in the benchmark specification (Prulhière, et al., 12/02/2025) except cladding thermal conductivity, for which the internal method of DYN3D code based on MATPRO version 09 is used. The gap heat transfer coefficient is simplified to a constant value of 1 W/(cm²×°C). For water and steam properties internal IFC-67 package of water-steam tables is used.

8.3.6. WIMS / PANTHER

WIMS (Winfrith Improved Multigroup Scheme) is a collection of modules that can be combined to perform neutronic calculations ranging from simple homogenous cell calculations to complex whole core simulations. For this benchmark, the nuclear constants of the fuel and reflector constituents are generated by means of the lattice code WIMS 10 ru2 and the ENDF/B VII.1 library of microscopic data (XMAS scheme of 172 energy groups). The tables of nuclear properties are obtained by first solving the neutron transport problem with a method of characteristics considering 22 neutron groups, and further homogenization and condensation to 2 groups. For fuel assemblies, this sequence is applied in a 2D symmetry sector with translational boundary conditions. The reflector constants are derived from a pseudo-1D supercell setup with 2 fuel assemblies and void boundary conditions on the outer side.

PANTHER is a few-group neutron diffusion reactor code distributed by ANSWERS. The flux distribution is calculated using a nodal method on a coarse 3D mesh. The fine-grained power

distribution is accessible through pin power reconstruction. PANTHER has a built-in module for the calculation of thermohydraulic feedback, that is derived from VIPRE-01 and that relies on the concept of an equivalent pin in a closed channel at constant pressure. PRATIC core simulations are performed with PANTHER 5.6.6 on a single assembly model with 4 planar nodes per channel.

This model was only used in the first phase of Task 7.2, at HZP conditions.

9. Presentation and discussion of results obtained

9.1. Code-to-Code Benchmarking at HZP State

9.1.1. Serpent2 reference solution

The initial step of the benchmark consisted of 2D infinite, reflected assembly calculations, in which the five different fuel assembly types of the PRATIC core were modelled under various control rod conditions. Table 10 presents the infinite multiplication factors calculated with Serpent for the five FA types.

Table 10. Serpent infinite multiplication factor for the different FA types. Number in parentheses indicate the ±1-sigma uncertainty in the last digit of the number.

Fuel assembly type	Control Rod Insertion	ENDF/B-VII.1 Kinf	JEFF-3.1.1 Kinf
UOX 1.6%	No Black (AIC)	1.18238 (2) 0.72672 (2)	1.18083 (2) 0.72370 (2)
UOX 2.5% + 8 BAs w. 8%Gd2O3	No Black (AIC)	1.17053 (2) 0.80834 (2)	1.16932 (2) 0.80494 (3)
UOX 2.8% + 4 BAs w. 2% Gd2O3 + 4 BAs w. 8% Gd2O3	No Grey (AIC + steel) Black (AIC)	1.22112 (2) 0.93616 (3) 0.85226 (3)	1.21986 (2) 0.93318 (3) 0.84880 (3)
UOX 3.5% + 36 BAs w. 8%Gd2O3	No Grey (AIC + steel)	0.93362 (3) 0.77251 (3)	0.93252 (3) 0.76991 (3)
UOX 5.0% + 28 BAs w. 8%Gd2O3	No Black (AIC)	1.12696 (3) 0.87038 (3)	1.12555 (3) 0.86650 (3)

As a second step under HZP conditions, the full 3D PRATIC core was simulated for different control rod bank configurations to compare global parameters such as multiplication factors and kinetic parameters, as well as power distributions in the core. Table 11 summarizes the multiplication factors obtained for each case, together with the corresponding control rod worth (CRW), calculated relative to the ARO condition.

Table 11. Serpent effective multiplication factor for different core configurations.

Core configuration	ENDF/B-VII.1 Keff and CRW [pcm]		JEFF-3.1.1 Keff and CRW [pcm]	
ARO	1.08267 (1)	/	1.08203 (1)	/
Only bank G1 inserted	1.05016 (1)	-2859 (2)	1.04932 (1)	-2881 (2)
Only bank G2 inserted	1.07134 (1)	-977 (1)	1.07068 (1)	-980 (1)
Only bank G3 inserted	1.05225 (1)	-2670 (2)	1.05146 (1)	-2687 (1)
Only bank G4 inserted	1.06477 (1)	-1553 (1)	1.06428 (1)	-1541 (2)
G1, G2, G3, G4 inserted	0.97066 (1)	-10658 (2)	0.96958 (1)	-10719 (2)
Only S bank inserted	0.95079 (1)	-12811 (2)	0.94945 (1)	-12905 (2)
ARI	0.79872 (1)	-32835 (2)	0.79618 (1)	-33182 (2)

Core power distributions were evaluated at the fuel assembly level, considering 20 axial slices over the active core height. Figure 12 and Figure 13 show the axially integrated radial power distributions for the different bank configurations. Figure 14 presents the axial power distributions.

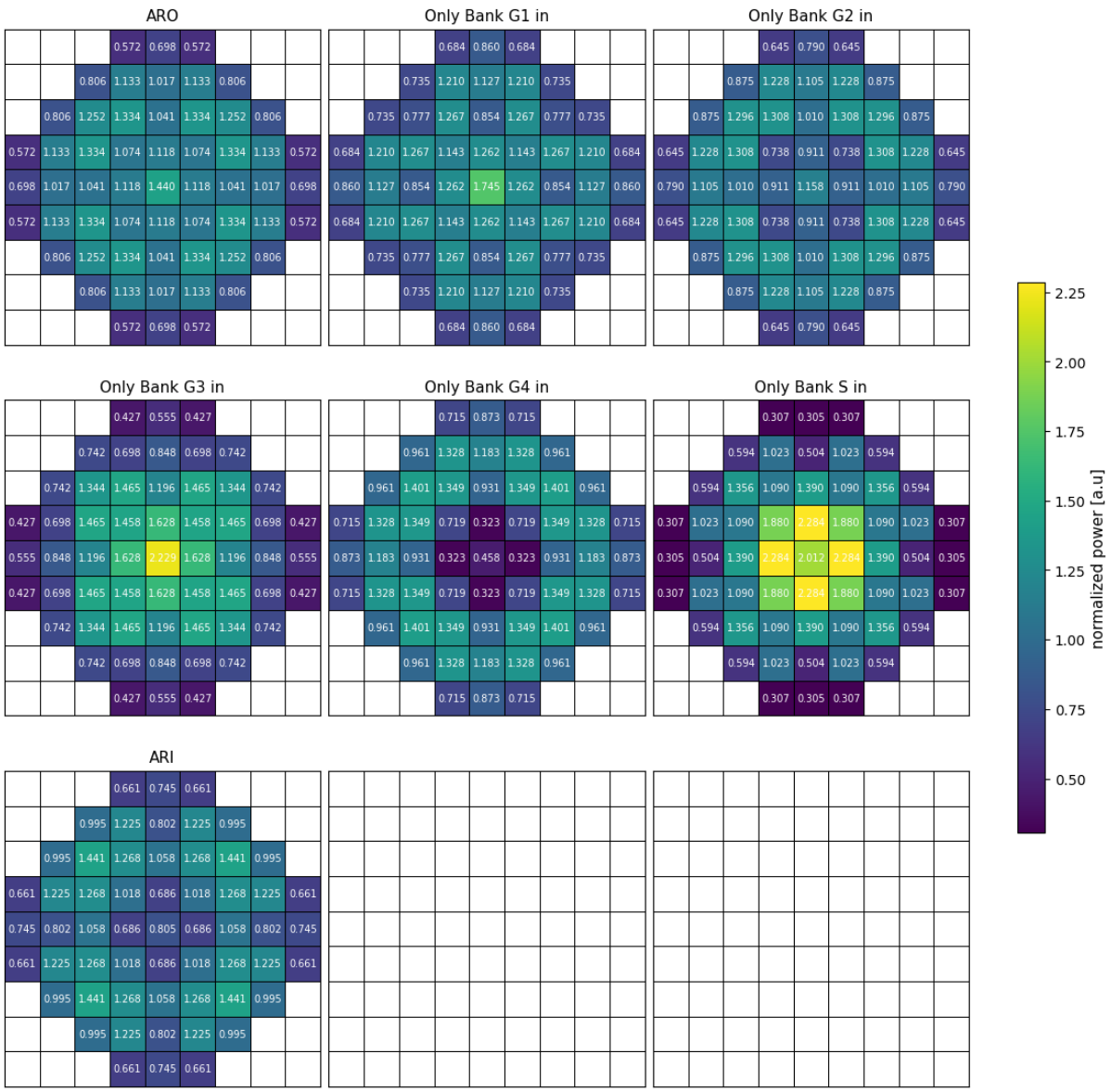

Figure 12. Serpent normalized radial power map distributions obtained with ENDF/B-VII.1 for different control rod configurations. The normalization is performed such that the sum of all power values equals the total number of fuel assemblies (57). Power is calculated using Serpent's detector with macroscopic reaction number -8, which accounts for the total fission energy production. The maximum uncertainty (1-sigma) in the values is 0.033%.

Co-funded by the European Union
UK Research and Innovation
The Research Council of Norway
Project funded by

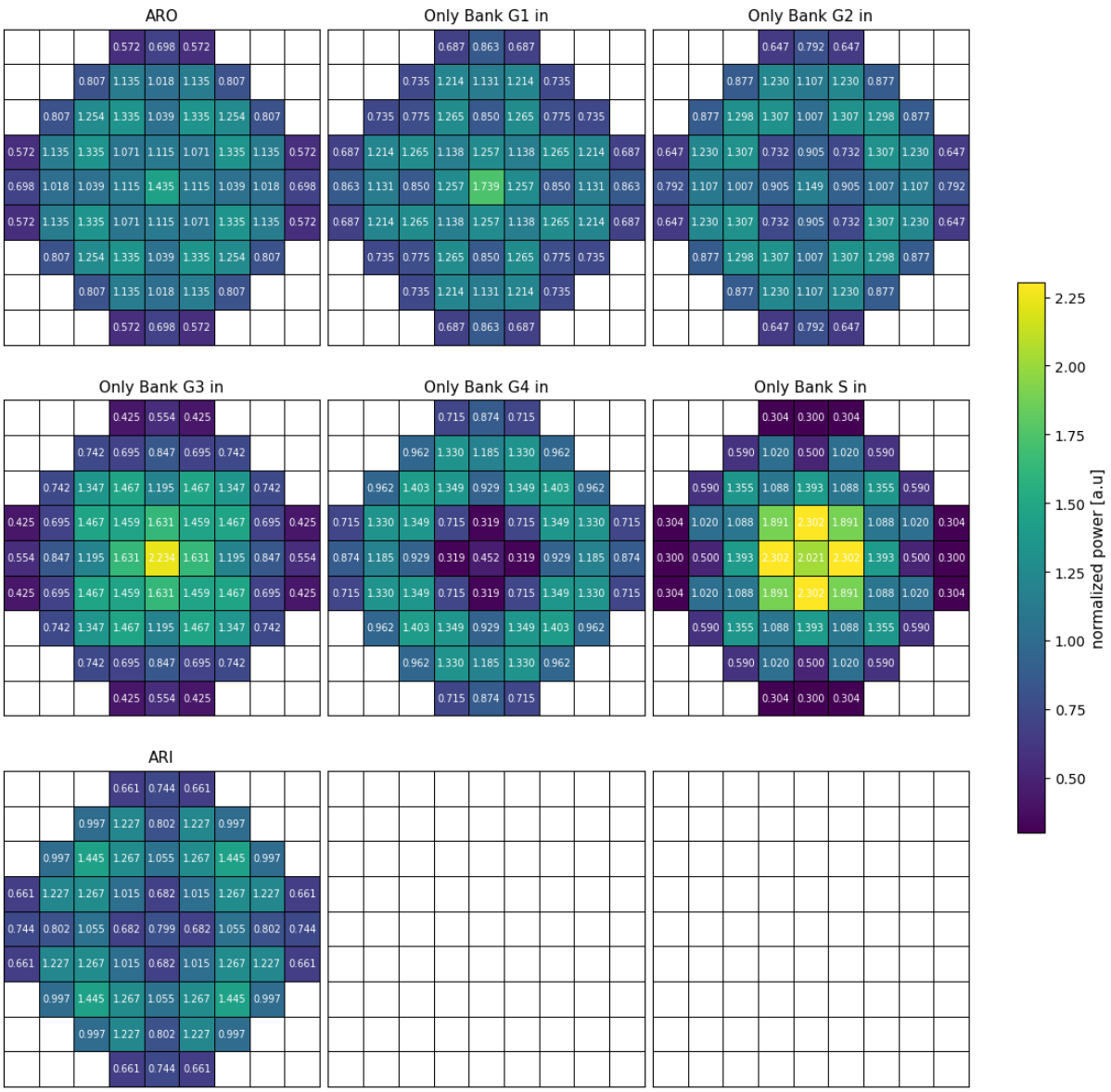

Figure 13. Serpent normalized radial power map distributions obtained with JEFF-3.1.1 for different control rod configurations. The normalization is performed such that the sum of all power values equals the total number of fuel assemblies (57). Power is calculated using Serpent's detector with macroscopic reaction number -8, which accounts for the total fission energy production. The maximum uncertainty (1-sigma) in the values is 0.032%.

Co-funded by the European Union
UK Research and Innovation
The Research Council of Norway
Project funded by

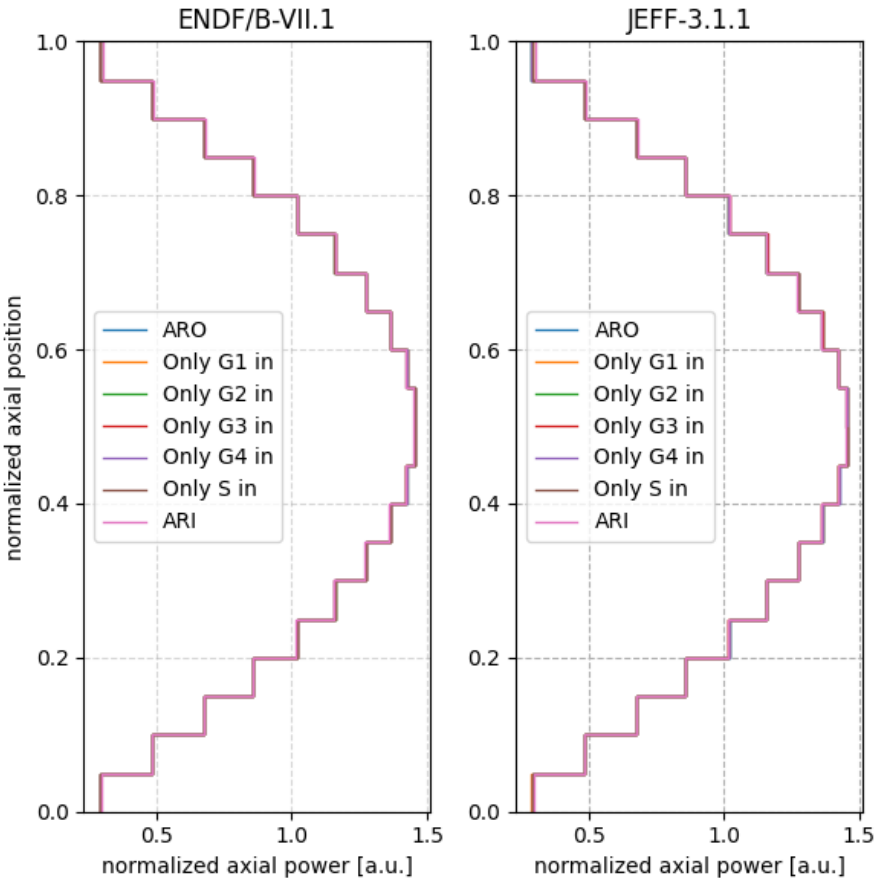

Figure 14. Serpent axial power distribution. The 20 axial slices are equally divided. The normalization is performed such that the average value equals 1. Power is calculated using Serpent's detector with macroscopic reaction number -8, which accounts for the total fission energy production. The maximum uncertainty (1-sigma) in the values is 0.027%.

As a final step under the HZP conditions, safety-relevant kinetic parameters were calculated for ARO and ARI conditions. Reactivity coefficients were determined by varying the fuel or coolant temperatures and evaluating the resulting change in k_{eff} relative to the HZP reference condition. For the fuel temperature reactivity coefficient, the fuel temperature was increased to 900 K. For the coolant temperature reactivity coefficient, the coolant density was reduced to its corresponding value at 315 °C, while the coolant temperature itself was kept constant. Table 12 summarizes the calculated values, together with additional kinetic parameters, as the effective delayed neutron fraction, and delayed neutron fractions and decay constants for each precursor group.

Table 12. Temperature feedback coefficients and kinetic parameters obtained with Serpent using the ENDF/B-VII.1 and JEFF-3.1.1 for ARO and ARI control rod configurations. Numbers in parentheses indicate the 1-sigma standard deviation.

Parameter	ENDF/B-VII.1		JEFF-3.1.1	
	ARO	ARI	ARO	ARI
fuel temp. coef. (pcm/K)	-2.353 (0.2%)	-3.262 (0.3%)	-2.352 (0.2%)	-3.282 (0.3%)
coolant temp. coef. (pcm/K)	-48.1 (0.2%)	-104.0 (0.2%)	-48.5 (0.2%)	-105.7 (0.2%)
β_{eff} (pcm)	702.6 (0.03%)	708.8 (0.03%)	723.5 (0.03%)	731.8 (0.03%)
Λ_{eff} (μs)	24.3 (0.01%)	22.7 (0.01%)	24.4 (0.01%)	22.8 (0.01%)
β_i	2,24298E-04 (0.16%) 1,19570E-03 (0.07%) 1,16767E-03 (0.07%) 2,71413E-03 (0.05%) 1,21776E-03 (0.07%) 5,06601E-04 (0.10%) - -	2,18741E-04 (0.19%) 1,18261E-03 (0.08%) 1,16355E-03 (0.08%) 2,73889E-03 (0.05%) 1,26106E-03 (0.08%) 5,23495E-04 (0.12%) - -	2,13139E-04 (0.16%) 1,04604E-03 (0.07%) 6,14420E-04 (0.10%) 1,36126E-03 (0.06%) 2,32275E-03 (0.05%) 7,79945E-04 (0.09%) 6,50234E-04 (0.10%) 2,47412E-04 (0.15%)	2,07005E-04 (0.18%) 1,03716E-03 (0.08%) 6,04797E-04 (0.11%) 1,35668E-03 (0.07%) 2,33174E-03 (0.06%) 8,28069E-04 (0.09%) 6,77256E-04 (0.10%) 2,75195E-04 (0.16%)
λ_i $(1/s)$	1,33556E-02 (0.001%) 3,25976E-02 (0.001%) 1,21088E-01 (0.0005%) 3,05956E-01 (0.001%) 8,62124E-01 (0.002%) 2,89555E+00 (0.003%) - -	1,33624E-02 (0.001%) 3,25514E-02 (0.001%) 1,21186E-01 (0.0006%) 3,06918E-01 (0.001%) 8,65538E-01 (0.002%) 2,90727E+00 (0.004%) - -	1,24667E-02 (4e-7%) 2,82917E-02 (8e-7%) 4,25244E-02 (~0) 1,33042E-01 (4e-7%) 2,92467E-01 (~0) 6,66488E-01 (4e-7%) 1,63478E+00 (~0) 3,55460E+00 (~0)	1,24667E-02 (4e-7%) 2,82917E-02 (8e-7%) 4,25244E-02 (~0) 1,33042E-01 (4e-7%) 2,92467E-01 (~0) 6,66488E-01 (4e-7%) 1,63478E+00 (~0) 3,55460E+00 (~0)

9.1.2. Selected parameters for code benchmarking

9.1.2.1. Multiplication Factor of Fuel Assemblies in Infinite Lattice

The benchmark participants calculated the infinite lattice neutron multiplication factors for all the fuel assembly patterns present in the PRATIC core. The operating conditions have been reported in Table 1. The differences in reactivity compared to the reference result provided by KIT/SERPENT2 are shown in Tables 13 and 15 for the ENDF/B7.1 NDL, and in Tables 14 and 16 for the JEFF-3.1.1 NDL. These differences are calculated using the following formula:

$$\Delta\rho = \frac{k_{\infty}^{participant} - k_{\infty}^{reference}}{k_{\infty}^{participant} \times k_{\infty}^{reference}} \times 1.0E^{+5}$$

These results are illustrated in Figure 15 for ENDF/B7.1, and Figure 16 for JEFF-3.1.1.

Table 13. ENDF/B-7.1. Reactivity differences (in pcm) of fuel assembly patterns in an infinite lattice.

Fuel assembly name and type	Control Rod Insertion	CEA-TRIPOLI4	ASNR-TRIPOLI5	CEA-APOLLO3	ASNR-CASMO5	KIT-CASMO5	PSI-CASMO5	SSTC NRS-HELIOS	TRACTEBEL-WIMS10	PSI-nTracer	UJV-HELIOS
Central = UOX 2,5% ; 8 Gd pins w/ 8% Gd2O3	No	13	15	58	-77	-72	7	120	-394	-138	-42
Central = UOX 2,5% ; 8 Gd pins w/ 8% Gd2O3	Black (AIC)	55	8	294	119	92	252	-621	-144	-398	1423
Internal 1 = UOX 3,5% ; 36 Gd pins w/ 8% Gd2O3	No	34	7	37	-34	-64	76	465	-564	-312	-5
Internal 1 = UOX 3,5% ; 36 Gd pins w/ 8% Gd2O3	Grey (AIC + steel)	62	3	81	142	75	249	-72	-383	-414	921
Internal 2 = UOX 1,6% ; 0 Gd pin	No	0	11	30	-116	-123	-33	86	-379	-38	-76
Internal 2 = UOX 1,6% ; 0 Gd pin	Black (AIC)	75	13	498	32	30	257	-480	-374	-542	1745
External 1 = UOX 5,0% ; 28 Gd pins w/ 8% Gd2O3	No	19	3	-7	-94	-84	37	178	-423	-180	-64
External 1 = UOX 5,0% ; 28 Gd pins w/ 8% Gd2O3	Black (AIC)	44	-12	62	108	53	250	-657	-221	-288	1018
External 2 = UOX 2,8% ; 4 Gd pins w/ 2% Gd2O3 + 4 Gd pins w/ 8% Gd2O3	No	7	9	52	-89	-87	3	91	-320	-103	-49
External 2 = UOX 2,8% ; 4 Gd pins w/ 2% Gd2O3 + 4 Gd pins w/ 8% Gd2O3	Grey (AIC + steel)	34	15	26	46	9	153	-366	-178	-283	842
External 2 = UOX 2,8% ; 4 Gd pins w/ 2% Gd2O3 + 4 Gd pins w/ 8% Gd2O3	Black (AIC)	56	14	182	103	69	242	-674	-83	-347	1316

Table 14. JEFF-3.1.1. Reactivity differences (in pcm) of fuel assembly patterns in an infinite lattice.

Fuel assembly name and type	Control Rod Insertion	CEA-TRIPOLI4	EDF-TRIPOLI4	CEA-APOLLO3	ASNR-CASMO5	FRAMATOME-APOLLO3	CEA-APOLLO2	PSI-SERPENT
Central = UOX 2,5% ; 8 Gd pins w/ 8% Gd2O3	No	62	63	84	-72	18	-125	10
Central = UOX 2,5% ; 8 Gd pins w/ 8% Gd2O3	Black (AIC)	160	157	365	114	-20	-318	1
Internal 1 = UOX 3,5% ; 36 Gd pins w/ 8% Gd2O3	No	85	83	41	-78	-24	-289	7
Internal 1 = UOX 3,5% ; 36 Gd pins w/ 8% Gd2O3	Grey (AIC + steel)	151	149	123	83	-21	-372	-15
Internal 2 = UOX 1,6% ; 0 Gd pin	No	59	59	72	-92	54	-42	9
Internal 2 = UOX 1,6% ; 0 Gd pin	Black (AIC)	170	170	568	24	-45	-326	-10
External 1 = UOX 5,0% ; 28 Gd pins w/ 8% Gd2O3	No	69	68	10	-114	-11	-181	-5
External 1 = UOX 5,0% ; 28 Gd pins w/ 8% Gd2O3	Black (AIC)	142	141	124	72	-9	-324	-4
External 2 = UOX 2,8% ; 4 Gd pins w/ 2% Gd2O3 + 4 Gd pins w/ 8% Gd2O3	No	59	59	84	-78	29	-46	0
External 2 = UOX 2,8% ; 4 Gd pins w/ 2% Gd2O3 + 4 Gd pins w/ 8% Gd2O3	Grey (AIC + steel)	117	117	86	42	9	-295	3
External 2 = UOX 2,8% ; 4 Gd pins w/ 2% Gd2O3 + 4 Gd pins w/ 8% Gd2O3	Black (AIC)	142	144	243	88	-12	-329	9

To summarise these results, the differences in reactivity have been averaged by their layout type, in Table 15 and Table 16.

Table 15. ENDF/B-7.1. Reactivity differences (in pcm) of fuel assembly patterns averaged by layout type.

	CEA-TRIPOLI4	ASNR-TRIPOLI5	CEA-APOLLO3	ASNR-CASMO5	KIT-CASMO5	PSI-CASMO5	SSTC NRS-HELIOS	TRACTEBEL-WIMS10	PSI-nTracer	UJV-HELIOS
FA w/o CR, 0 or 8 Gd pins	7	12	47	-94	-94	-8	99	-364	-93	-56
FA w/o CR, 28 or 36 Gd pins	27	5	15	-64	-74	56	321	-494	-246	-34
FA w/ grey CR, 8 Gd pins	34	15	26	46	9	153	-366	-178	-283	842
FA w/ grey CR, 36 Gd pins	62	3	81	142	75	249	-72	-383	-414	921
FA w/ black CR, 0 or 8 Gd pins	62	12	325	85	64	250	-592	-200	-429	1494
FA w/ black CR, 28 Gd pins	44	-12	62	108	53	250	-657	-221	-288	1018

Table 16. JEFF-3.1.1. Reactivity differences (in pcm) of fuel assembly patterns averaged by layout type.

	CEA-TRIPOLI4	EDF-TRIPOLI4	CEA-APOLLO3	ASNR-CASMO5	FRAMATOME-APOLLO3	CEA-APOLLO2	PSI-SERPENT
FA w/o CR, 0 or 8 Gd pins	60	60	80	-81	34	-71	6
FA w/o CR, 28 or 36 Gd pins	77	76	26	-96	-18	-235	1
FA w/ grey CR, 8 Gd pins	117	117	86	42	9	-295	3
FA w/ grey CR, 36 Gd pins	151	149	123	83	-21	-372	-15
FA w/ black CR, 0 or 8 Gd pins	158	157	392	75	-26	-324	0
FA w/ black CR, 28 Gd pins	142	141	124	72	-9	-324	-4

The results of tables 15 and 16 are illustrated in Figure 15 and Figure 16.

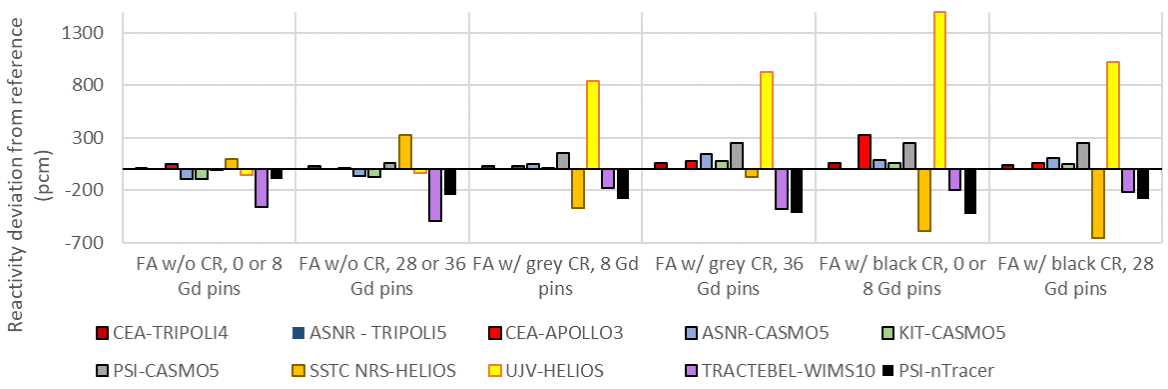

Figure 15. ENDF/B7.1. Reactivity deviation from reference (infinite lattice calculations).

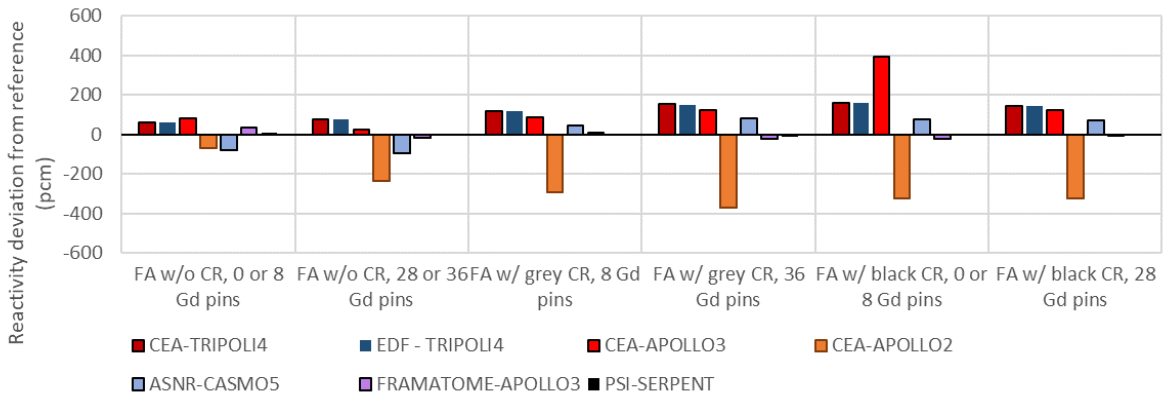

Figure 16. JEFF-3.1.1. Reactivity deviation from reference (infinite lattice calculations).

The results obtained with SERPENT2 by PSI fit exactly the reference results. This was also confirmed by HZDR and ASNR SERPENT2 results, that are not represented here. The results obtained with other codes based on Monte Carlo method (TRIPOLI4® and TRIPOLI5) are very close to the reference results obtained with SERPENT2, which is also a code based on the Monte Carlo method to evaluate the neutron transport. The deviations between Monte Carlo results never exceed 75 pcm with ENDF/B7.1 and are contained below 170 pcm with JEFF-3.1.1. There is a better accordance between TRIPOLI5 and SERPENT2 than between TRIPOLI4® and SERPENT2.

The results obtained using APOLLO3® and CASMO5 are in very good agreement with those obtained using SERPENT2. Apart from one case, all of these results show a reactivity difference with the reference of less than 250 pcm. The APOLLO3 model used by Framatome is more refined than the CEA model: the reactivity differences are very low for the Framatome case. It appears that the calculation method employed by PSI for the CASMO5 calculations is less precise than those used by ASNR and KIT, particularly when control rods are included in the simulation.

The results from the APOLLO2, nTracer and WIMS10 codes differ more from the reference, with reactivity differences of up to -400 to -500 pcm. One thing to mention is that the nTracer code was used with ENDF/B7.0 NDL and not B7.1, which is a deviation from the specification, and can be a cause to the reactivity differences observed.

The HELIOS code shows the greatest deviation in these lattice calculations, at up to 1,500 pcm. In the case of SSTC NRS simulations, these deviations can be explained by the use of the ENDF/B6 NDL, which differs from the specifications. There is no explanation for the reason behind such a large deviation in the Tractebel results.

9.1.2.2. Control Rod Bank Worth

All participants calculated the effective neutron multiplication factor k_{eff} of several core configurations with different insertion of control rod banks (CRB). These k_{eff} values are converted into reactivity values (ρ, in pcm) thanks to the following formula:

$$\rho = \frac{k_{eff} - 1}{k_{eff}} \times 1.0E^5$$

These core reactivities are reported in Table 17 for ENDF/B7.1 NDL, and Table 18 for JEFF-3.1.1 NDL.

Co-funded by the European Union
UK Research and Innovation
The Research Council of Norway
Project funded by

Table 17. ENDF/B7.1. Reactivity (in pcm) of core configurations.

Configuration	CEA-TRIPOLI4	ASNR-TRIPOLI5	CEA-AP3/Diff2g	ASNR-CMS5	KIT-CMS5	Tractebel-Panther5	PSI-CMS5	SSTC NRS-DYN3D	ASNR-CASMO/PARCS	CEA-AP3/SN8g	PSI-nTracer	UJV-DYN3D
All Rods Out (ARO)	21	6	-37	85	0	-448	219	-288	-4	102	-126	-248
G1 in	22	8	-71	132	40	-505	271	-423	-12	120	-138	-222
G2 in	20	10	-54	113	23	-409	241	-358	38	111	-119	-169
G3 in	23	10	-47	93	13	-395	238	-361	-83	137	-159	-352
G4 in	23	8	-22	110	12	-313	232	-293	140	138	-105	-25
G1+G2+G3+G4 in	33	3	-41	244	114	-303	414	-428	384	167	-146	396
S in	33	14	2	154	72	-778	385	-738	-157	277	-221	-387
All Rods In (ARI)	62	13	241	258	125	174	722	-85	1167	430	-291	1802

Table 18. JEFF-3.1.1. Reactivity (in pcm) of core configurations.

Configuration	CEA-TRIPOLI4	EDF-TRIPOLI4	CEA-AP3/Diff2g	ASNR-CMS5	FRAMATOME-AP3/SPn8g	ASNR-CASMO/PARCS	CEA-CRONOS2	CEA-AP3/SN8g	PSI-SERPENT
All Rods Out (ARO)	73	70	-19	90	593	4	-139	124	0
G1 in	76	78	-52	138	683	-3	-153	142	3
G2 in	74	72	-35	121	641	50	-144	133	2
G3 in	73	73	-31	91	679	-84	-167	156	-4
G4 in	80	77	-4	121	724	153	-119	160	6
G1+G2+G3+G4 in	95	95	-24	254	1085	397	-102	187	5
S in	94	94	21	146	1100	-172	-177	297	-1
All Rods In (ARI)	149	148	267	251	2345	1164	-6	452	2

From these values, the control rod banks worth (CRBW) were evaluated by comparing the k_{eff} of the configuration c with inserted control rods, and the k_{eff} of the ARO configuration, as expressed in the following formula:

$$CRBW = \frac{k_{eff}^{c} - k_{eff}^{ARO}}{k_{eff}^{c} \times k_{eff}^{ARO}} \times 1.0E^{+5} = \rho^{c} - \rho^{ARO}$$

The absolute (in pcm) and relative (in %) deviations of CRBW evaluated by the participant p with respect to the reference ref (corresponding to KIT-SERPENT2 results) are given by the following equations:

$$\Delta CRBW(in\ pcm) = CRBW^{p} - CRBW^{ref}$$

$$\Delta CRBW(in\ \%) = \frac{CRBW^{p} - CRBW^{ref}}{CRBW^{ref}} \times 100$$

The operating conditions used for these core calculations are described in Table 2. These control rod banks worth are presented in Figure 17 for the ENDF/B7.1 NDL, and Figure 18 for the JEFF-3.1.1 NDL.

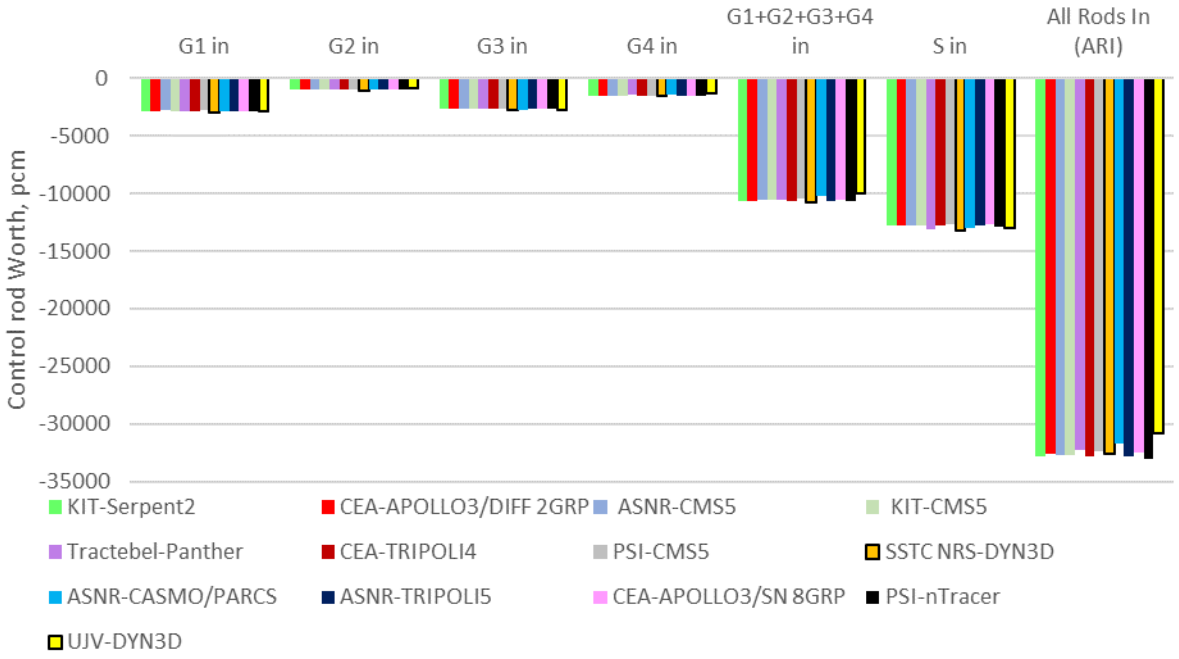

Figure 17. ENDF/B7.1. Control rod bank worth, in pcm.

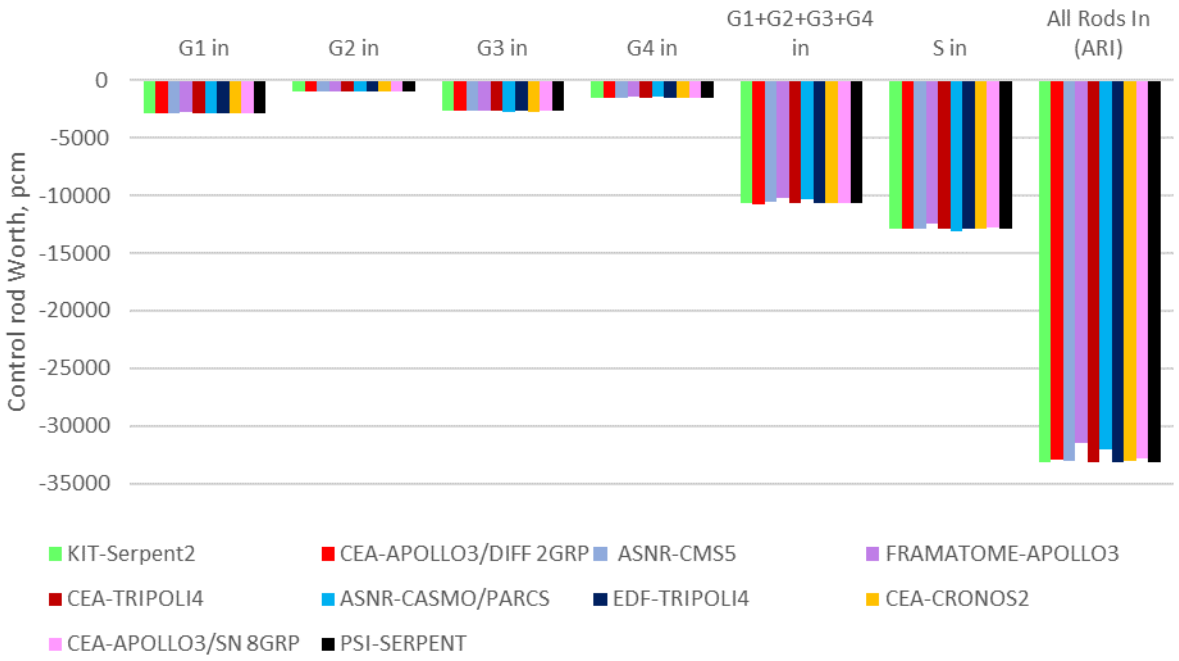

Figure 18. JEFF-3.1.1. Control rod bank worth, in pcm.

The absolute deviations ΔCRBW (in pcm) between each CRBW and the reference one, obtained with KIT-SERPENT2 calculations, are given in Table 19 for ENDF/B7.1 results, and Table 20 for JEFF-3.1.1. The relative deviations in % are given in Table 21 and are plotted in Figure 19 for ENDF/B7.1, and Table 22 and Figure 20 for JEFF-3.1.1.

Table 19. ENDFB/7.1. Absolute deviations of CRBW with the reference, in pcm.

Configuration	CEA-TRIPOLI4	ASNR-TRIPOLI5	CEA-APOLLO3/Diff2g	ASNR-CMS5	KIT-CMS5	Tractebel-Panther5	PSI-CMS5	SSTC NRS-DYN3D	ASNR-CASMO/PARCS	CEA-AP3/SN8g	PSI-nTracer	UJV-DYN3D
All Rods Out (ARO)	-	-	-	-	-	-	-	-	-	-	-	-
G1 in	1	2	-34	47	40	-57	53	-135	-8	18	-12	26
G2 in	-2	4	-17	28	23	40	22	-70	42	8	8	79
G3 in	2	4	-10	8	13	54	19	-73	-79	35	-33	-105
G4 in	2	2	15	25	11	135	14	-5	144	36	21	223
G1+G2+G3+G4 in	12	-3	-5	158	114	145	196	-141	388	65	-19	644
S in	11	8	39	68	71	-329	166	-450	-153	175	-94	-139
All Rods In (ARI)	40	7	278	173	125	622	503	202	1172	327	-164	2050

Table 20. JEFF-3.1.1. Absolute deviations of CRBW with the reference, in pcm.

Configuration	CEA-TRIPOLI4	EDF-TRIPOLI4	CEA-AP3/Diff2g	ASNR-CMS5	FRAMATOME-AP3/SPn8g	ASNR-CASMO/PARCS	CEA-CRONOS2	CEA-AP3/SN8g	PSI-SERPENT
All Rods Out (ARO)	-	-	-	-	-	-	-	-	-
G1 in	3	8	-33	48	90	-7	-14	19	3
G2 in	1	3	-16	32	48	46	-5	10	2
G3 in	0	4	-12	2	86	-88	-27	33	-4
G4 in	7	7	15	31	130	148	20	37	6
G1+G2+G3+G4 in	22	25	-5	164	491	393	37	64	5
S in	21	25	40	57	507	-176	-38	174	-1
All Rods In (ARI)	76	79	286	162	1751	1160	133	328	2

Table 21. ENDF/B7.1. Relative deviations of CRBW with the reference.

Configuration	CEA-TRIPOLI4	ASNR-TRIPOLI5	CEA-APOLLO3	ASNR-CMS5	KIT-CMS5	Tractebel-Panther5	PSI-CMS5	SSTC NRS-DYN3D	ASNR-CASMO/PARCS	CEA-AP3/SN8g	PSI-nTracer	UJV-DYN3D
All Rods Out (ARO)	-	-	-	-	-	-	-	-	-	-	-	-
G1 in	0,0%	-0,1%	1,2%	-1,6%	-1,4%	2,0%	-1,8%	4,7%	0,3%	-0,6%	0,4%	-0,9%
G2 in	0,2%	-0,4%	1,8%	-2,9%	-2,3%	-4,1%	-2,3%	7,2%	-4,3%	-0,8%	-0,8%	-8,1%
G3 in	-0,1%	-0,1%	0,4%	-0,3%	-0,5%	-2,0%	-0,7%	2,7%	3,0%	-1,3%	1,2%	3,9%
G4 in	-0,1%	-0,1%	-0,9%	-1,6%	-0,7%	-8,7%	-0,9%	0,3%	-9,3%	-2,3%	-1,4%	-14,4%
G1+G2+G3+G4 in	-0,1%	0,0%	0,0%	-1,5%	-1,1%	-1,4%	-1,8%	1,3%	-3,6%	-0,6%	0,2%	-6,0%
S in	-0,1%	-0,1%	-0,3%	-0,5%	-0,6%	2,6%	-1,3%	3,5%	1,2%	-1,4%	0,7%	1,1%
All Rods In (ARI)	-0,1%	0,0%	-0,8%	-0,5%	-0,4%	-1,9%	-1,5%	-0,6%	-3,6%	-1,0%	0,5%	-6,2%

Table 22. JEFF-3.1.1. Relative deviations of CRBW with the reference.

Configuration	CEA-TRIPOLI4	EDF-TRIPOLI4	CEA-AP3/Diff 2g	ASNR-CMS5	FRAMATOME-AP3/SPn 8g	ASNR-CASMO/PARCS	CEA-CRONOS2	CEA-AP3/SN8g	PSI-SERPENT
All Rods Out (ARO)	-	-	-	-	-	-	-	-	-
G1 in	-0,1%	-0,3%	1,1%	-1,7%	-3,1%	0,3%	0,5%	-0,6%	-0,1%
G2 in	-0,1%	-0,3%	1,6%	-3,2%	-4,9%	-4,6%	0,5%	-1,0%	-0,2%
G3 in	0,0%	-0,1%	0,4%	-0,1%	-3,2%	3,3%	1,0%	-1,2%	0,1%
G4 in	-0,4%	-0,5%	-1,0%	-2,0%	-8,5%	-9,6%	-1,3%	-2,4%	-0,4%
G1+G2+G3+G4 in	-0,2%	-0,2%	0,0%	-1,5%	-4,6%	-3,7%	-0,3%	-0,6%	0,0%
S in	-0,2%	-0,2%	-0,3%	-0,4%	-3,9%	1,4%	0,3%	-1,3%	0,0%
All Rods In (ARI)	-0,2%	-0,2%	-0,9%	-0,5%	-5,3%	-3,5%	-0,4%	-1,0%	0,0%

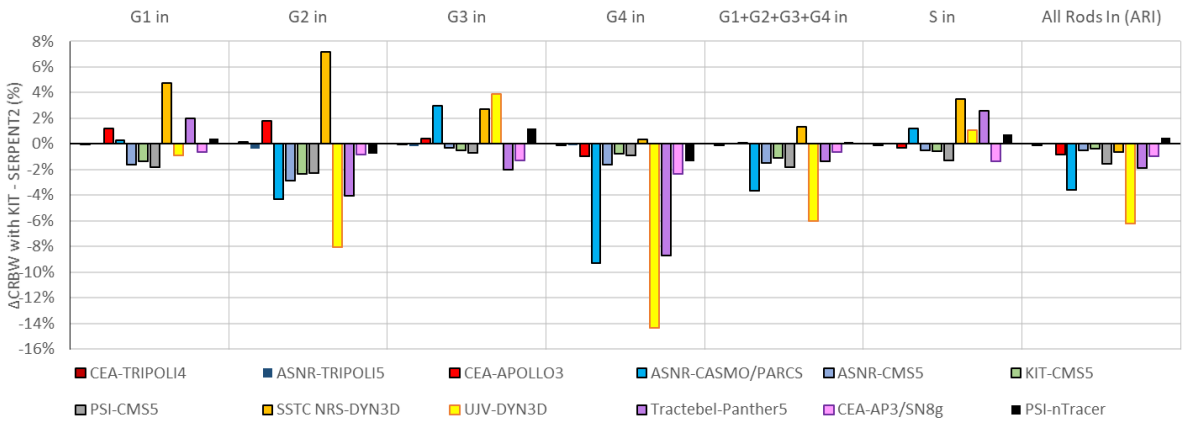

Figure 19. ENDF/B7.1. Relative deviations of CRBW with the reference.

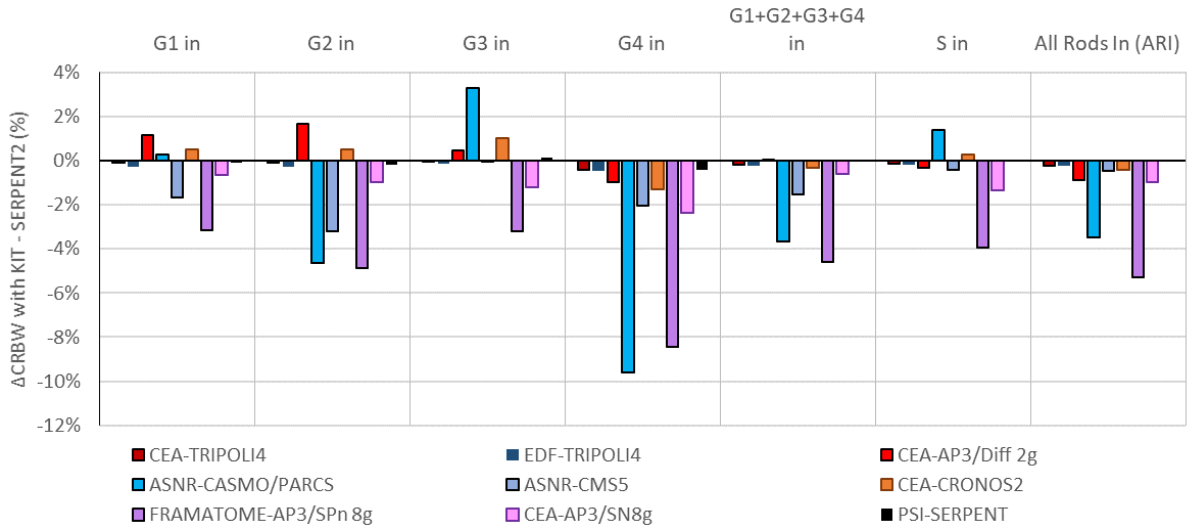

Figure 20. JEFF-3.1.1. Relative deviations of CRBW with the reference.

Concerning the core reactivities (Tables 17 and 18):

Monte Carlo methods (PSI-SERPENT2, ASNR-TRIPOLI5) fit exactly with the reference results produced by KIT-SERPENT2, with less than 15 pcm of difference. TRIPOLI4® results deviate a little more (20 to 30 pcm with ENDF/B7.1; 70 to 95 pcm with JEFF-3.1.1), except for the ARI configuration, where the deviation reaches 62 pcm with ENDF/B7.1 and 149 pcm with JEFF-3.1.1.

The advanced methods (CEA-APOLLO3/SN 8g, FRAMATOME-APOLLO3/SPn 8g, PSI-nTracer/8g) show large deviations from the reference: APOLLO3/SN between 100 and 450 pcm; APOLLO3/SPn between 600 and 2,350 pcm; nTracer between 100 and 300 pcm.

Codes involving industry-like methods, such as APOLLO3/Diffusion 2G, CMS5 and CRONOS2, demonstrate relatively good performance in terms of reactivity accuracy compared to advanced methods, with reactivity deviations ranging from 0 to 250 pcm. The CMS5 code used by PSI shows larger deviations (200–700 pcm) than the CMS5 code used by ASNR or KIT. Reasons for it need to be investigated. The PARCS code, when fed with CASMO5 homogeneous cross sections, shows good agreement with the reference results for configurations involving 0 to 1 bank insertion (with deviations of 3 to 150 pcm), but differences increase for configurations involving more bank insertions (with deviations of 160 to 1,170 pcm). The PANTHER5 and DYN3D codes generally show the largest deviations, in the order of 200 to 500 pcm.

Concerning the CRBW (Tables 19 to 22, Figures 17 to 20):

PSI-SERPENT2 and ASNR-TRIPOLI5 results fit exactly (less than 8 pcm of deviation) with the reference results provided by KIT-SERPENT2. The results obtained with TRIPOLI4® by CEA and EDF are very close to the reference, even for configurations involving the insertion of a large number of control rods into the core, which produce slightly less favourable results. In particular, the “ARI” configuration shows a deviation of up to 80 pcm.

The APOLLO2/CRONOS2, APOLLO3/Diffusion 2g, APOLLO3/Sn 8g, CASMO5/SIMULATE5 and nTracer codes exhibit the same behaviour: when only one control rod bank is inserted into the core, its efficiency is calculated with great accuracy, with less than 50 pcm deviation. However, configurations involving many banks inserted provide less accurate results, with up to 300 pcm deviation. This behaviour is exacerbated in the calculations made by PSI with the CMS5 code system, where the “ARI” configuration deviates by 500 pcm.

The APOLLO3/SPn 8g, DYN3D, PANTHER5 and PARCS codes show the largest deviations. When only one 'grey' control rod bank is inserted into the core, the deviation is up to 100 pcm; this increases to 200 pcm when the 'black-type' bank G4 is inserted; and when several banks or the S bank are inserted, the deviation from the reference increases to 2,000 pcm.

The PSI-nTracer MoC and SSTC NRS-DYN3D results obtained with ENDF/B7.0 and ENDF/B6, respectively, do not deviate the most from the reference.

9.1.2.3. 2D Radial Power

The power produced in the active zone is calculated, with the values being integrated both assembly-wise and axially. Each participant has plotted 2D radial power maps, as can be seen in Figures 12 and 13. The same operating conditions as those detailed in Table 2 were used. All these power maps were compared to the corresponding reference one, obtained by KIT-SERPENT2, by the following equation:

$$\Delta P_{i,j} = \left(P_{i,j}^{p} - P_{i,j}^{ref}\right)$$

With $\Delta P_{i,j}$ the value of the absolute power deviation in the fuel assembly located with coordinates (i,j); $P_{i,j}^{p}$ is the value of the power calculated by participant p in the fuel assembly located with coordinates (i,j) and $P_{i,j}^{ref}$ the corresponding power value calculated with KIT-SERPENT2.

To avoid plotting all the 2D radial absolute power deviation maps, they were all converted in box-and-whisker plots. This plot type permits to represent a dispersion of values. It contains:

- a cross that is the mean value of the dispersion,
- a line that represents the median, also called the 50th percentile (half of the values are above and the other half are below this line),
- a box whose top and bottom edges represent the 25th percentile (25% of the values are located between the 25th and the 50th percentile), and the 75th percentile (25% of the values are located between the 75th and the 50th percentile). The interval between 25th and 75th percentile is called the interquartile range (IQR),
- upper and lower whiskers. They represent the maximal and minimal values, or 1.5 times IQR at maximum,
- it may be some dots, representing the outliers. Outliers are values exceeding 1.5 times IQR.

A schematic view of his type of plot is represented in Figure 21.

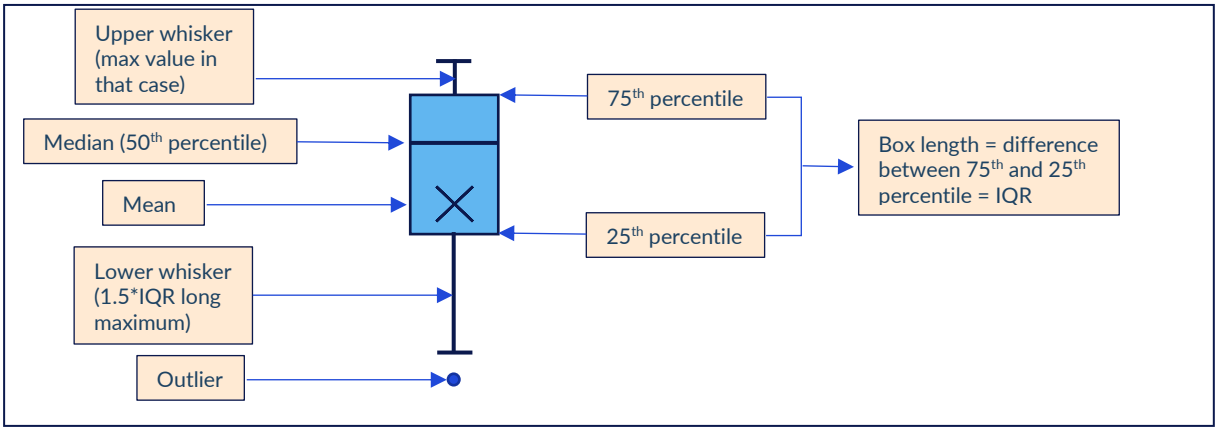

Figure 21. Box-and-whiskers plot definition.

Absolute 2D power deviations have been calculated for the following configurations:

- “ARO”. ENDF/B7.1 (left) and JEFF-3.1.1 (right) values are plotted in Figure 22,
- “G1 in”. ENDF/B7.1 (left) and JEFF-3.1.1 (right) values are plotted in Figure 23,
- “G2 in”. ENDF/B7.1 (left) and JEFF-3.1.1 (right) values are plotted in Figure 24,
- “G3 in”. ENDF/B7.1 (left) and JEFF-3.1.1 (right) values are plotted in Figure 25,
- “G4 in”. ENDF/B7.1 (left) and JEFF-3.1.1 (right) values are plotted in Figure 26,
- “S in”. ENDF/B7.1 (left) and JEFF-3.1.1 (right) values are plotted in Figure 27,
- “ARO”. ENDF/B7.1 (left) and JEFF-3.1.1 (right) values are plotted in Figure 28.

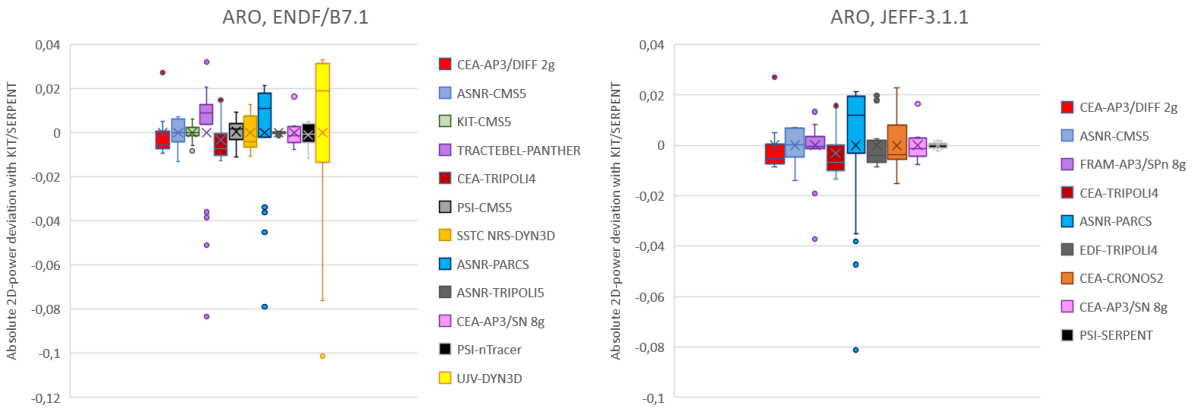

Figure 22. Absolute 2D power deviations for "ARO" configuration.

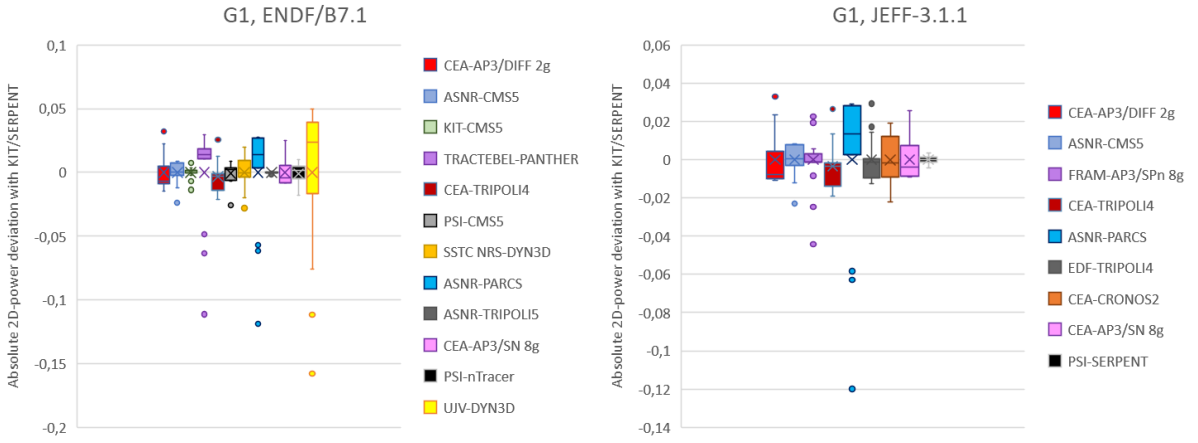

Figure 23. Absolute 2D power deviations for "G1 in" configuration.

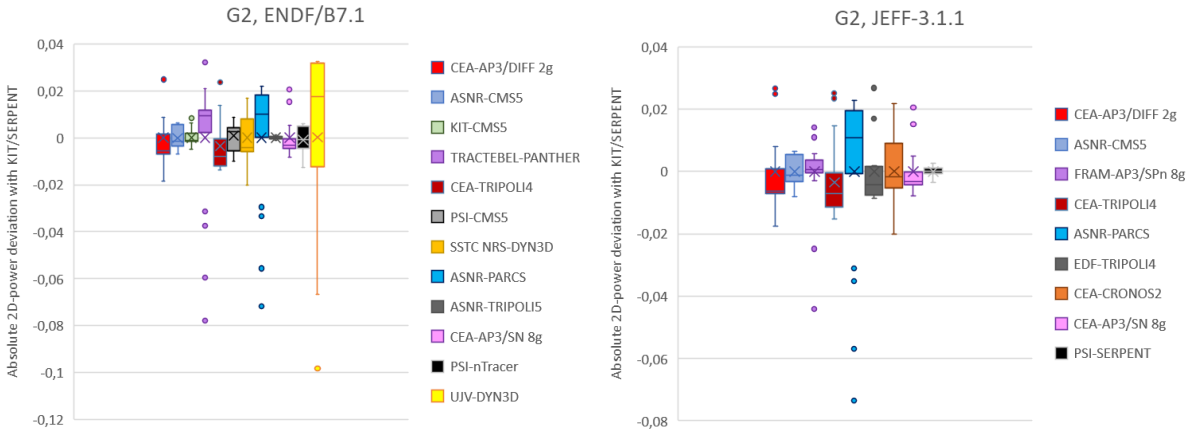

Figure 24. Absolute 2D power deviations for "G2 in" configuration.

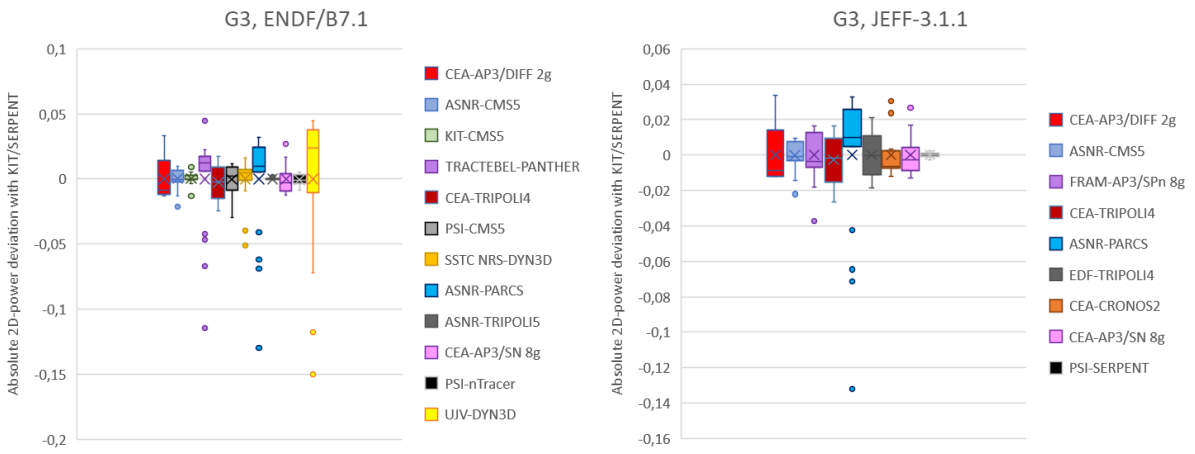

Figure 25. Absolute 2D power deviations for "G3 in" configuration.

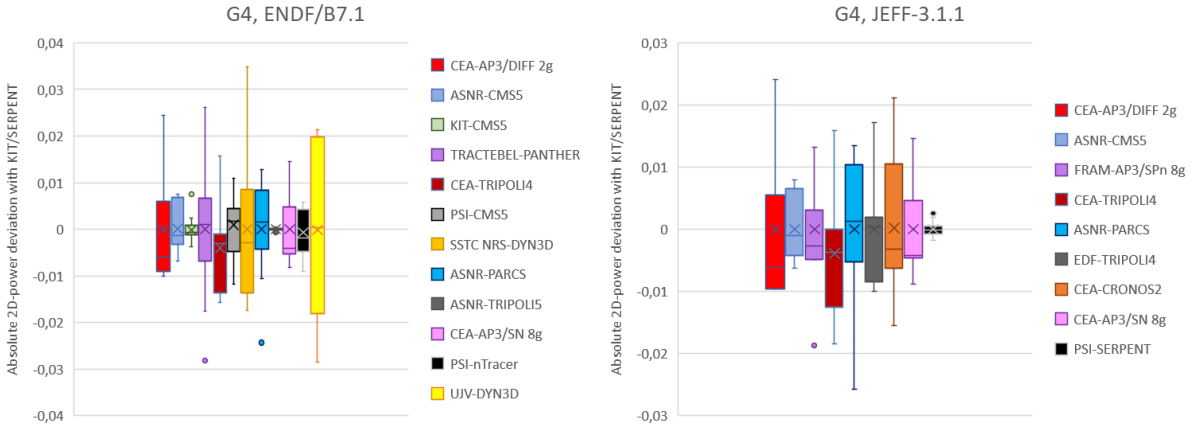

Figure 26. Absolute 2D power deviations for "G4 in" configuration.

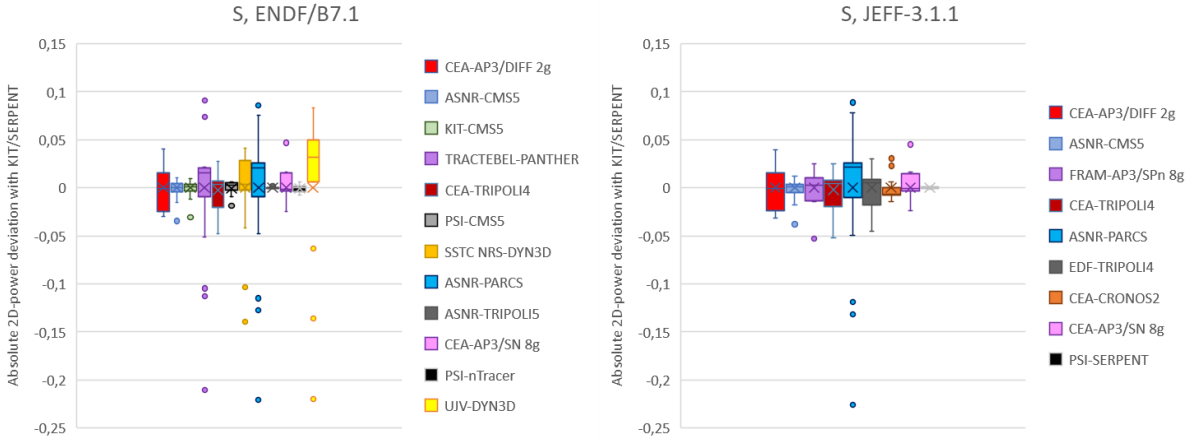

Figure 27. Absolute 2D power deviations for "S in" configuration.

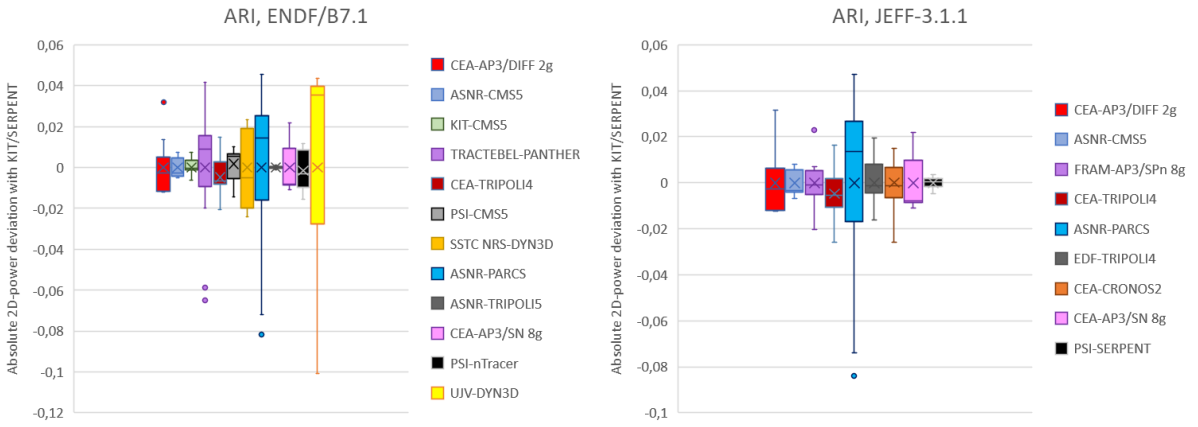

Figure 28. Absolute 2D power deviations for "ARI" configuration.

Once more, PSI-SERPENT2 and ASNR-TRIPOLI5 results fit exactly with KIT-SERPENT2 results, which demonstrate the really good accordance in the input data, and in the models chosen. Although their results are not shown here, HZDR and ASNR contributed to the verification and review of the SERPENT2 calculations, thereby confirming the robustness of the reference results obtained by KIT-SERPENT2 simulations. The core exhibits $\pi/4$ symmetry, which was utilised when processing the ASNR-TRIPOLI5 and KIT-SERPENT results. The PSI-SERPENT2 results are the code's raw output and show discrepancies of up to 0.5% with the previous two sets of results in the case of the ARI configuration. This small discrepancy is due to the convergence of the fission sources, demonstrating the very high quality of the results obtained.

The other Monte Carlo results obtained using the TRIPOLI4® code by CEA and EDF show a greater deviation from the reference. This deviation, which can reach $\Delta P_{i,j} = 0.052$ in the ARI configuration and only affects one type of fuel assembly per configuration; typically, FAs with the greatest number of gadolinium pins are affected. It appears to originate from the tally (or score) type required in the codes: SERPENT2 users defined an '*-8*' macroscopic reaction, accounting for total fission energy production, whereas TRIPOLI4® users defined total energy production, accounting for energy produced by both fission and neutron capture. This difference in how the code defines the output result may account for some of the discrepancies observed with deterministic codes, which typically employ a multi-source energy deposit (fission and capture). This bias stems from the fact that the benchmark specifications were not clearly defined. Ideally, at this stage of the benchmark, fission rates would have been compared. This would ensure that all the codes produce the same type of results.

Advanced deterministic models such as CEA-APOLLO3/Sn 8g, FRAMATOME-APOLLO3/SPn 8g, and PSI-nTracer MoC/8g produce good results regarding 2D power distributions. Results based on APOLLO3 transport or simplified transport show deviations of less than 0.053, which correspond to the behaviour of TRIPOLI4® results. One possible explanation for these deviations is similar to that for the differences between TRIPOLI4® and SERPENT2: APOLLO3® calculates power values that account for fission and neutron capture energies, whereas SERPENT2 only accounts for fission energy deposition. Despite deviating from the specifications concerning the NDL, the PSI-nTracer results show very good agreement with the reference results, with an absolute deviation of less than 0.018.

For industry-like deterministic codes, such as APOLLO3/Diffusion 2g and CRONOS2, the absolute deviations with the reference are limited to 0.040, with the same behaviour as TRIPOLI4®, which indicates that the main source of the deviations may be the energy deposition definition.

For CMS5 results, deviations are limited to 0.038 but this value only concerns the central FA of the configuration "S". The 2nd largest deviation value is 0.026 which emphasize the very good quality of the 2D power results produced with this code.
UJV-DYN3D, TRACTEBEL-PANTHER and ASNR-PARCS results show the same behaviour: the power tends to be underestimated at the centre of the core (until -0.23) and overestimated at the periphery (up to +0.09). This may be due to a calculation scheme for the radial reflector not adapted to heavy reflector, that overestimate the power produced at the periphery of the core. The tendency for SSTC NRS-DYN3D is quite the same, but very attenuated. The reason of this attenuation may be caused by the NDL used (ENDF/B6) which deviates from the benchmark specifications.

9.1.2.4. 1D Axial Power

The power produced in the active zone is calculated, with the values being integrated core-wise radially. This allows an axial 1D power profile to be evaluated, with 20 values taken at different heights along the core. The same operating conditions as those detailed in Table 2 were used. All these 1D power profiles were compared to the corresponding reference one, obtained by KIT-SERPENT2, by the following equation:

$$\Delta P_z = \left(P_z^p - P_z^{ref}\right) \times 100$$

With ΔP_z the value of the absolute power deviation in the z axial zone; P_z^p is the value of the power calculated by participant p in the z axial zone and P_z^{ref} the corresponding power value calculated with KIT-SERPENT2. To enhance the presentation of the results, the differences in power have been multiplied by 100.

Absolute 1D power deviations have been calculated for the following configurations:

- "ARO". ENDF/B7.1 (left) and JEFF-3.1.1 (right) values are plotted in Figure 29,
- "G1 in". ENDF/B7.1 (left) and JEFF-3.1.1 (right) values are plotted in Figure 30,
- "G2 in". ENDF/B7.1 (left) and JEFF-3.1.1 (right) values are plotted in Figure 31,
- "G3 in". ENDF/B7.1 (left) and JEFF-3.1.1 (right) values are plotted in Figure 32,
- "G4 in". ENDF/B7.1 (left) and JEFF-3.1.1 (right) values are plotted in Figure 33,
- "S in". ENDF/B7.1 (left) and JEFF-3.1.1 (right) values are plotted in Figure 34,
- "ARO". ENDF/B7.1 (left) and JEFF-3.1.1 (right) values are plotted in Figure 35.

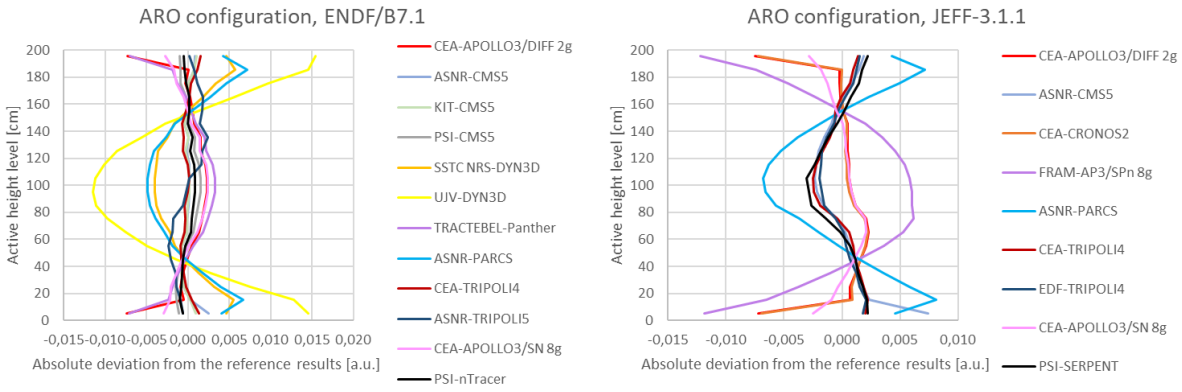

Figure 29. Absolute 1D power profile deviations for "ARO" configuration.

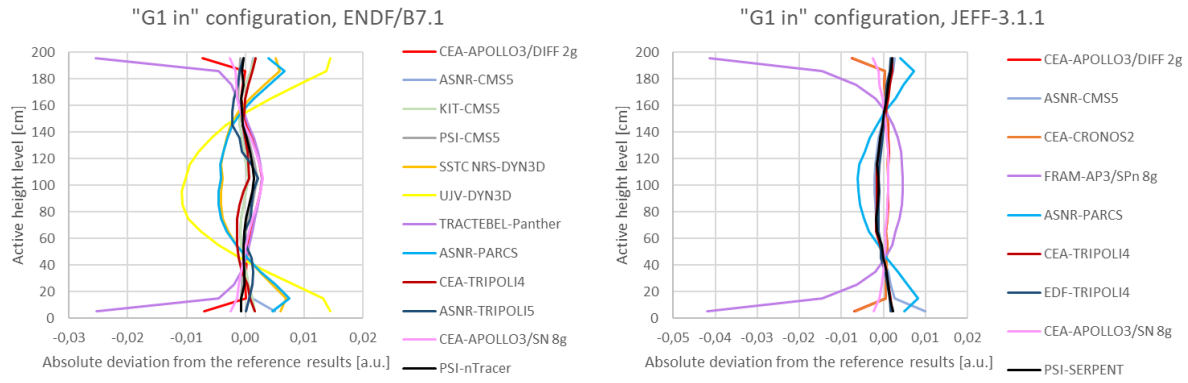

Figure 30. Absolute 1D power profile deviations for "G1 in" configuration.

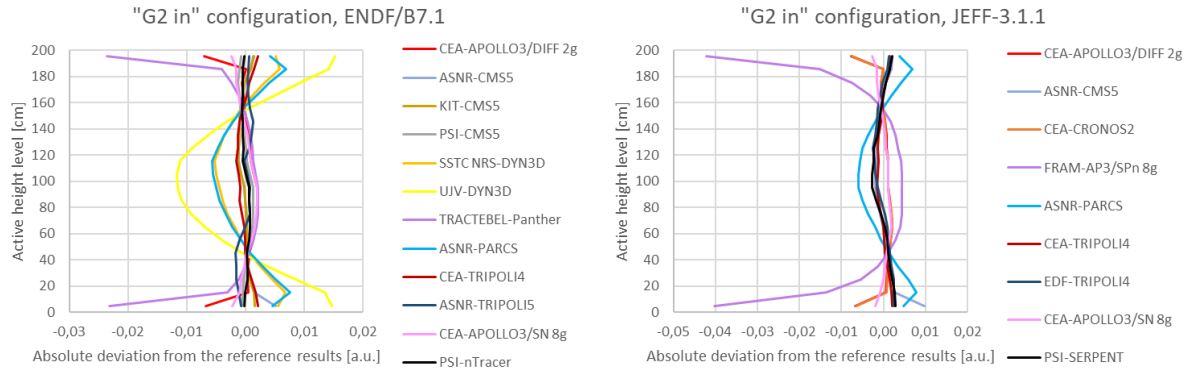

Figure 31. Absolute 1D power profile deviations for "G2 in" configuration.

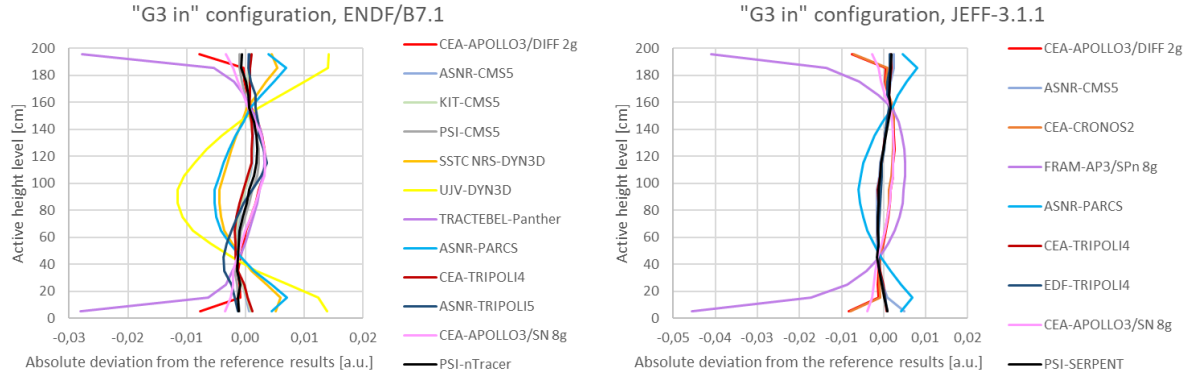

Figure 32. Absolute 1D power profile deviations for "G3 in" configuration.

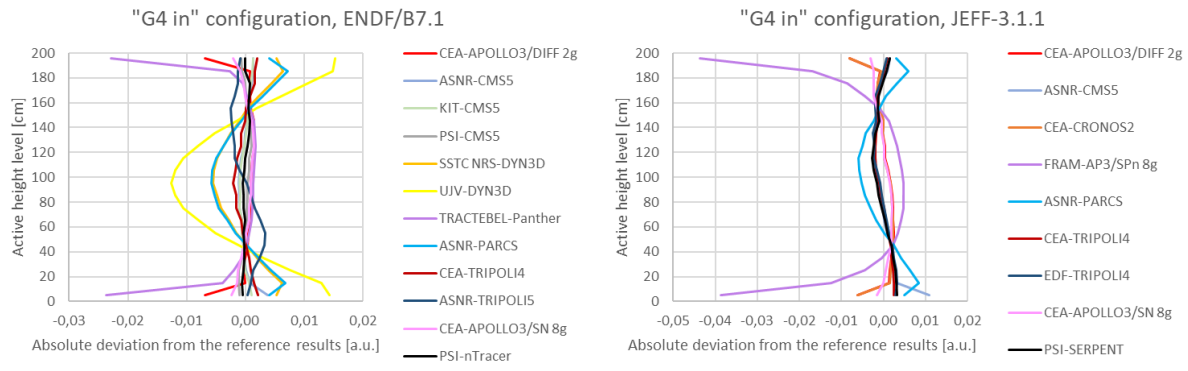

Figure 33. Absolute 1D power profile deviations for "G4 in" configuration.

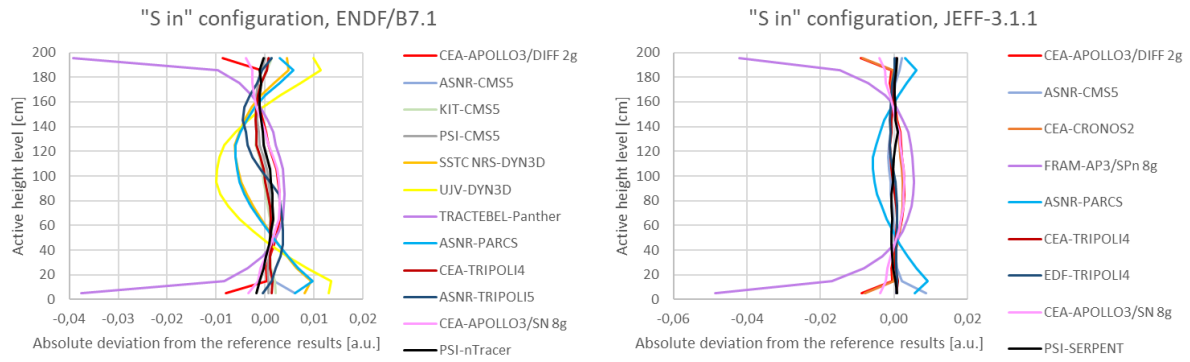

Figure 34. Absolute 1D power profile deviations for "S in" configuration.

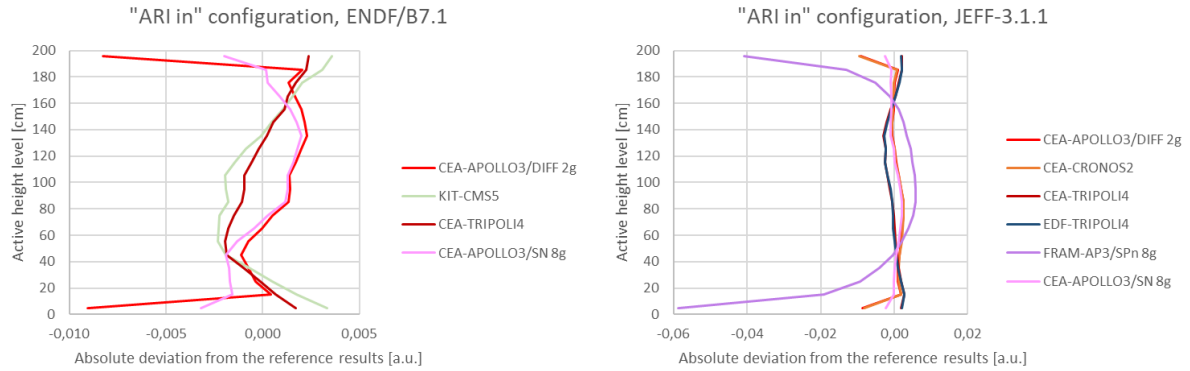

Figure 35. Absolute 1D power profile deviations for "ARI" configuration.

The 1D-axial power profiles are very well evaluated, with an absolute deviation comprised between -0.01 and +0.01 in most of the codes. Some exceptions can be noted:

- Advanced method using APOLLO3/SPn reveal larger discrepancies (up to 0.06) in the bottom two and top two calculation cells of the model. The same behaviour is observed with PANTHER code (up to 0.04) when control rods are inserted into the core.
- Industry-like methods implemented in DYN3D and PARCS generate axial deviations of up to -0.013 at the core mid-plane, and up to +0.015 at the top and bottom edges.

This may be due to the calculation methods employed for axial reflectors not being adapted to accurately reproduce the reflector's behaviour within the first few centimetres of the active zone.

9.1.2.5. Thermal Feedback Coefficients

The k_{eff} values of 6 configurations described in Section 7.1.4 are calculated with core simulations. The thermal feedback coefficients are estimated using the following formula:

$$\theta = \frac{\Delta\rho}{\Delta T} = \frac{\rho^{T_i} - \rho^{T_{ref}}}{T_i - T_{ref}}$$

With

- θ the thermal feedback coefficient in pcm/K or pcm/°C depending on the unit of the temperature variation,
- $\rho = \frac{k_{eff}-1}{k_{eff}} \times 1.0E^{+5}$ the reactivity in pcm,
- ρ^{T_i} and $\rho^{T_{ref}}$ the reactivity values at temperatures T_i and T_{ref},
- T_i and T_{ref} the temperature of the configuration i, and the temperature of the reference configuration, respectively.

Fuel and coolant thermal coefficients are calculated with ENDF/B7.1 and JEFF-3.1.1 NDLs, their values are reported in the Tables 23 and 24, and the relative deviations of these coefficients compared to the reference ones obtained with KIT/SERPENT2 are given in the Tables 25 and 26.

Table 23. ENDF/B7.1. Fuel and coolant thermal coefficients.

	KIT/Serpent	CEA/AP3-DIFF2g	ASNR 4GRP - CMS5	KIT/CMS5	TRACTEBEL - Panther	CEA-TRIPOLI4	PSI-CMS5	SSTC NRS - DYN3D	ASNR-CASMO/PARCS	ASNR-TRIPOLI5	CEA-AP3/SN 8g	PSI-nTracer	UJV-DYN3D
Fuel Temp. Coef., ARO (pcm/K)	-2,35	-2,47	-2,54	-2,39	-2,40	-2,31	-2,49	-2,53	-2,48	-2,31	-2,49	-2,44	-2,54
Coolant Temp. Coef., ARO (pcm/°C)	-48,1	-52,8	-47,2	-47,7	-46,2	-48,2	-47,8	-54,7	-53,6	-48,3	-53,3	-47,7	-51,5
Fuel Temp. Coef., ARI (pcm/K)	-3,26	-3,43	-3,54	-3,34	-3,29	-3,22	-3,40	-3,49	-1,71	-3,30	-3,44	-3,35	-3,47
Coolant Temp. Coef., ARI (pcm/°C)	-103,9	-115,5	-100,7	-101,9	-97,6	-103,8	-102,2	-122,2	-116,7	-104,6	-115,8	-102,3	-104,7

Table 24. JEFF-3.1.1. Fuel and coolant thermal coefficients.

	KIT/Serpent	CEA/AP3-DIFF2g	ASNR 4GRP - CMS5	FRAMATOME - APOLLO3	CEA-TRIPOLI4	ASNR-CASMO/PARCS	EDF-TRIPOLI4	CEA-CRONOS2	CEA-AP3/SN 8g	PSI-SERPENT
Fuel Temp. Coef., ARO (pcm/K)	-2,35	-2,48	-2,54	-2,47	-2,35	-2,49	-2,34	-2,49	-2,49	-2,36
Coolant Temp. Coef., ARO (pcm/°C)	-48,5	-52,8	-47,8	-47,5	-48,3	-54,2	-48,3	-48,6	-53,4	-48,4
Fuel Temp. Coef., ARI (pcm/K)	-3,28	-3,44	-3,57	-3,39	-3,27	-1,72	-3,28	-3,45	-3,45	-3,28
Coolant Temp. Coef., ARI (pcm/°C)	-105,7	-116,9	-103,2	-101,1	-104,8	-119,1	-105,4	-105,9	-117,2	-105,2

Table 25. ENDF/B7.1. Relative deviations of fuel and coolant thermal coefficients.

	CEA/AP3-DIFF2g	ASNR 4GRP - CMS5	KIT/CMS5	TRACTEBEL - Panther	CEA-TRIPOLI4	PSI-CMS5	SSTC NRS - DYN3D	ASNR-CASMO/PARCS	ASNR-TRIPOLI5	CEA-AP3/SN 8g	PSI-nTracer	UJV-DYN3D
Fuel Temp. Coef., ARO (pcm/K)	5,1 %	7,8 %	1,8 %	2,0 %	-1,8 %	5,8 %	7,5 %	5,6 %	-1,6 %	5,8 %	3,8 %	8,1 %
Coolant Temp. Coef., ARO (pcm/°C)	9,7 %	-1,9 %	-0,7 %	-3,9 %	0,2 %	-0,6 %	13,8 %	11,5 %	0,5 %	10,8 %	-0,8 %	7,0 %
Fuel Temp. Coef., ARI (pcm/K)	5,1 %	8,7 %	2,4 %	1,0 %	-1,3 %	4,2 %	7,2 %	-47,7 %	1,3 %	5,5 %	2,9 %	6,4 %
Coolant Temp. Coef., ARI (pcm/°C)	11,1 %	-3,1 %	-1,9 %	-6,0 %	-0,1 %	-1,7 %	17,6 %	12,3 %	0,7 %	11,4 %	-1,5 %	0,8 %

Table 26. JEFF-3.1.1. Relative deviations of fuel and coolant thermal coefficients.

	CEA/AP3-DIFF2g	ASNR 4GRP - CMS5	FRAMATOME - APOLLO3	CEA-TRIPOLI4	ASNR-CASMO/PARCS	EDF-TRIPOLI4	CEA-CRONOS2	CEA-AP3/SN 8g	PSI-SERPENT
Fuel Temp. Coef., ARO (pcm/K)	5,3 %	8,0 %	5,0 %	-0,1 %	5,9 %	-0,3 %	5,8 %	6,0 %	0,4 %
Coolant Temp. Coef., ARO (pcm/°C)	8,9 %	-1,5 %	-2,0 %	-0,4 %	11,8 %	-0,3 %	0,2 %	10,1 %	-0,2 %
Fuel Temp. Coef., ARI (pcm/K)	4,7 %	8,7 %	3,3 %	-0,3 %	-47,6 %	0,1 %	5,1 %	5,2 %	0,0 %
Coolant Temp. Coef., ARI (pcm/°C)	10,6 %	-2,4 %	-4,4 %	-0,8 %	12,7 %	-0,3 %	0,2 %	10,9 %	-0,5 %

Codes based on the Monte Carlo method, such as SERPENT2, TRIPOLI4® and TRIPOLI5, provide thermal feedback coefficient estimates that differ by less than 1.6% from the KIT-SERPENT2 reference.

Deterministic codes, on the other hand, estimate thermal feedback coefficients with biases ranging from -47.7% to +17.6%, indicating that the deterministic approach to this calculation differs fundamentally from Monte Carlo one. However, certain trends appear to emerge:

- All deterministic codes overestimate the fuel temperature coefficient (FTC), ranging from +1.8% (KIT-CMS5) to +8.7% (ASNR-CMS5). Most codes overestimate this coefficient by around +5% - +6%. Interestingly, the minimum and maximum values were obtained using the same calculation code. This clearly demonstrates that the calculation strategy must be precisely defined to minimise discrepancies of this type.
- Concerning the coolant temperature coefficient (CTC), the deterministic codes fall into two categories. The first category comprises CEA-APOLLO3, DYN3D and PARCS, and the CTC is generally overestimated by around +10 - +11%. The second category comprises FRAMATOME-APOLLO3, CMS5, CRONOS2, nTRACER and PANTHER, and the CTC is generally underestimated by around -2% (values spread between -6.0% and +0.2%). One possible explanation for this dual behaviour is the coolant temperature or density of the reflectors: if one family of simulations forgot to change the water density in the reflectors' zones, this could affect the core reactivity and the CTC evaluation. Once again, the importance of very detailed simulation specifications is evident.

An exception to the overestimation of the fuel temperature coefficient in ASNR-PARCS calculations is seen at the ARI configuration, where the value is underestimated by -48% compared to the reference. This is probably due to the significant discrepancy in this code's evaluation of k_{eff} for this configuration.

9.1.2.6. Kinetic Parameters

Some participants have calculated the kinetic parameters of the core in ARO and ARI configurations. In particular, the reactivity ρ of both configurations, the effective fraction of delayed neutrons β_{eff} and the average neutron generation time Λ_{eff} of the reference calculations with KIT/SERPENT2 have been reported to Tables 27 and 28 for ENDF/B7.1 and JEFF-3.1.1 NDLs, respectively. The relative deviations of these parameters with respect to the KIT/SERPENT2 values are also reported in these tables.

Table 27. ENDF/B7.1. Kinetic parameters.

Configuration	Parameter	KIT-Serpent	CEA-APOLLO3/DIFF2g	ASNR-CMS5/4g	KIT-CMS5	TRACTEBEL-Panther	CEA-TRIPOLI4	PSI-CMS5	SSTC NRS-DYN3D	ASNR-PARCS	ASNR-TRIPOLI5	CEA-AP3/SN 8g	PSI-nTracer	UJV-DYN3D
ARO	βeff [pcm]	702,6	1,8%	0,0%	0,1%	1,5%	-0,5%		7,4%				6,2%	2,6%
	Λeff [s]	2,43E-05	1,8%	-2,9%	0,8%	-3,8%	0,4%		2,4%				1,8%	7,1%
	ρ [pcm]	7636	-0,5%	1,1%	0,0%	-5,9%	0,3%	2,9%	-3,8%	-0,1%	0,1%	1,3%	-1,7%	-3,2%
ARI	βeff [pcm]	708,8	2,9%	-0,3%		3,5%	-0,5%		6,4%				-7,2%	1,9%
	Λeff [s]	2,27E-05	0,7%	-7,5%		-8,2%	0,3%		-23,4%				3,5%	-0,9%
	ρ [pcm]	-25200	-1,0%	-1,0%	-0,5%	-0,7%	-0,2%	-2,9%	0,3%	-4,6%	0,0%	-1,7%	1,2%	-7,2%

Table 28. JEFF-3.1.1. Kinetic parameters.

Configuration	Parameter	KIT-Serpent	CEA-APOLLO3/DIFF2g	ASNR-CMS5/4g	FRAM-AP3/SPn 8g	CEA-TRIPOLI4	ASNR-PARCS	EDF-TRIPOLI4	CEA-CRONOS2	CEA-AP3/SN 8g	PSI-SERPENT
ARO	βeff [pcm]	723,5	1,7%	-3,1%	0,1%	-0,5%		-0,6%	3,1%		-0,1%
	Λeff [s]	2,44E-05	1,7%	-3,0%	7,6%	0,3%		0,3%	1,6%		0,0%
	ρ [pcm]	7581	-0,2%	1,2%	7,8%	1,0%	0,1%	0,9%	-1,8%	1,6%	0,0%
ARI	βeff [pcm]	731,8	2,6%	-3,6%	0,5%	-0,6%		-0,6%	-10,2%		0,0%
	Λeff [s]	2,28E-05	1,7%	-7,7%	-23,4%	0,1%		0,1%	2,9%		0,0%
	ρ [pcm]	-25601	-1,0%	-1,0%	-9,2%	-0,6%	-4,5%	-0,6%	0,0%	-1,8%	0,0%

The Monte Carlo methods (SERPENT2 and TRIPOLI4®) produce results that are in very good agreement with the reference results, with a relative deviation of less than 1%.

APOLLO3/Diffusion 2g, CMS5 and CRONOS2 also provide good results, with a deviation of generally less than 3%. However, an exception is the β_{eff} estimated with CRONOS2 for the ARI configuration, where the relative deviation is 10%. Another exception is the evaluation of the Λ_{eff} by ASNR-CMS5 for the ARI configuration, which differs from the reference by 7.7%.

APOLLO3/SPn 8g, DYN3D, nTracer and PANTHER produce lower-quality results, with deviations from the reference of around 7% to 8%. For these codes, the Λ_{eff} of the ARI configuration can deviate by up to 23%.

9.1.3. Conclusions of HZP code benchmarking

The benchmarking phase realized at hot zero-power (HZP) state allowed the neutron calculations to be calibrated against the reference results. The calculations involved 2D fuel assembly patterns in an infinite lattice, as well as 3D core simulations with different control rod bank insertion configurations or fuel and coolant temperature settings. The codes calculated the following values:

- infinite (k_∞ , lattice calculations) or effective (k_{eff} , core calculations) neutron multiplication factors,
- 1D (axis along the height of the core) or 2D (radial plane) power distributions,
- neutron kinetic parameters.

The reference results were produced by KIT using the SERPENT2 Monte Carlo code. Independent SERPENT2 calculations by HZDR and ASNR led to the correction of several discrepancies and confirmed the robustness of the KIT simulations. Consequently, the KIT-SERPENT2 results are considered the reference solution.

Neutron calculations were carried out using the Monte Carlo method with the SERPENT2 (PSI), TRIPOLI4® (CEA and EDF) and TRIPOLI5 (ASNR) codes. The results produced by these codes agree very well with the reference results (typically by less than 0.5%). Nevertheless, it is important to specify exactly what calculations are to be performed, particularly with regard to the type of output required by the user. In our case, SERPENT2 and TRIPOLI5 calculated power values as fission energy deposits, whereas TRIPOLI4 defined power values as the total energy deposited in each grid cell, including energy from both fission and neutron capture. This difference in definition resulted in discrepancies of up to 0.05 in the power distributions per assembly.

These highly accurate results were compared with industrial-standard neutron simulations employing neutron diffusion theory with two or four energy groups. These simulations fall into two categories:

- Those that behave similarly to the reference, with limited reactivity calculation biases (less than a 250 pcm deviation for k_∞ and k_{eff}, with deviations limited to 300 pcm for CRBW, power differences per assembly of less than 0.04 in 2D and 0.01 in 1D, and 3% for neutron kinetic parameters). This category includes the APOLLO2/CRONOS2, APOLLO3® and CASMO5/SIMULATE5 codes (collectively known as CMS5).
- Those showing greater deviations from the reference (up to 1500 pcm on the k_∞, 1,200 pcm in core reactivity calculations, 2,000 pcm in CRBW, power differences of up to 0.23 in 2D and 0.015 in 1D, and around 7% in kinetic parameters). This category comprises the CASMO5/PARCS, HELIOS/DYN3D, and WIMS/PANTHER codes.

There is no obvious reason that would enable us to distinguish between these two categories of codes. Maybe the computational models used in the second category are not sophisticated enough to accurately reproduce the specific characteristics of soluble boron-free PWR cores. These characteristics include a radial reflector composed mainly of steel, extensive use of neutron poisons such as gadolinium, and core configurations with numerous control rods inserted.
Analyses of the differences between the calculation schemes have not been thorough enough to allow rigorous recommendations to be made. However, the following hypotheses may help to explain these discrepancies:

- It would appear that lattice calculations employing a two-level approach perform better than single-level calculations. The two-level approach involves a self-shielding calculation on an energy mesh comprising approximately 300 groups or more, and a second level based on the use of the MoC method to determine the spatial distribution of the neutron flux.
- The heterogeneities in fuel assemblies, particularly the presence of gadolinium-poisoned fuel rods or control rods, appear to necessitate the use of the P3 anisotropy approximation to correctly handle scattering phenomena.
- The presence of the above-described heterogeneities also appears to necessitate a finer radial spatial mesh for core calculations than the standard industry-wide meshes (where fuel assemblies are typically modelled using 2x2 homogeneous cells).

Further investigations are required to confirm these hypotheses.

Further simulations were carried out using advanced models, employing either the Sn transport theory (CEA-APOLLO3/Sn), the simplified SPn transport theory (FRAMATOME-APOLLO3/SPn), or the characteristic method (PSI-nTracer/MoC). Whilst the bias in core reactivity is rather disappointing for nTracer (100 to 300 pcm) and APOLLO3/Sn (150 to 450 pcm), it is downright poor in the case of APOLLO3/SPn (600 to 2,350 pcm). CRBWs are assessed fairly well by nTracer/MoC (bias below 160 pcm) and APOLLO3/Sn (bias below 330 pcm), but not by APOLLO3/SPn (maximum bias of 1,750 pcm). The 2D power profiles are calculated correctly by all three codes, but APOLLO3/SPn exhibits significant biases in the evaluation of the 1D profile, with deviations of up to 0.06 for this parameter. The neutron kinetic parameters exhibit biases of 6 to 8%. These results from advanced calculations are therefore generally disappointing, given the additional computing power required to perform them. They do show larger discrepancies than industry-like simulations, particularly in cases where strong absorbers are present. The presence of these absorbers, as well as the extensive use of neutron poisons and heavy radial reflectors, highlights the difficulty of modelling the soluble boron-free (SBF) core type.

9.2. HFP Code-to-Code Benchmarking

9.2.1. Serpent2/Subchanflow reference solution

For the second phase, four cases under HFP condition were defined to perform coupled neutronic and thermohydraulic simulations. These cases are divided in two groups: the first group (cases 1.1 and 1.2) does not consider xenon, while the second group (cases 2.1 and 2.2) includes equilibrium xenon concentration. For each group, two subcases were defined, considering either fixed control rod positions or a critical search condition.

Table 29 summarizes the effective multiplication factors obtained for each case. For the critical search calculations, the criteria for criticality ($\rho = 0$) were that the core reactivity remained within ± 20 pcm ($|\rho| < 20\ pcm$). Table 30 summarizes the resulting critical control rod bank positions.

Table 29. Serpent/SCF effective multiplication factors for the HFP cases studied. Number in parentheses indicate the ± 1-sigma statistical uncertainty in the last digit of the number.

Case	Xenon	Control rod banks	ENDF/B-VII.1 Keff	JEFF-3.1.1 Keff
1.1	Null	given	1.00266 (3)	1.00159 (3)
1.2	Null	critical search	1.00013 (3)	1.00014 (3)
2.1	Equilibrium	given	1.00124 (3)	1.00015 (3)
2.2	Equilibrium	critical search	1.00001 (3)	1.00015 (3)

Table 30. Serpent/SCF critical control rod bank positions.

CR Bank	ENDF/B-VII.1		JEFF-3.1.1	
	Case 1.2	Case 2.2	Case 1.2	Case 2.2
Bank G1 insertion (cm)	200	200	200	200
Bank G2 insertion (cm)	200	162	200	157
Bank G3 insertion (cm)	143	62	141	57
Bank G4 insertion (cm)	43	0	41	0
Bank S insertion (cm)	0	0	0	0

Selected parameters, such as power and temperature distributions, are presented hereafter only for the cases with fixed given control rod positions (cases 1.1 and 2.1). Figure 36 shows the axial power profile together with the corresponding fuel and coolant temperature distributions. Case 1.1, without xenon, exhibits a higher peak power compared to Case 2.1 with equilibrium xenon, due to the insertion of fewer control rods. The fuel temperature follows a trend similar to the axial power distribution. As the coolant flows through the core, a faster temperature increase is observed in Case 1.1 because of the higher power in the lower part of the core. However, all cases reach the same outlet temperature, since the total power generated in the core is constant. Negligible differences are observed between results obtained with ENDF/B-VII.1 and JEFF-3.1.1. Table 31 summarizes the main peak parameter in the figure.

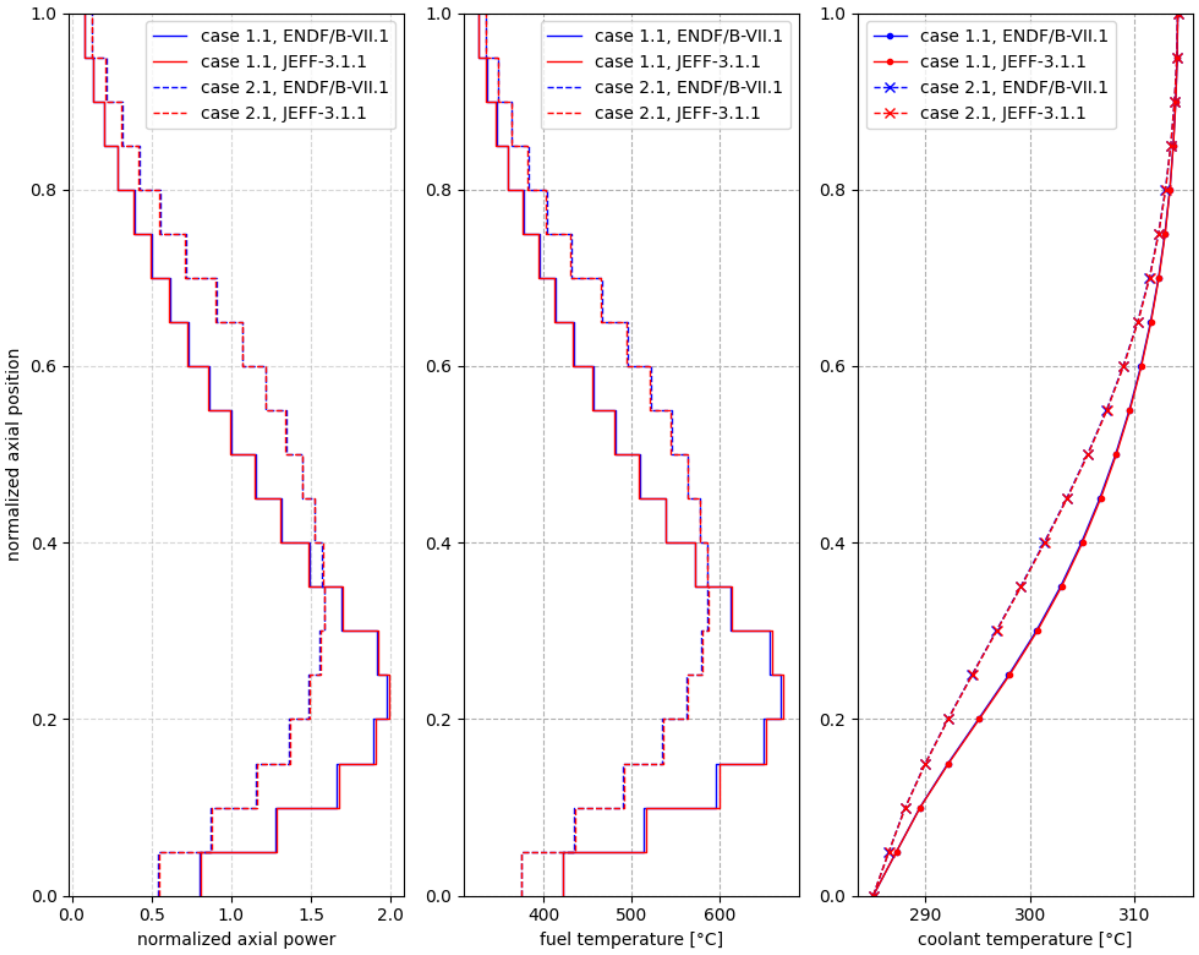

Figure 36. Serpent/SCF axial power, and axial fuel and coolant temperature profiles.

Table 31. Summary of peak values for the axial profile results.

Parameter	ENDF/B-VII.1		JEFF-3.1.1	
	Case 1.1	Case 2.1	Case 1.1	Case 2.1
Peak power	1.9774(4)	1.5827(3)	1.9890(4)	1.5867(3)
Peak fuel temperature (°C)	670.0	586.7	672.6	587.6
Outlet coolant temperature (°C)	314.2	314.2	314.2	314.2

Figure 37 shows the axially integrated assembly-wise power distribution. Again, higher peak power is observed in Case 1.1 and located in the central fuel assembly. Figure 38 and Figure 39 show the axially average assembly-wise fuel and coolant temperature distribution, respectively. Additionally selected pin-wise results for ENDF/B-VII.1 are provided in the Appendix.

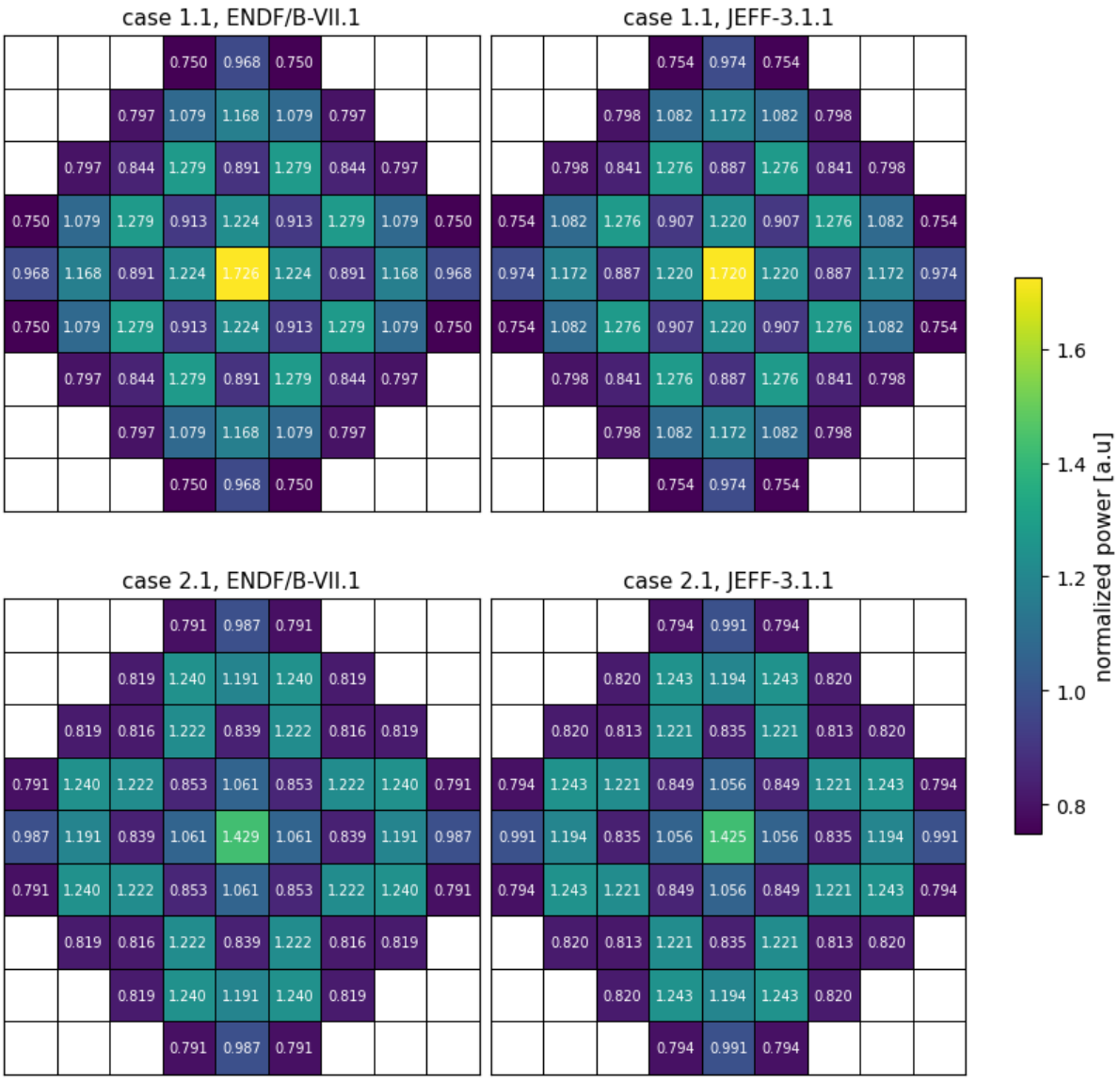

Figure 37. Serpent/SCF axially-integrated radial power distribution. The normalization is performed such that the sum of all power values equals the total number of fuel assemblies (57). Power is calculated using Serpent's detector with macroscopic reaction number -8, which accounts for the total fission energy production. The maximum uncertainty (1-sigma) in the values is 0.061%.

Co-funded by the European Union
UK Research and Innovation
The Research Council of Norway
Project funded by

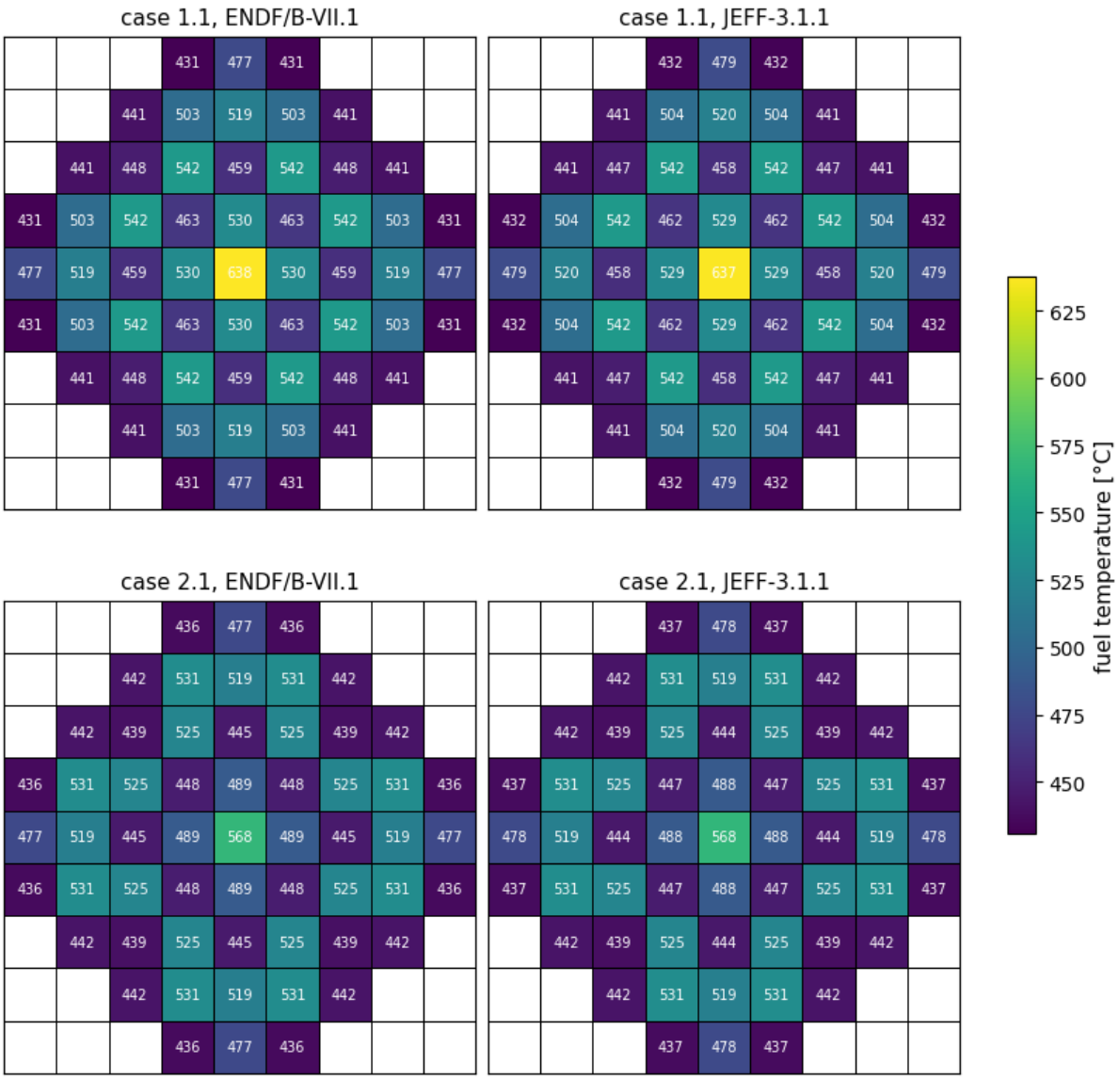

Figure 38. Serpent/SCF assembly-wise and axially-averaged fuel temperature.

Co-funded by the European Union
UK Research and Innovation
The Research Council of Norway
Project funded by

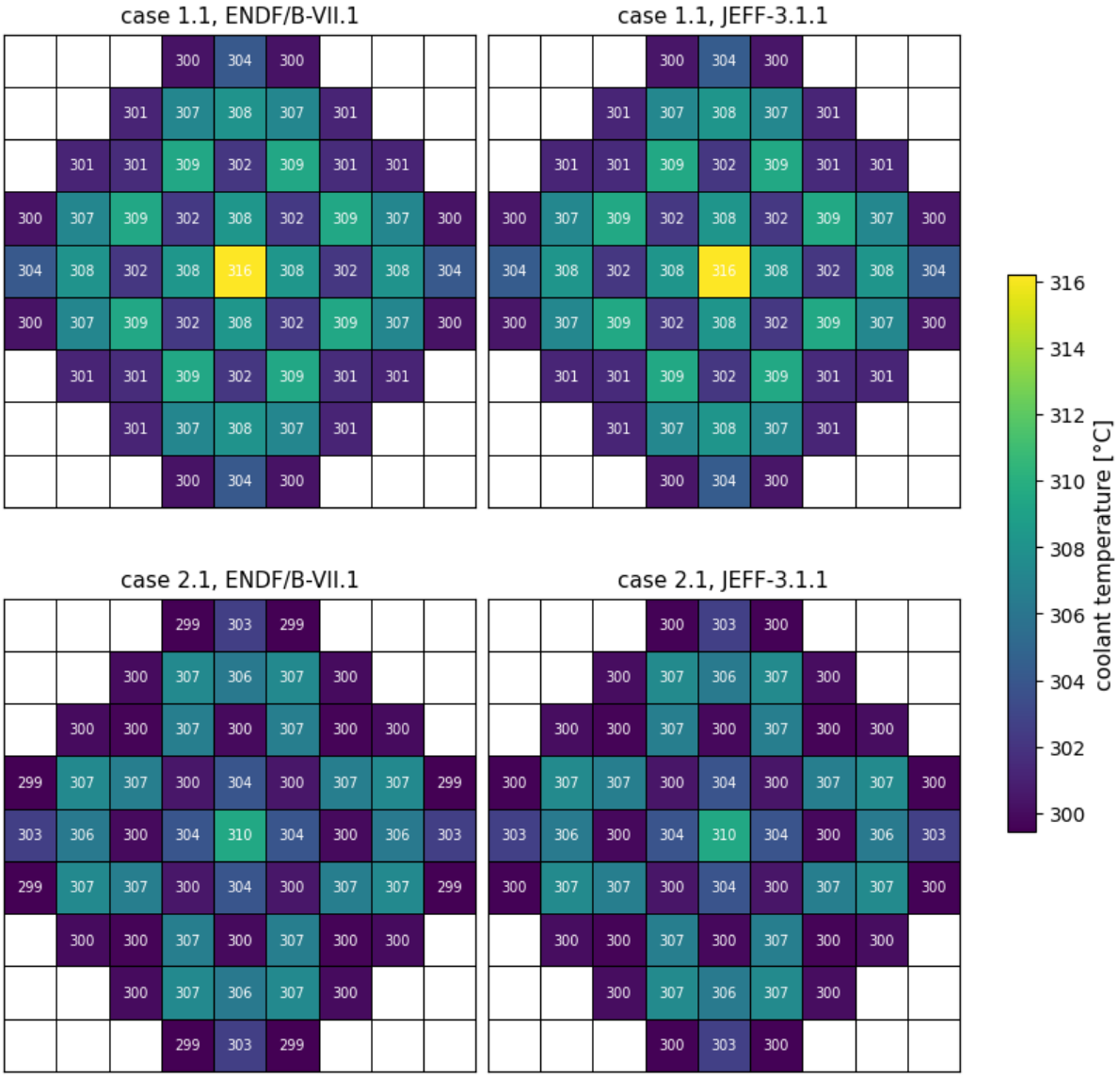

Figure 39. Serpent/SCF assembly-wise and axially-averaged coolant temperature.

9.2.2. Selected parameters for code benchmarking

9.2.2.1. Core K-eff at given control rods insertion

The insertion levels for absorbents have been set for cases 1.1, 2.1, 3.1 and 4.1. The k_{eff} value for each configuration has been calculated and is shown in Table 32 for ENDF/B7.1 and Table 33 for JEFF-3.1.1. The differences in reactivity from the reference KIT-SERPENT values are reported in Tables 34 and 35 for ENDF/B7.1 and JEFF-3.1.1, respectively. Only the results for configurations 1.1 and 2.1 are shown in these latter tables, since reference calculations were only performed for these two configurations.

Table 32. ENDF/B7.1. Keff values for HFP configurations where CRB insertion is specified.

Case	Power	Xenon	KIT-SERPENT	ASNR-CMS5	CEA-AP3-DIFF	CEA-AP3-SN	CEA-CRONOS2	KIT-CMS5	SSTC NRS-DYN3D	UJV-DYN3D
1.1	100%	null	1,00266	1,00383	1,00042	1,00317	1,00076	1,00406	0,99530	0,99501
2.1	100%	equilibrium	1,00124	1,00178	1,00001	1,00224	1,00041	1,00228	0,99627	0,99447
3.1	50%	null		1,00355			1,00061		0,99479	0,99377
4.1	50%	equilibrium		1,00245			1,00062		0,99623	0,99428

Table 33. JEFF-3.1.1. Keff values for HFP configurations where CRB insertion is specified.

Case	Power	Xenon	KIT-SERPENT	ASNR-CMS5	CEA-AP3-DIFF	CEA-AP3-SN	CEA-CRONOS2
1.1	100%	null	1,00159	1,00286	0,99960	1,00227	1,00015
2.1	100%	equilibrium	1,00015	1,00083	0,99951	1,00138	0,99980
3.1	50%	null		1,00255			0,99995
4.1	50%	equilibrium		1,00153			1,00001

Table 34. ENDF/B7.1. Differences in reactivity compared with the KIT-SERPENT reference.

Case	Power	Xenon	ASNR-CMS5	CEA-AP3-DIFF	CEA-AP3-SN	CEA-CRONOS2	KIT-CMS5	SSTC NRS-DYN3D	UJV-DYN3D
1.1	100%	null	+116	-223	+51	-189	+139	-738	-767
2.1	100%	equilibrium	+54	-123	+100	-83	+104	-498	-680

Table 35. JEFF-3.1.1. Differences in reactivity compared with the KIT-SERPENT reference.

Case	Power	Xenon	ASNR-CMS5	CEA-AP3-DIFF	CEA-AP3-SN	CEA-CRONOS2
1.1	100%	null	+126	-199	+68	-144
2.1	100%	equilibrium	+68	-64	+123	-35

Case 1.1 shows that activation of the thermal feedback models tends to accentuate differences in reactivity compared to the KIT-SERPENT reference results observed in HZP conditions (see Tables 17 and 18). This accentuation is between 100 and 300 pcm, except in the case of the CEA-AP3-Sn calculation, where the deviation is reduced by around 100 pcm.

When the xenon equilibrium models are activated, most of the deviations from the reference are reduced by between 35 and 240 pcm. However, for CEA-AP3-Sn, they increase by 50 pcm.

Ultimately, when the thermal feedback and xenon equilibrium models are activated, almost all of the results align with the reference core reactivity, with a deviation of less than 125 pcm.

9.2.2.2. Critical control rods insertion

The control rod banks (CRB) insertions that make the core critical are estimated for configurations 1.2 (null xenon) and 2.2 (xenon equilibrium) at 100% nominal power, with ENDF/B7.1 and JEFF-3.1.1 NDLs. The values are reported in Tables 36 and 37 for ENDF/B7.1, and Tables 38 and 39 for JEFF-3.1.1. As the CR insertion steps are 1 cm, and the differential control rod bank worth is between -20 and -50 pcm/cm, it is not possible to reach exactly the criticality. Therefore, the k_{eff} values are reported for every calculation. The critical insertion of every bank is reported in the tables, as well as the cumulative CR insertion, that is an abstract value permitting to represent the position of the four CR banks with only one value. Its definition is given in the benchmark specification (Prulhière, et al., 12/02/2025).

By knowing:

- the reactivity deviation with the reference at a given CR insertion $\Delta\rho^{CR\ given}$ (provided by configurations 1.1 and 2.1 and reported in Section 9.2.2.1);
- the difference of reactivity between each participant and the reference at critical CRB insertion $\Delta\rho^{critical}$ (obtained during configurations 1.2 and 2.2);
- the difference of CRB insertion with the reference ΔCR;

It is possible to estimate the differential control rod bank worth (CRBW) $\delta CRBW$ (in pcm/cm) with the following formula:

$$\delta CRBW = -\frac{\Delta\rho^{CR\ given} - \Delta\rho^{critical}}{\Delta CR}$$

This estimation is reported in the following tables.

Table 36. ENDF/B7.1. Critical CRB insertion of configuration 1.2 (null xenon).

	KIT-SERPENT	ASNR-CMS5	CEA-AP3-DIFF	CEA-CRONOS2	KIT-CMS5	SSTC NRS-DYN3D	UJV-DYN3D
G1 bank insertion [cm]	200	200	200	200	200	200	200
G2 bank insertion [cm]	200	200	200	200	200	200	200
G3 bank insertion [cm]	143	146	139	140	147	128	127
G4 bank insertion [cm]	43	46	39	40	47	28	27
S bank insertion [cm]	0	0	0	0	0	0	0
Cumulative CR insertion [cm]	343	346	339	340	347	328	327
Keff	1,00013	0,99988	0,99992	0,99982	0,99976	1,00002	1,00001
Δcumul. CR Insert / KIT-SERPENT [cm]	-	3	-4	-3	4	-15	-16
Δρ / KIT-SERPENT [pcm]	-	-25	-21	-31	-37	-11	-12
Differential CRBW [pcm/cm]	-	-47	-51	-53	-44	-48	-47

Table 37. ENDF/B7.1. Critical CRB insertion of configuration 2.2 (equilibrium xenon).

	KIT-SERPENT	ASNR-CMS5	CEA-AP3-DIFF	CEA-CRONOS2	KIT-CMS5	SSTC NRS-DYN3D	UJV-DYN3D
G1 bank insertion [cm]	200	200	200	200	200	200	200
G2 bank insertion [cm]	162	165	157	159	167	140	127
G3 bank insertion [cm]	62	65	57	59	67	40	27
G4 bank insertion [cm]	0	0	0	0	0	0	0
S bank insertion [cm]	0	0	0	0	0	0	0
Cumulative CR insertion [cm]	262	265	257	259	267	240	227
Keff	1,00001	0,99992	1,00001	0,999985	0,99991	0,99992	1,000063
Δcumul. CR Insert / KIT-SERPENT [cm]	-	3	-5	-3	5	-22	-35
Δρ / KIT-SERPENT [pcm]	-	-9	0	-3	-10	-9	5
Differential CRBW [pcm/cm]	-	-21	-25	-27	-23	-22	-20

Table 38. JEFF-3.1.1. Critical CRB insertion of configuration 1.2 (null xenon).

	KIT-SERPENT	ASNR-CMS5	CEA-AP3-DIFF	CEA-CRONOS2
G1 bank insertion [cm]	200	200	200	200
G2 bank insertion [cm]	200	200	200	200
G3 bank insertion [cm]	141	144	137	139
G4 bank insertion [cm]	41	44	37	39
S bank insertion [cm]	0	0	0	0
Cumulative CR insertion [cm]	341	344	337	339
Keff	1,00014	0,99987	1,00008	0,99969
Δcumul. CR Insert / KIT-SERPENT [cm]	-	3	-4	-2
Δρ / KIT-SERPENT [pcm]	-	-27	-6	-45
Differential CRBW [pcm/cm]	-	-51	-48	-50

Table 39. JEFF-3.1.1. Critical CRB insertion of configuration 2.2 (equilibrium xenon).

	KIT-SERPENT	ASNR-CMS5	CEA-AP3-DIFF	CEA-CRONOS2
G1 bank insertion [cm]	200	200	200	200
G2 bank insertion [cm]	157	161	155	156
G3 bank insertion [cm]	57	61	55	56
G4 bank insertion [cm]	0	0	0	0
S bank insertion [cm]	0	0	0	0
Cumulative CR insertion [cm]	257	261	255	256
Keff	1,00015	0,99992	0,99995	1,000052
Δcumul. CR Insert / KIT-SERPENT [cm]	-	4	-2	-1
Δρ / KIT-SERPENT [pcm]	-	-23	-20	-10
Differential CRBW [pcm/cm]	-	-23	-22	-25

The differential CRBW are evaluated at almost the same values by all the participants, considering that this value depends on the control rods position, on the CRW of each participant, on the core reactivity, the NDL, etc. The differential CRBW is around -49 pcm/cm for the configuration 1.2 (variations between -53 and -44 pcm/cm) and is around -23 pcm/cm for the configuration 2.2 (variations between -27 and -20 pcm/cm).

It implies relatively weak differences in critical CR insertion: between -5 and 5 cm of cumulative CRB insertion for most of the calculations. Thus, the cumulative CR insertion is near 342 cm in configuration 1.2, and near 260 cm for configuration 2.2. An exception concerns the code DYN3D used by UJV and SSTC NRS: due to the great difference of critical core reactivity during configurations 1.1 and 2.1, the control rods are not at the same level of insertion than the reference, which makes the differential CRBW very different for these calculations and makes the critical CR insertion very different too.

9.2.2.3. Power distribution at given control rods insertion

Each participant has evaluated the power distribution within the active zone of the core. These values were integrated assembly-wise and axially to represent the power distribution on a 2D radial map. These values were also integrated core-wise and on 10 cm axial mesh to represent the power distribution on a 1D axial profile.

Each power 2D map was compared to the corresponding reference one to produce power deviation 2D radial maps. To summarise these results, each power deviation 2D map is represented as a box-and-whiskers plot, as defined in Figure 21. These plots are given in Figure 40 for configuration 1.1 (100% NP, null xenon) and Figure 42 for configuration 2.1 (100% NP, xenon at equilibrium), with both ENDF/B7.1 on the left and JEFF-3.1.1 NDL on the right. The power 1D axial profiles are given in Figure 41 for ENDF/B7.1 (left) and JEFF-3.1.1 (right).

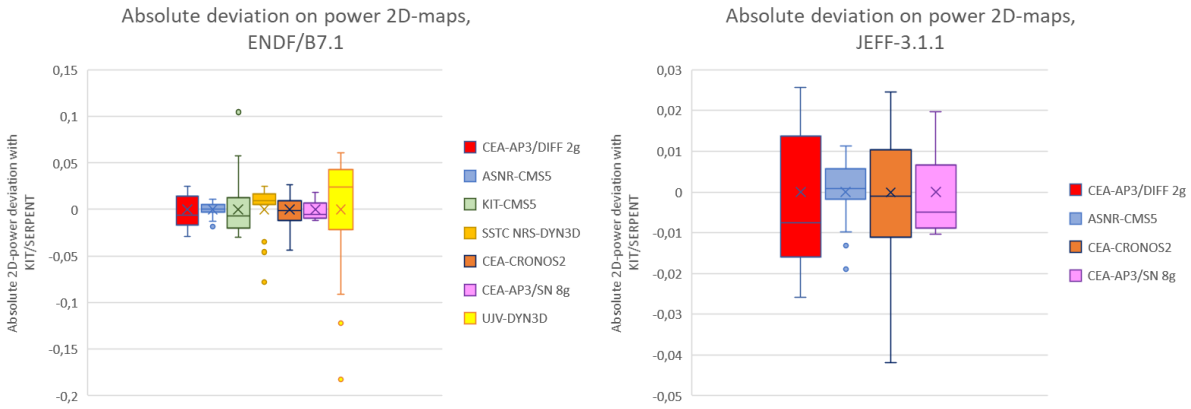

Figure 40. Absolute deviation on power 2D-maps for config 1.1.

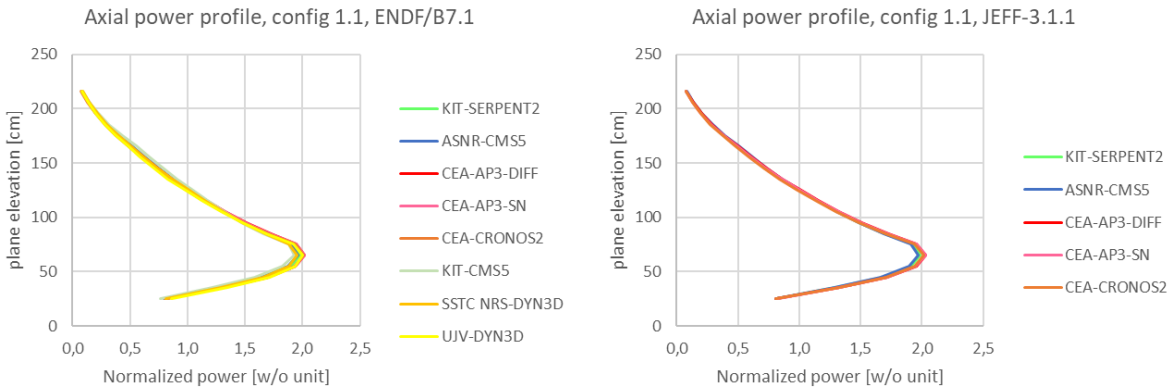

Figure 41. Power 1D axial profiles for config 1.1.

For the config 1.1, the deviations on power 2D-maps show a good behaviour, with most of the results comprised between -0.05 and +0.05. The 1D axial power deviations compared to the reference are very good too, because they are comprised between:

- -0.075 (KIT-CMS5) and +0.061 (UJV-DYN3D) for ENDF/B7.1;
- -0.018 (CEA-CRONOS2) and +0.045 (CEA-APOLLO3-DIFFUSION) for JEFF-3.1.1.

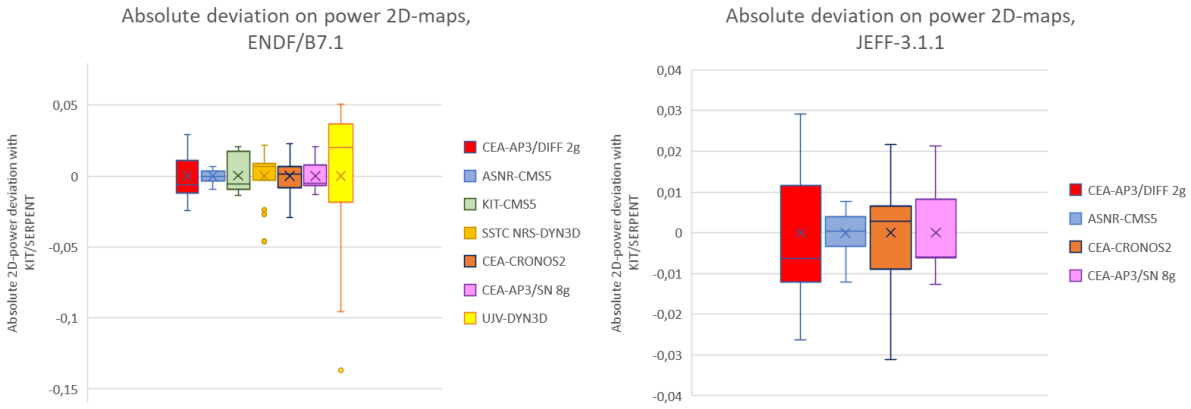

Figure 42. Absolute deviation on power 2D-maps for config 2.1.

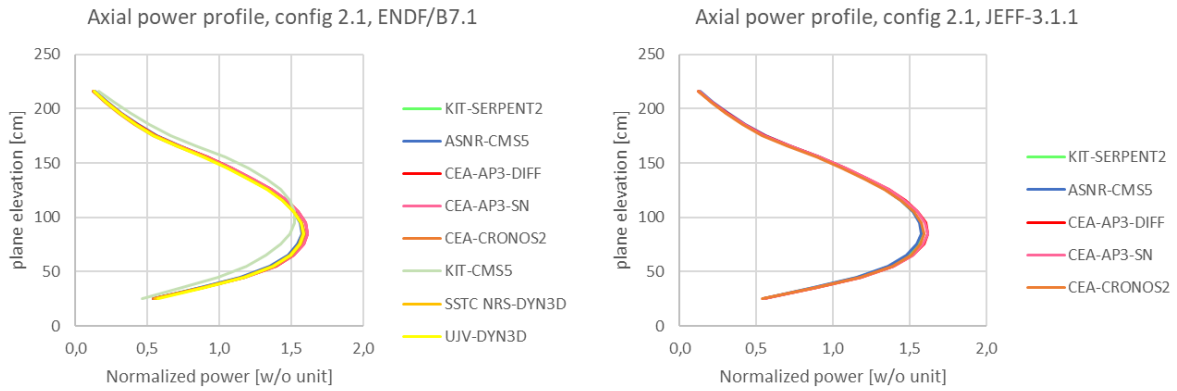

Figure 43. Power 1D axial profiles for config 2.1.

The axial power profile of KIT-CMS5 result for config 2.1 is very different from the other codes. Plane-by-plane, we can see differences comprised between -0.17 and +0.13. Indeed, we can see a shift upward of the KIT-CMS5 axial power profile compared to the other codes.
For the config 2.1, excepted the KIT-CMS5 results, the 1D axial power deviations compared to the reference are comprised between:

- -0.018 (UJV-DYN3D) and +0.033 (CEA-APOLLO3-DIFFUSION) for ENDF/B7.1,
- -0.012 (ASNR-CMS5) and +0.032 (CEA-APOLLO3-DIFFSUION) for JEFF-3.1.1.

9.2.2.4. Fuel temperature distribution at given control rods insertion

The same representations than for power distributions is done with fuel temperatures.

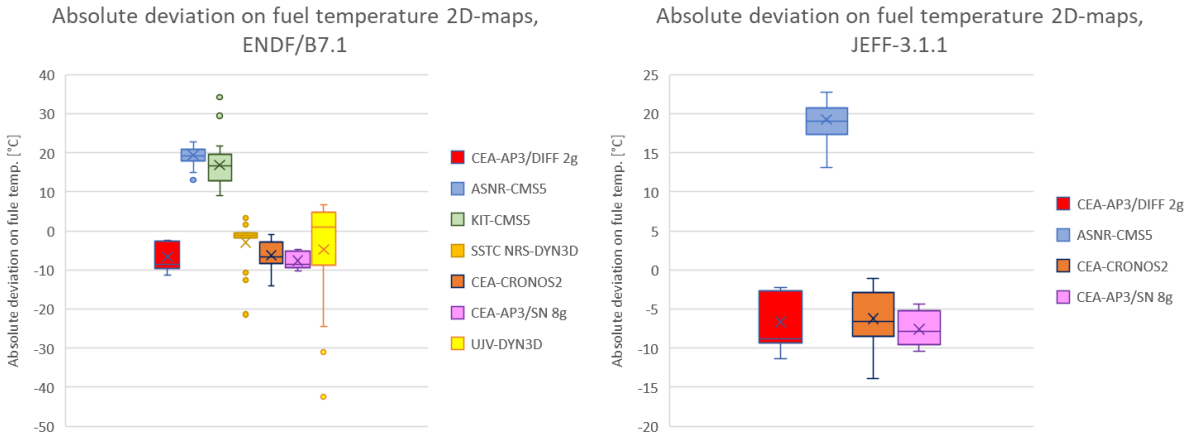

Figure 44. Absolute deviation on fuel temperature 2D-maps for config 1.1.

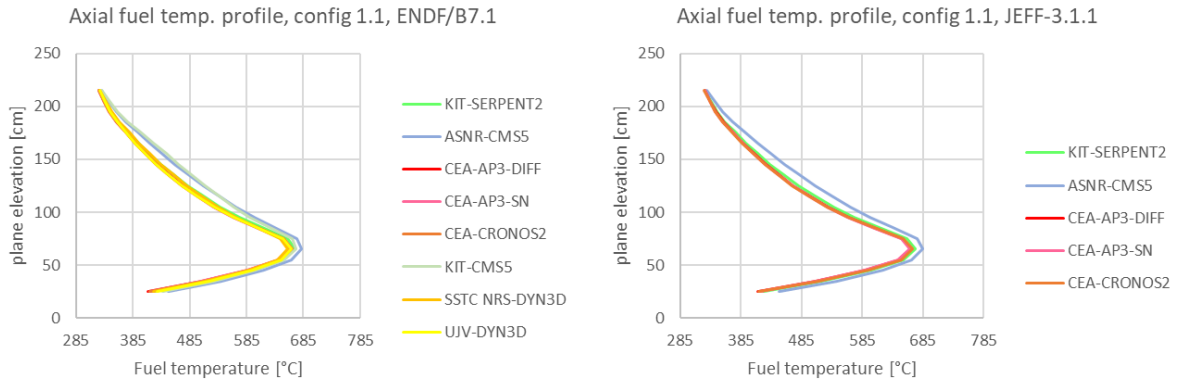

Figure 45. Fuel temperature 1D axial profiles for config 1.1.

For the config 1.1, the evaluation of the fuel temperature is very different for CMS5 code system compared to other codes. On the fuel temperature 2D maps, we see an increase of almost +20 °C for CMS5 compared to the reference provided by KIT-SERPENT-SUBCHANFLOW whereas the other codes tend to underestimate this value of almost -6 °C.
The 1D axial fuel temperature deviations compared to the reference show the same trends, and are comprised between:

- -14 °C (SSTC NRS-DYN3D) and +32 °C (KIT-CMS5) for ENDF/B7.1;
- -11 °C (CEA-APOLLO3-Sn) and +28 °C (ASNR-CMS5) for JEFF-3.1.1.

A possible explanation is that ASNR and KIT used the default thermal conductivity values in SIMULATE5, rather than those specified in the benchmark.

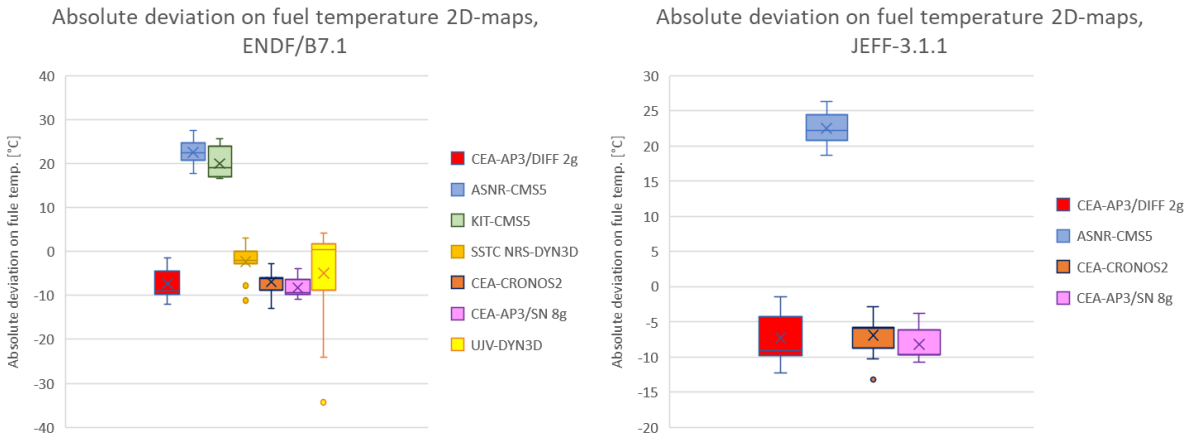

Figure 46. Absolute deviation on fuel temperature 2D-maps for config 2.1.

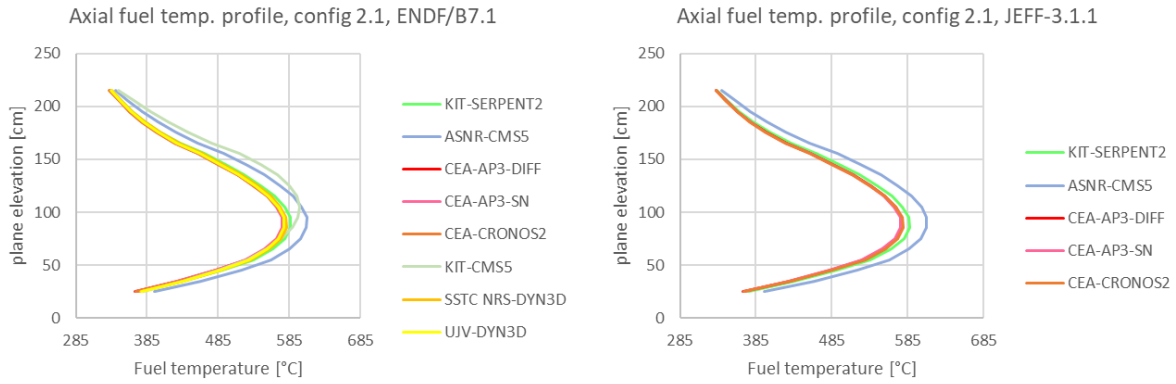

Figure 47. Fuel temperature 1D axial profiles for config 2.1.

The observations of the fuel temperature deviation in config 2.1 are the same than in config 1.1, and are coherent with the comments concerning the power deviations:

- Fuel temperatures computed by ASNR-CMS5 and KIT-CMS5 are almost +20 °C above the reference ones;
- A shift upward the axial fuel temperature profile is observed for KIT-CMS5 in case of config 2.1, similar to the shift in axial power;
- Apart from CMS5, other codes tend to underestimate the fuel temperature regarding the reference, by almost -6 °C.

9.2.2.5. Water temperature distribution at given control rods insertion

The same representations than for power distributions is done with coolant temperatures.

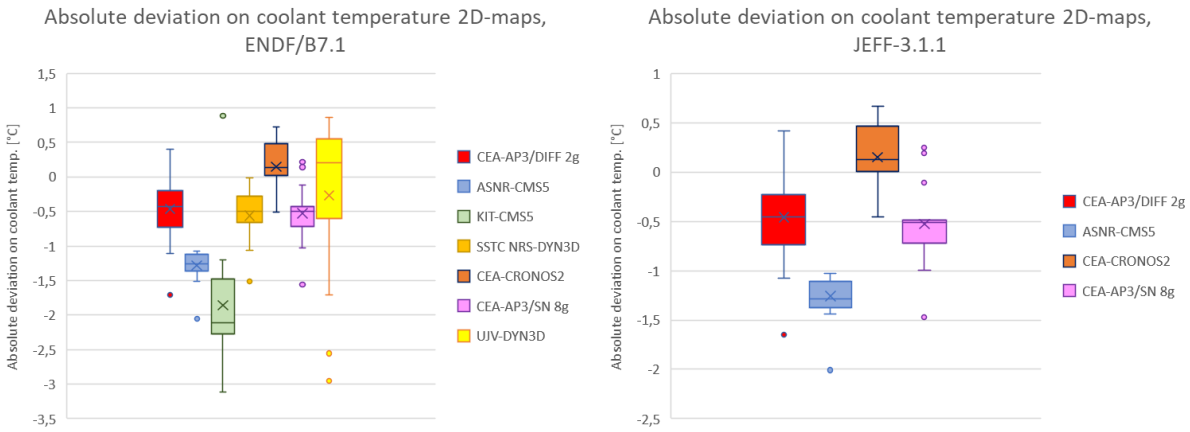

Figure 48. Absolute deviation on coolant temperature 2D-maps for config 1.1.

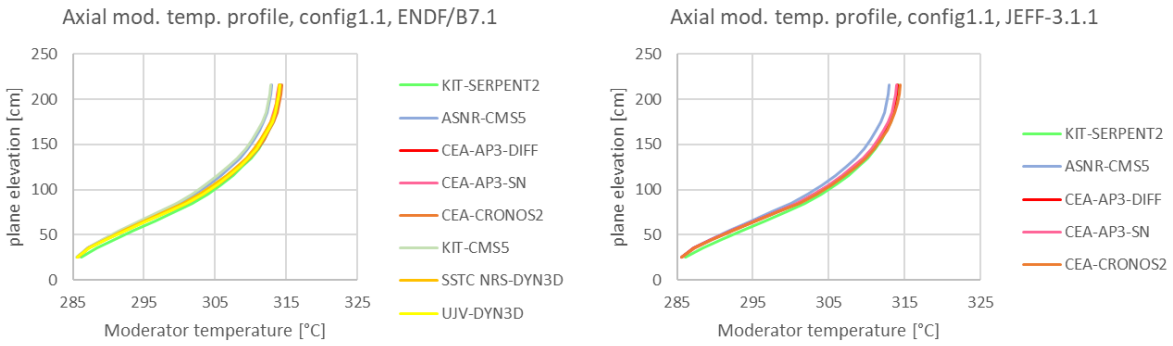

Figure 49. Coolant temperature 1D axial profiles for config 1.1.

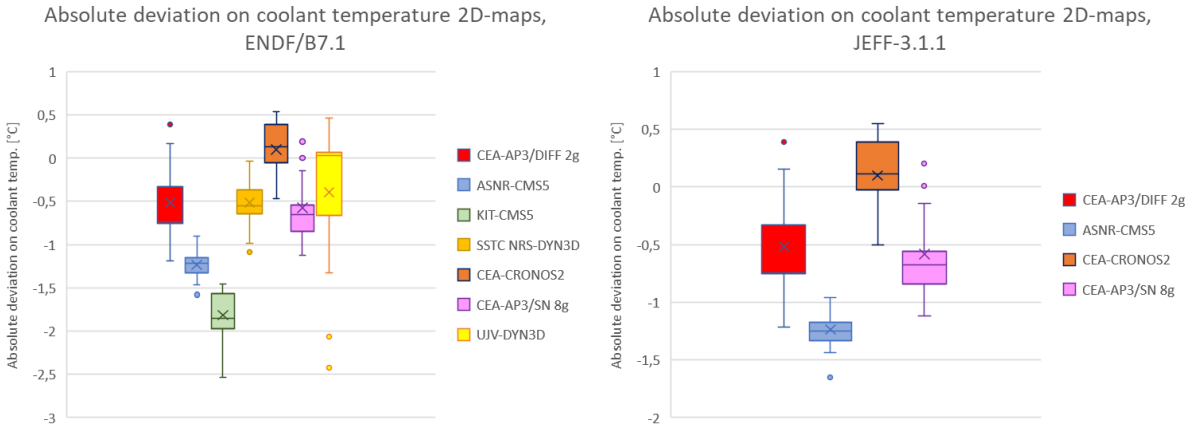

Figure 50. Absolute deviation on coolant temperature 2D-maps for config 2.1.

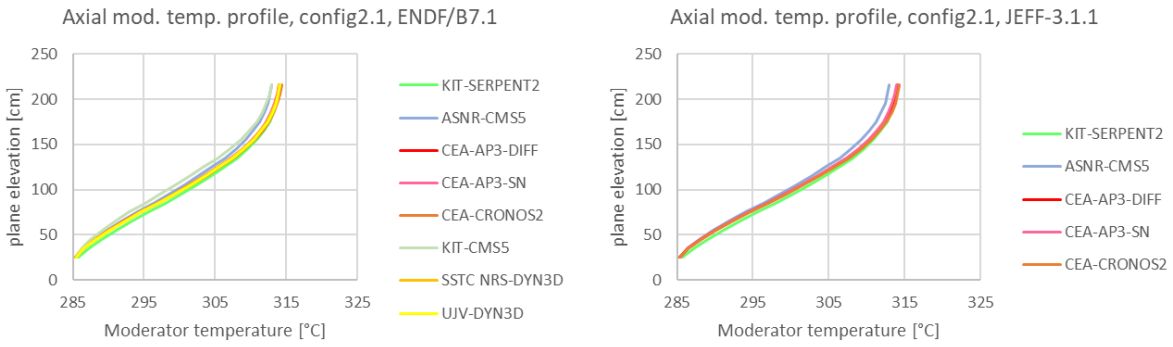

Figure 51. Coolant temperature 1D axial profiles for config 2.1.

Coolant temperature deviations are limited, compared to fuel ones. Both configurations, without (1.1) and with (2.1) xenon, present the same behaviour:

- Most of the codes underestimate the coolant temperature by almost -0.5 °C;
- CMS5, used by ASNR and KIT, show a larger underestimation of around -1.5 °C;
- CRONOS2 shows a singular behaviour, with a slight overestimation of around 0.1 °C.

9.2.3. Conclusions of code benchmarking at HFP conditions

Calculations under HFP conditions required the joint consideration of neutron physics and thermohydraulics. Several codes were employed for this purpose. The first type, carried out by KIT, involves coupling the SERPENT Monte Carlo code with SUBCHANFLOW. As this represents the simulation at the highest fidelity level, it has been adopted as the reference in this study. The advanced method is represented by CEA-APOLLO3-Sn calculations. In this code, the THEDI model is responsible for the thermohydraulics. Several industry-grade code systems follow, including ASNR-CMS5, KIT-CMS5, CEA-APOLLO3-DIFFUSION, CEA-CRONOS2, SSTC NRS-DYN3D and UJV-DYN3D. All these codes were used with their built-in thermohydraulics models.

Two main configurations were simulated at HFP state: 1.x with xenon forced to be null, and 2.x with xenon at equilibrium. Compared to the HZP condition, deviations in reactivity values are more pronounced (around 100 to 300 pcm) when the thermal feedback are activated and the xenon deactivated. Activating the xenon equilibrium tends to reduce these core reactivity deviations, allowing reactivity deviations to be brought back under 125 pcm.

Most of the codes have been used to estimate the insertion of control rods that make the core critical. These insertions are estimated to be almost the same value as the reference, with an insertion range of ±5 cm, except in the case of the DYN3D code where the difference of insertion reaches -15 to -35 cm. This seems to be mainly due to the evaluation of the core reactivity with DYN3D that is different from the reference by almost -500 to -800 pcm. This critical CR insertion stage permits to estimate roughly the differential control rod bank worth at the neighbourhood of the criticality. The estimation was -49 ± 5 pcm for the configuration 1.2, and -23 ± 4 pcm for the configuration 2.2.

Furthermore, the distribution of power, fuel and coolant temperature within the core were also compared. The power distributions were found to be very similar, with most of the results ranging from ±0.05 around the reference point. An exception was observed with the axial power profile of KIT-CMS5 in the configuration 2.1, with xenon at equilibrium. For this configuration, the axial power profile was shifted upwards.

For the fuel temperature distribution, we observed two classes of results:

- CMS5 results, whose setting deviate from the specifications because of using the default conductivity laws, show a deviation of around +20 °C regarding the reference,
- Other codes tend to underestimate the fuel temperature by almost -6 °C compared to the reference.

The coolant temperature calculations agree with the reference, because most of the codes underestimate this temperature by almost -0.5 °C, CMS5 underestimate by around -1.5 °C and CRONOS2 slightly overestimate of around +0.1 °C.

10. Final conclusions

This document details the results of the calculations performed for Task 7.2.1 of the EASI-SMR project, focused on the PRATIC core. The objective of this task was to calibrate the calculation codes against each other. This was first achieved in a purely neutronics phase, where the core was simulated at HZP conditions. This was then followed by a phase that coupled neutronics and thermohydraulics, in which HFP conditions were simulated. Various ranges of simulation codes were compared: reference codes using the Monte Carlo method, advanced codes based on neutron transport theory, and commercial or industry-grade codes.

In the first phase, excellent agreement was observed between the Monte Carlo codes in terms of the calculated reactivity values, power distributions and reactivity coefficients. However, a few discrepancies highlighted the need to specify precisely which outputs were to be compared. As the codes did not calculate the same quantities, this may have led to discrepancies.
In contrast, the results produced by advanced computational methods are often disappointing. Their performance is comparable to, or in some cases worse than, that of industrial codes, despite requiring substantially greater computational resources. One possible explanation is that these methods do not fully benefit from the most relevant bias corrections derived from operational feedback on industrial codes. As a result, while certain computational biases are reduced, others may be amplified. The delicate balance between compensating biases typically observed in industrial codes is therefore disrupted, leading to deviations from the reference results.
In terms of industrial-scale calculations based on solving the diffusion equation, we have observed two categories of results. The first category comprises those that perform very well against the reference, while the second category comprises those whose results show greater discrepancies. For the latter category, it is not the codes themselves that are in question, but rather the calculation methods chosen by users within these codes. Indeed, soluble boron-free SMR cores exhibit spatial heterogeneities that locally disrupt the spatial distribution and spectrum of the neutron flux. These heterogeneities include gadolinium rods, control rods and the radial reflector, which is mainly made of steel. To account for these spatial heterogeneities correctly in neutron calculation schemes, the following recommendations should be established:

- Perform two-level lattice calculations: self-shielding based on an energy mesh of almost 300 groups or more, followed by determination of the spatial shape of the flux using the MoC method.
- Describe the angular variable with P3 anisotropy in lattice calculations.
- Define spatial meshes in core calculations that are finer than the industry-standard 2x2 radial cell grids per fuel assembly.

These recommendations are preliminary and will need to be confirmed by more comprehensive analyses.

In the second phase, these types of neutron calculation were coupled with thermohydraulic models to simulate the core under HFP conditions. Activating thermohydraulic feedback mechanisms and establishing xenon equilibrium reduced the discrepancies between the codes and the reference more than had been observed during Phase 1. Most of the results obtained are in very good agreement with the reference. However, some participants used the default thermal conductivity laws in their code without adhering to the benchmark conditions, resulting in a change in fuel temperature of around 20°C. Advanced calculations did not show any significant improvement in the quality of the results in this phase either, compared with standard industrial calculations.

In conclusion, considering the efforts undertaken to ensure a high level of reliability in the reference calculations, and the satisfactory agreement between the various code results and the reference data, Task 7.2.1, focused on the characterization of the PRATIC core with fresh fuel, can be regarded as successfully complete. The PRATIC core has been fully characterised under conditions ranging from zero power to full power.

11. Outlook

Based on the results obtained by the participants in Task 7.2, and perhaps with the support of additional analysis, it would be beneficial to further develop this work by addressing the following topics:

Monte Carlo methods:

- The origin of discrepancies between SERPENT and TRIPOLI4. One hypothesis to consider is how the various models (Thermal Scattering Law, Sampling the Velocity of the Target, Asymptotic Kernel, etc.) treat neutron scattering phenomena in the 1–50 eV range and their respective cut-off energies.

Deterministic methods:

- Advanced methods based on solving the neutron transport equation:
  - Seeking to improve the predictability of these methods compared to standard industrial methods. It is necessary to ensure a balanced trade-off between positive and negative calculation biases, as with industrial methods. To this end, a detailed analysis of modelling biases and a rebalancing exercise should be undertaken. However, this would require a significant amount of work.

- Standard industrial methods based on the diffusion equation, in line with soluble-boron-free light water specificities:
  - Energy mesh. CASMO5/SIMULATE5 results based on a 4-group energy mesh seem to be better than 2-group or 8-group mesh. The trend for other codes such as APOLLO2/CRONOS2 or APOLLO3 seems to be different, with the best results obtained with a 2-group energy mesh. Further investigation of this topic would be worthwhile in order to confirm these trends and explain their origins.
  - Anisotropy. Results obtained by considering P3 anisotropy were closer to the reference than those obtained by considering P0 anisotropy, even with a transport correction applied. This trend is less pronounced in large PWRs, whose reactivity control uses soluble boron. One hypothesis to explain this is that SBF-type cores contain more pronounced neutron flux heterogeneities due to the extensive use of neutron poisons and the insertion of control rods. It would be worthwhile testing this hypothesis to confirm whether the SBF-SMR core simulations require P3 anisotropy treatment because of their specific characteristics.

The EASI-SMR project does not aim to explore these topics in depth, but they do provide ideas for relevant areas of scientific research.

12. Bibliography

Bahadir, T., Lindahl, S. Ö., & Studsvik Scandpower Ab. (April 12-15 (2009)). Studsvik's Next Generation Nodal Code SIMULATE-5. *Proc. Int. Conf. on Advances in Nuclear Fuel Management IV (ANFM IV)*. Hilton Head, SC, USA.

Becker, B. (2010). *On the influence of the resonance scattering treatment in Monte Carlo codes on high temperature reactor characteristics.* University of Stuttgart, Germany: Institut fur Kernenergetik und Energiesysteme.

Brun, E., Damian, F., Diop, C. M., Dumonteil, E., Hugot, F. X., Jouanne, C., . . . Zoia, A. (2015). Tripoli-4®, CEA, EDF and AREVA reference Monte Carlo code. *Annals of Nuclear Energy, 82*, 151-160. doi:https://doi.org/10.1016/j.anucene.2014.07.053

Brun, R., & Rademakers, F. (1997, Sept.). ROOT — An object oriented data analysis framework. *Nuclear Instruments and Methods in Physics Research Section A: Accelerators, Spectrometers, Detectors and Associated Equipment, 389*(1-2), 81-86. doi:https://doi.org/10.1016/S0168-9002(97)00048-X

Chadwick, M. B., Herman, M., Oblozinsky, P., Dunn, M. E., Danon, Y., Kahler, A. C., . . . Kawano, T. (2011). ENDF/B-VII.1 Nuclear Data for Science and Technology: Cross Sections, Covariances, Fission Product Yields and Decay Data. *Nuclear Data Sheets, 112*(12), 2887-2996. doi:https://doi.org/10.1016/j.nds.2011.11.002

Chadwick, M. B., Obložinský, P., Herman, M., Greene, N. M., McKnight, R. D., Smith, D. L., . . . van der Marck, S. C. (2006). ENDF/B-VII.0: Next Generation Evaluated Nuclear Data Library for Nuclear Science and Technology. *Nuclear Data Sheets, 107*(12), 2931-3060. doi:https://doi.org/10.1016/j.nds.2006.11.001

Downar, T., Xu, Y., & Seker, V. (2009). *PARCS v3.0, U.S. NRC Core Neutronics Simulator - THEORY MANUAL.* Ann Arbor, MI, U.S.A.: Department of Nuclear Engineering and Radiological Sciences, University of Michigan.

Dunford, C. L. (1991). *Evaluated Nuclear Data File.* National Nuclear Data Center. Upton, NY 11973, USA: Brookhaven National Laboratory. Retrieved from https://scispace.com/pdf/evaluated-nuclear-data-file-endf-b-vi-6pui5xwrmy.pdf

EASI-SMR Project. (2025). Retrieved from EASI-SMR website: https://easi-smr.eu/

European SMR pre-Partnership Workstream 5 –Research, Development, and Innovation Roadmap. (2023). Retrieved from SNETP: https://snetp.eu/wp-content/uploads/2023/07/European-SMR-pre-Partnership-WS5-report-and-roadmap-30-June-2023.pdf

Ferraro, D., Garcia, M., Imke, U., Valtavirta, V., Leppänen, J., & Sanchez-Espinoza, V. (2019). Serpent/SCF pin-level multiphysics solutions for the VERA Fuel Assembly benchmark. *Annals of Nucler Energy 128*.

Hfaiedh, N., & Santamarina, A. (2005). Determination of the optimized SHEM mesh for neutron transport calculations. *M&C - The Int. Top. Mtg. on Mathematics and Computation, Supercomputing, Reactor Physics and Nuclear and Biological Applications.* Avignon, France: ANS.

Hugot, F. X., Jinaphanh, A., Jouanne, C., Larmier, C., Lee, Y. K., Mancusi, D., . . . Zoia, A. (2024). Overview of the TRIPOLI-4 Monte Carlo code, version 12. *EPJ Nuclear Sci. Technol., 10*(17). doi:https://doi.org/10.1051/epjn/2024018

IAEA. (2024). *Small Modular Reactors: Advances in SMR Developments*. Vienna: IAEA. doi:https://doi.org/10.61092/iaea.3o4h-svum

Imke, U., & Sanchez, V. (2012). Validation of the Subchannel Code SUBCHANFLOW using the NUPEC PWR Tests (PSBT). *Science and Technology of Nuclear Installations, 12*. Récupéré sur https://doi.org/10.1155/2012/465059

Jung, Y. S. (2013). Practical numerical reactor employing direct whole core neutron transport and subchannel thermal/hydraulic solvers. *Annals of Nuclear Energy, 62*, 357-374.

Lautard, J. J., Loubière, S., & Feudon-Magnaud, C. (1992). CRONOS: A modular computational system for neutronic core calculations. *Specialists meeting on advanced calculational methods for power reactors; Technical committee meeting and workshop on LWR core design parameters* (pp. 42-50). Cadarache (France) & Rez (Czechoslovakia): International Atomic Energy Agency (IAEA).

Lautard, J. J., Schneider, D., & Baudron, A. M. (1999). Mixed Dual Methods for Neutronic Reactor Core Calculations in the CRONOS System. *M&C - The Int. Conf. on Mathematics and Computation, Reactor Physics and Environmental Analysis in Nuclear Applications* (pp. 814-826). Madrid (Spain): Senda Editorial S.A.

LDR lite benchmark. (2025, July 23). Retrieved from https://serpent.vtt.fi/kraken/index.php?title=LDR_lite_benchmark

Leppänen, J., Valtavirta, V., Rintala, A., & Tuominen, R. (2025). Status of Serpent Monte Carlo code in 2024. *EPJ Nuclear Sci. Technol. 11 3*.

Mancusi, D., Brun, E., Dechenaux, B., Fröhlicher, K., Gonçalves, T., Jinaphanh, A., . . . Zoia, A. (2024). Overview of TRIPOLI-5, a Monte Carlo code for HPC. *EPJ Nuclear Sci. Technol., 10*(26). doi:https://doi.org/10.1051/epjn/2024028

Mercatali, L., Huaccho Zavala, G., & Sanchez Espinoza, V. H. (April 19 – 23, 2026). Steady-state characterization of the PRATIC core at Hot Zero Power with the CMS5 code package and verification against Serpent2. *PHYSOR2026.* Torino, Italy.

Moller, J. Y., & Lautard, J. J. (2011). Minaret, A Deterministic Neutron Transport Solver for Nuclear Core Calculation. *M&C - The Int. Conf. on Mathematics and Computational Methods Applied to Nuclear Science and Engineering.* Rio de Janeiro (Brazil): Latin American Section (LAS) / American Nuclear Society (ANS). Retrieved from https://inis.iaea.org/records/7xgs2-pps94/files/48022288.pdf

Mosca, P., Bourhrara, L., Calloo , A., Gammicchia, A., Goubioud, F., Lei-Mao, L., . . . Vezzoni, B. (2023). APOLLO3®: Overview of the new code capabilities for reactor physics analysis. *M&C - The Int. Conf. on Mathematics and Computational Methods Applied to Nuclear Science and Engineering.* Niagara Falls, Ontario, Canada. Retrieved from https://cea.hal.science/cea-04469092

Patricot, C., Lenain, R., & Caron, D. (2019). Upgrade of APOLLO3® internal thermohydraulic feedback model with THEDI, and application to a control-rod ejection accident. *M&C - The Int. Conf. on Mathematics and Computational Methods Applied to Nuclear Science and Engineering.* Portland, Oregon, USA: ANS. Retrieved from https://cea.hal.science/cea-02623807v1

Prulhière, G., Eustache, A., Vezzoni, B., Girardi, E., Tiberga, M., & Dor, M.-A. (12/02/2025). *D7.1 Specifications of PRATIC fresh core at BOC conditions.* https://easi-smr.eu/docs/resources/EASI-SMR_D7.1_Specification_of_PRATIC_fresh_core_at_BOC_conditions.pdf: EASI-SMR Project.

Rhodes, J., Smith, K., & Lee, D. (Sept. 10-14, 2006). CASMO-5 development and applications. *PHYSOR 2006.* Vancouver, BC, Canada.

Sanchez, R., Zmijarevic, I., Coste-Delclaux, M., Masiello, E., Santandrea, S., Martinolli, E., . . . Guler, N. (2010, October). Apollo2: year 2010. *Nuclear Engineering and Technology, 42*(5), 474-499. doi:10.5516/NET.2010.42.5.474

Santamarina, A., Bernard, D., & Rugama, Y. (2009). *The JEFF-3.1.1 Nuclear Data Library. Validation Results from JEF-2.2 to JEFF-3.1.1.* Paris: OECD NEA No. 6807. Retrieved from https://www.oecd-nea.org/upload/docs/application/pdf/2019-12/nea6807-jeff22.pdf

Santamarina, A., Bernard, D., Blaise, P., Erradi, L., Leconte, P., Le Tellier, R., . . . Vidal, J. F. (2009). APOLLO2.8: A validated code package for PWR neutronics calculations. *Advances in Nuclear Fuel Management IV (ANFM).* Hilton Head Island, South Carolina, USA: American Nuclear Society.

Santandrea, S., Sanchez, R., & Mosca, P. (2008). A Linear Surface Characteristics Approximation for Neutron Transport in Unstructured Meshes. *Nuclear Science and Engineering, 160*(1), 23-40. doi:https://doi.org/10.13182/NSE07-69

Tulkki, V., Sanchez-Espinoza, V. H., & Sobecki, N. (2025). Main goals and research outcomes of the EU Projects ELSMOR, McSAFER, and EASI-SMR: regulatory, experimental and analytical safety-related investigations. *EPJ Nuclear Sci. Technol., 11*(33). doi:https://doi.org/10.1051/epjn/2025023

Vuiart, R., Eustache, A., Eveillard, S., & Prulhière, G. (2024). PRATIC: A soluble-boron-free, pressurized water cooled, SMR core benchmark. *EPJ Nuclear Sci. Technol., 10*(25). doi:https://doi.org/10.1051/epjn/2024026

Appendix

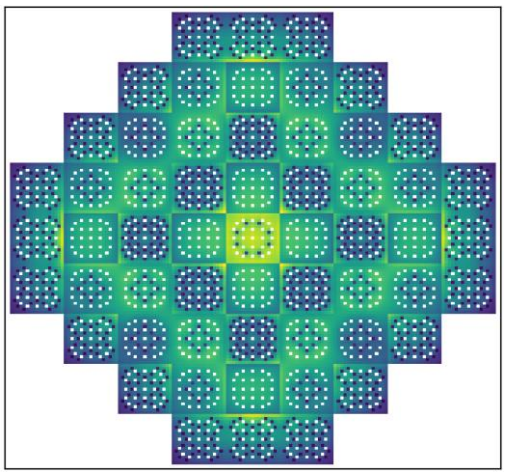

Figure 52. (Case 1.1, ENDF/B-VII.1) Serpent/SCF axially-integrated pin power distribution.

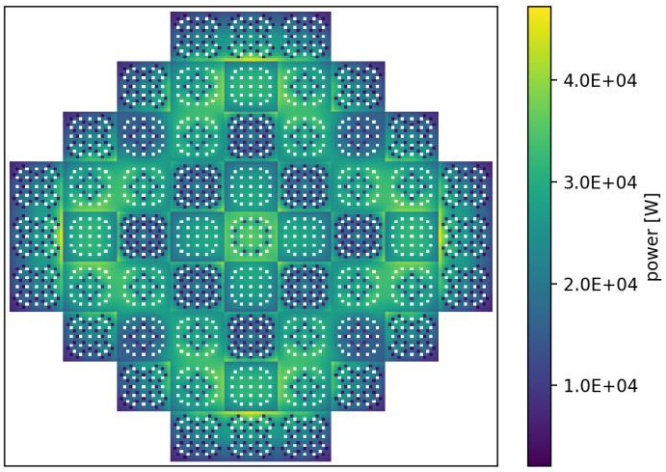

Figure 53. (Case 2.1, ENDF/B-VII.1) Serpent/SCF axially-integrated pin power distribution.

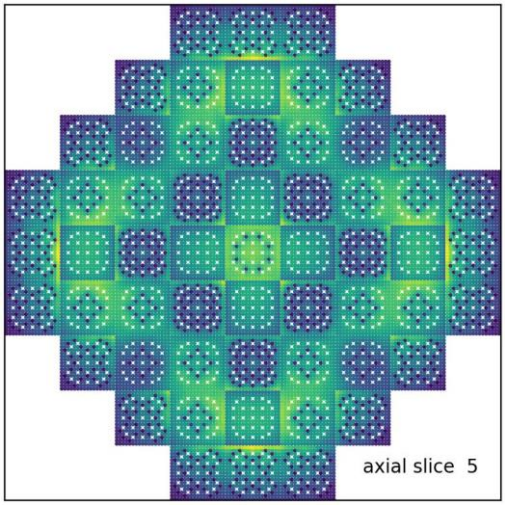

Figure 54. (Case 1.1, ENDF/B-VII.1) Serpent/SCF fuel temperature in axial slice 5, corresponding to the peak-power region.

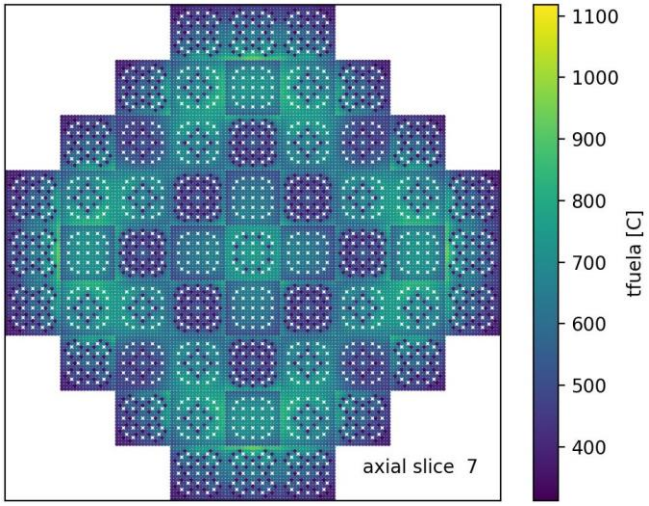

Figure 55. (Case 2.1, ENDF/B-VII.1) Serpent/SCF fuel temperature distribution in axial slice 7, corresponding to the peak-power region.

Co-funded by the European Union
UK Research and Innovation
The Research Council of Norway
Project funded by

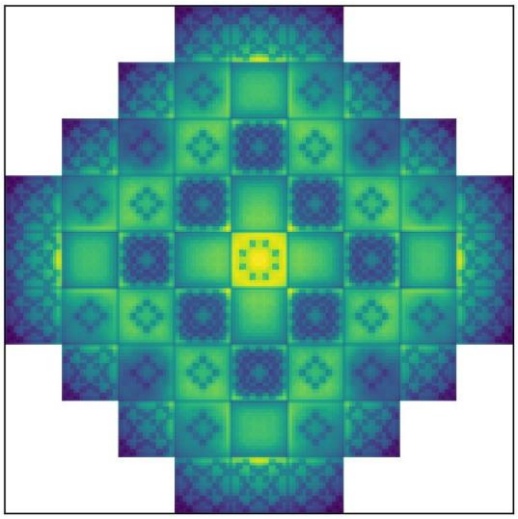

Figure 56. (Case 1.1, ENDF/B-VII.1) Serpent/SCF coolant temperature in axial slice 20.

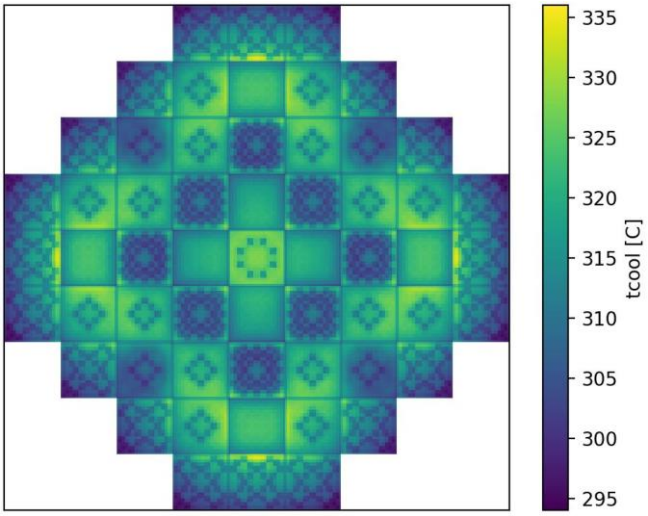

Figure 57. (Case 2.1, ENDF/B-VII.1) Serpent/SCF coolant temperature in axial slice 20.

Co-funded by the European Union
UK Research and Innovation
The Research Council of Norway
Project funded by


EASI SMR